

UNCLASSIFIED

AD NUMBER

AD805309

LIMITATION CHANGES

TO:

Approved for public release; distribution is unlimited.

FROM:

Distribution authorized to U.S. Gov't. agencies and their contractors;  
Administrative/Operational Use; JAN 1967. Other requests shall be referred to Air Force Rocket Propulsion Laboratory, Wright-Patterson AFB, OH 45433.

AUTHORITY

AFAPL ltr dtd 12 Apr 1972

THIS PAGE IS UNCLASSIFIED

AFAPL-TR-65-48  
PART II

805309

**HIGH SPECIFIC IMPULSE THERMAL  
ARC JET THRUSTOR TECHNOLOGY**

**Part II. Performance of Hall Arc Jets With Lithium Propellant**

**G. L. Cann et al.**

**Electro-Optical Systems, Inc.**

**TECHNICAL REPORT AFAPL-TR-65-48, PART II**

**January 1967**

**Air Force Aero Propulsion Laboratory  
Research and Technology Division  
Air Force Systems Command  
Wright-Patterson Air Force Base, Ohio**

25  
AFAPL-TR-65-48  
Part II

HIGH SPECIFIC IMPULSE THERMAL  
ARC JET THRUSTOR TECHNOLOGY

Part II. Performance of Hall Arc Jets With Lithium Propellant

G. L. Cann, et al  
Electro-Optical Systems, Inc.

TECHNICAL REPORT AFAPL-TR-65-48, PART II

January 1967

Air Force Aero Propulsion Laboratory  
Research and Technology Division  
Air Force Systems Command  
Wright-Patterson Air Force Base, Ohio

## FOREWORD

This report was prepared by Electro-Optical Systems, Inc., Pasadena, California, to summarize the results of the second phase of Contract AF 33(615)-1579, Project No. 314101. This contract began in April 1964. The first phase ended in March 1965 and the second phase ended in March 1966. The contractor's number for this report is EOS 5090-Phase II Final. The report authors are G. L. Cann, R. A. Moore, R. L. Harder, and P. F. Jacobs.

This research contract is funded by the Aero Propulsion Laboratory of the Air Force Research and Technology Division. The program is monitored in the Electric Propulsion Technology Section of the Aero Propulsion Laboratory by Mr. Paul Lindquist.

The authors gratefully acknowledge the contributions of C. H. Giltner, C. B. Shephard, Jr., S. M. Snider, E. G. Doty, B. A. Sanders, T. L. Jacobson, and W. Prichard in obtaining the results reported.

Publication of this report does not constitute Air Force approval of the report's findings or conclusions. It is published only for the exchange and stimulation of ideas.

DAVID F. O'BRIEN, 1/Lt., USAF  
Aerospace Engineer, Electric Propulsion  
Propulsion and Power Branch  
Aerospace Power Division

This technical document report has been reviewed and is approved.



## ABSTRACT

The objective of this program is to develop the technology of efficient electric arc jet thrusters for high specific impulse and long life. It is aimed particularly at power levels between 10 and 50 kW, specific impulse between 1500 and 6500 seconds, and power input-to-thrust ratios less than 190 kW/lb for durations up to 100 hours. The approach combines analytical and experimental research to investigate and develop thrusters using lithium and other alkali metals as propellants. Alkali metals have the advantage of high frozen-flow efficiency compared with gaseous propellants used in previous arc jet work. The use of lithium in this  $I_{sp}$  range requires energies per particle which are not achievable by the electrothermal arc-heating process. Thus, it is necessary to employ, in addition, electromagnetic acceleration processes. The present approach has relied predominantly on Hall current interactions with an applied magnetic field. Thrusters of this type have been designated ALPHA (Alkali Plasma Hall Accelerator). During the second phase of the program the following advances have been made. The effects of the testing environment upon the measured performance have been intensively investigated and criteria developed for determining when the measurements can be relied upon. The performance of potassium propellant has been investigated and found to be comparable with that of lithium at low specific impulse and worse at higher specific impulses. This is tentatively explained by multiple ionization of the potassium. Two major modifications to the design of the engine have been made: (a) the cylindrical cathode has been replaced by a buffered cathode with separate propellant injection, thereby increasing the thrust per unit current, decreasing the cathode power loss per unit current, increasing the insulator lifetime and helping to separate the ionization and acceleration processes; and (b) the region of strong magnetic field has been extended downstream by placing a second coil on the engine, thereby reducing the magnet power requirement by a factor of almost five. The vacuum tank has been doubled in length and the background pressure during a typical run has been reduced by almost an order of magnitude. The thrust balance has been improved, permitting measurements with an accuracy of about  $\pm 2$  percent. A new high capacity feed system has been designed to provide continuous reliable operation for periods of over 100 hours at levels around 10 mg/sec. A theory has been developed for the operation of ALPHA. Calculations based on this theory indicate that significant improvements can be made over present performance. Equally important, the theory gives design parameters that can be tested and then used in the development of optimum thrusters.

## CONTENTS

I	INTRODUCTION	1
II	SUMMARY	9
III	THEORY AND MECHANISMS	11
	1. Introduction	11
	2. Acceleration Mechanisms	12
	3. Electrode Mechanisms	21
IV	FACILITY MODIFICATIONS	27
	1. Improvements of Measurement Techniques	27
	2. Thrust Balance Improvements	40
V	HIGH VACUUM TESTS	41
	1. High-Vacuum Tests of a Lithium Thrustor	41
VI	POTASSIUM PERFORMANCE MEASUREMENTS	47
VII	CONFIGURATION STUDIES	61
	1. Buffered Cathode Thrustor Studies	61
VIII	ENDURANCE TESTS	103
	APPENDIX I - TEST DATA	105
	APPENDIX II - X-ATRON ANALYSIS	129
	APPENDIX III - CATHODE HEAT TRANSFER CALCULATIONS	143
	REFERENCES	153

## ILLUSTRATIONS

1	Typical Contour Lines of Constant Pseudo-Potential For a Magnetic Coil	20
2	Comparison of Ring and Tip Cathode Attachments	24
3	Feed System Bellows - Volume Displacement versus Linear Displacement	28
4	Feed System Bellows - Volume Change Due to Pressure Difference	29
5	Feed System Bellows Spring Force Calibration	30
6	MK-1B Lithium Feed System and Vaporizer	32
7	10 kW Lithium Arc Jet Model LAJ-AF-CG-1	34
8	Lithium Feed System	35
9	Lithium Feed System - Model LV 4-1	37
10	Modified Balance With Coaxial Mercury Parts and Water U-Tubes	40
11	Arc Jet Model LAJ-AF-6D	42
12	Lithium Arc Jet and Balance Assembly	43
13	Lithium Arc Jet 6-Ft-Diameter Test Chamber	44
14	Arc Jet Model LAJ-AF-6D	48
15	Hall Arc Jet Performance With Potassium	50
16	Thrust versus Tank Pressure With Potassium	51
17	Effect of Magnetic Field Strength on Thrust and Voltage for Potassium	53
18	Effect of Magnetic Field on Arc Potentials for Sodium and Potassium	54
19	Effect of Magnetic Field Strength on Anode Power Loss for Sodium and Potassium	55
20	Cathode Power Loss as a Function of Arc Current	57
21	Thrust versus Current with Potassium	58
22	Thrust per Unit Current, Voltage as a Function of Parameter $\psi = \frac{e}{m_a} \frac{m}{I}$ , for Potassium	59

# ILLUSTRATIONS (contd)

23	Buffered-Cathode Thrustor Configuration, Model LAJ-BF-1	62
24	Lithium Arc Jet Assembly, Models LAJ-BF-1B, -1C, -1D and -1E	64
25	10 kW Lithium Arc Jet, Model LAJ-AF-BG-1 and 1A	65
26	10 kW Lithium Arc Jet, Model LAJ-AF-CG-1	66
27	Overall Efficiency $\left(\frac{T^2}{2mVI}\right)$ of Lithium Arc Jet Model LAJ-AF-BG-1A as a Function of Specific Impulse	76
28	Thermal Efficiency of Lithium Arc Jet Model LAJ-AF-BG-1A as a Function of Specific Impulse	77
29	Ratio of Thrust to Arc Current for Lithium Arc Jet Model LAJ-AF-BG-1A as a Function of the Mass-Flow, Current Parameter $\psi$	78
30	Ratio of Thrust Arc Current for Lithium Arc Jet Model LAJ-AF-BG-1A as a Function of the Magnet-Coil Current	80
31	Lithium Arc Jet Assembly	81
32	Thrust Efficiency versus Specific Impulse	83
33	Axial Magnetic Field at Coil Centerline for Thrustor Models AF-CG-1A and 1B	85
34	Thermal Efficiency versus Specific Impulse, Models AF-CG-1A and 1B	86
35	Cathode Power Loss versus Arc Current	88
36	Thrust Per Unit Arc Current versus the Parameter $\psi$ for Models AF-CG-1A and 1B	89
37	Effect of Magnetic-Coil Current on Thrust to Arc Current Ratio, Model AF-CG-1B	90
38	Thrust to Arc Current Ratio versus Tank Pressure for Models AF-CG-1A and 1B	91
39	Power to Thrust Ratio for Model LAJ-AF-CG-1 versus Magnet Coil Current	94
40	Thermal Efficiency of Model LAJ-AF-CG-1 versus Magnet Coil Current	96
41	Thrust Efficiency versus Specific Impulse for Model LAJ-AF-CG-1C	97
42	Thrust Efficiency versus Specific Impulse for Model LAJ-AF-CG-1C	98
43	Thrust Efficiency versus Specific Impulse for Model LAJ-AF-CG-1D	99
44	Photograph of Extended Propulsion Test Chamber	101

# LIST OF SYMBOLS

$A$	=	Vector potential
$\bar{B}$	=	Magnetic induction
$\bar{E}$	=	Electric field intensity
$e$	=	Electronic charge
$F^*$	=	$F_a - F_s$ = (bellows actuator force) - (bellows spring force)
$H$	=	Pseudo-potential defined on p. 17
$h$	=	Height
$I$	=	Current
$I_A$	=	Arc current
$I_C$	=	Magnet coil current
$I_{sp}$	=	Specific impulse
$J$	=	Current density
$k$	=	Boltzmann's constant
$L$	=	Length
$M$	=	Mach number
$m$	=	Particle mass
$m$	=	Mass of propellant in bellows
$\dot{m}$	=	Mass flow rate
$m_a$	=	Atomic mass
$m_{aa}$	=	Atomic mass in anode jet
$m_{ac}$	=	Atomic mass in cathode jet
$n_e$	=	Electron particle density
$P_A$	=	Arc power
$P_{an}$	=	Power in anode
$P_{ca}$	=	Power in cathode
$P_{C+B}$	=	Power in anode and buffer
$P_{mag}$	=	Magnet power
$P_r$	=	Power radiated and conducted
$P_t$	=	Pressure in vacuum chamber (torr)
$P_\theta$	=	Canonical angular momentum

# LIST OF SYMBOLS (contd)

$p$	=	Plasma pressure
$R$	=	Radius of cathode jet
$R_A$	=	Anode radius
$R_{A0}$	=	Radius of anode sheath at the anode
$R_C$	=	Radius of cathode attachment zone
$R_{cr}$	=	Minimum radial coordinate of ion trajectory
$r$	=	Radial coordinate
$\dot{r}$	=	Radial velocity
$\ddot{r}$	=	Radial acceleration
$s$	=	Variable of integration
$T$	=	Plasma temperature
$T$	=	Temperature of liquid in bellows
$t$	=	Time
$u$	=	Radial velocity
$V$	=	$V(x, F^*)$ = volume of bellows
$V_A$	=	Potential drop along anode sheath
$V_I$	=	Ionization potential
$v$	=	Azimuthal velocity
$v_{cr}$	=	Critical velocity
$w$	=	Axial velocity
$\bar{w}$	=	Average axial velocity of the gas near the anode
$x$	=	$L_{max} - L$ = displacement of bellows
$\dot{z}$	=	Axial velocity
$\ddot{z}$	=	Axial acceleration
$\gamma$	=	Specific heat ratio
$\eta_b$	=	Overall efficiency
$\dot{\theta}$	=	Azimuthal velocity
$\ddot{\theta}$	=	Azimuthal acceleration
$\rho$	=	Density of liquid in bellows
$\rho$	=	Plasma density

# LIST OF SYMBOLS (contd)

- $\sigma$  = Plasma conductivity  
 $\phi$  = Electrostatic potential  
 $\phi_A$  = Anode potential  
 $\psi = \frac{e \hbar}{m_a I}$   
 $\psi_c = \frac{e \hbar_c}{m_{ac} I}$   
 $\omega$  = Angular velocity

## Subscripts

- $z$  - Axial  
 $r$  - Radial  
 $\theta$  - Azimuthal



## SECTION I

### INTRODUCTION

This report summarizes the results obtained during the second year of a 3-year program aimed at developing the technology of steady-state arc devices to the point where it will be possible to build plasma thrusters capable of the following performance:

Power Input	Up to 300 kW
Specific Impulse	1500-4000 sec
Overall Efficiency	Greater than 60 percent
Lifetime	Over 500 hours

The technology of the alkali metal plasma thruster was developed during the first phase of this program. However, a number of outstanding problems still existed at the end of the first phase which were of a rather fundamental nature. The most important are listed below.

1. Possible effects of the test environment upon the measured engine performance cast some doubt upon the data obtained from thrust and mass flow rate measurements.
2. Of the alkali metals, only lithium had been investigated. Its performance at low specific impulse appeared rather poor and calculations indicated that sodium or potassium might perform better.
3. The engine mechanisms were not well enough understood to be useful in developing optimum engine designs. One result of this was that the magnet power was twice as high as the arc power, making the overall efficiency quite low.

One of the most difficult questions that confronts the experimentalist who is attempting to evaluate the performance capability of an alkali metal accelerator is to define the conditions which will constitute a valid test. The problem arises because the discharge extends an indeterminate distance into the wake. The specific questions are these:



1. How large must the vacuum tank be to insure that the tank walls do not affect engine performance?
2. What precautions must be taken to insure that the mass flow rate in the exhaust beam is equal to or lower than the propellant injection rate into the accelerator?

Preliminary tests indicated that the size of the tank is not critical. However, the possibility still exists that in some cases the tank may limit the size of the discharge, or may actually carry some of the discharge current over a part of its path. Tests in tanks of various diameters and lengths have been conducted at EOS and elsewhere but the results are still not conclusive because other variables occurred simultaneously in the tests.

The problem of determining the ratio of beam particle flux rate to propellant injection rate is formidable. When tests are being conducted with an alkali metal propellant any one of the following sources of extra material for the beam exists:

1. Propellant can condense on any cool engine component. When conditions are altered so that the engine heats up, this propellant can vaporize and enter the exhaust beam.
2. If all of the beam particles do not adhere to the target or tank walls once they have struck it, then this "backstreaming" propellant can be ionized and accelerated in the discharge, resulting in a recirculation of the propellant.
3. If any background gaseous material is present in the vacuum tank (e.g., air leakage), then this substance can be ionized and accelerated by the discharge.
4. The heat flux to one or both electrodes can become high enough to vaporize electrode or insulator material. The discharge may then ionize and accelerate this material.

Items 1 and 4 can be controlled by proper design and by exercising care while testing. By using adequate pumping capacity and careful sealing of the vacuum tank, the impurity level of ambient gas can be maintained

adequately low. If necessary, liquid nitrogen liners can be used. There is real difficulty, however, in determining if the recirculation of propellant can ever be completely eliminated. The beam itself is likely to dislodge particles that have condensed in the target area and these could backstream into the volume of the discharge.

The extent to which any one or several of the above-mentioned four processes may have had some influence upon performance data that have been reported elsewhere and in this report are difficult to assess. Efforts have been made at EOS to control all four of the above-mentioned items. These are reported here and in Refs. 1 and 2.

A few very general statements concerning these mechanisms which govern the behavior of magnetic annular accelerators can be made:

1. Thrust is produced by the expulsion of high-velocity ions from the engine.
2. The ions are produced by collisions between atoms and energetic electrons throughout the volume of the discharge.
3. The electrical discharge extends a considerable distance downstream of the electrodes and, hence, transfers most of the energy and momentum to the gas far from the engine. Viscous interaction with engine components can hence be neglected. Thermal conduction effects to all engine components other than the cathode can also be neglected.
4. Since the discharge occurs in a low density environment, most of the internal energy of the gas can be associated with the electrons. As the arc current becomes large, e.g., > 1000 amps, then this may not remain valid, since the high pressures in the cathode jet could lead to considerable ion heating due to electron-ion collisions. Similarly, the energy associated with the body forces exerted on the gas can be associated with the ions.
5. The power transferred to the anode can be attributed almost entirely to the energy convected by the electrons as they

carry the current into the anode. This is especially true when the cathode tip is flush with the anode face. As the cathode tip is recessed further and further back in the anode cavity, more and more of the anode heating will be due to conduction from the hot gas.

6. The solenoidal magnetic field that is applied acts as a magnetic nozzle for any plasma that is produced by the discharge. That is, all forms of electron and ion energy (exclusive of ionization and radiation) are converted into axial and radial ion velocities by expansion out of the magnetic field. This indicates that all the electrical power of the discharge can be converted into beam power except for: (a) the anode and cathode power loss, (b) the power used in ionizing the propellant.
7. All of the beam power cannot be converted into axial kinetic energy. The ions will have some tangential velocity to balance the torque produced on the accelerator by the discharge current crossing the applied magnetic field. There will also be some radial velocity of the ions due to the shape of the magnetic nozzle.
8. A large fraction of the thrust reaction occurs on the magnet. This indicates that azimuthal currents must be flowing in the plasma tube.

The above considerations lead to some well-defined design criteria:

1. Raise the arc voltage to as high a value as possible while maintaining the electron temperature at modestly low values. This will transfer a large amount of kinetic energy directly to the ions with good thermal efficiency.
2. Inject the propellant so that it will be ionized in a region of high potential, i.e., near anode potential. This will allow the ions to carry some of the current and thus acquire energy directly from the electric field.

3. Use a propellant of low molecular weight to obtain the best possible energy transfer characteristics between ions and electrons. Also pick a propellant with a low first ionization potential so the gas can be easily singly ionized with a minimum power loss. The second ionization potential should be as high as possible to prevent energy losses in excitation or ionization of the second electron.

The development of a comprehensive theory describing the mechanisms and performance capability of the accelerator has also proven to be a very difficult task. A phenomenological theory was developed at EOS during the first phase of this program which used measured dependencies of thrust and anode power loss upon the controllable variables to develop relations among the voltage, specific impulse, and thrust efficiency. Naturally, this approach did not identify any mechanisms for thrust production or power losses. A more fundamental approach to the problem is presented in Appendix II of this report and a complete analysis is carried out for a simplified model of the accelerator. The significance of some overall conservation principles is also discussed.

The underlying principle of the analytic approach developed at EOS is that the discharge will operate in a minimum potential mode. This follows the accepted approach to studying arc discharge phenomena, which is assumed to remain valid even when a significant fraction of the discharge power is transferred directly into kinetic energy of the ions. This leads to the concept of a critical mass flow defined as the effective mass flow rate. The ideas behind this concept are simple. Assume that a discharge is occurring in a vacuum environment across an electrode configuration where the arc current and applied magnetic field strength are held constant while the propellant flow rate through the engine is varied. If the thrust is electromagnetic in origin, it will not increase appreciably as the flow rate increases. If the propellant is fully ionized in the discharge, then as the flow

rate is increased the beam power decreases and the power used to ionize the propellant increases. These two competing processes indicate that there will probably be some mass flow rate at which the power input, or voltage drop will be a minimum. It is then assumed that the discharge will encompass enough volume to ionize propellant at just this critical rate, provided enough is available. If more than the "effective" mass flow rate is injected through the engine, it is assumed that the excess is not ionized and, hence, diffuses out of the accelerator unused. If less than the "effective" mass flow rate is injected through the electrodes, the discharge will attempt to entrain ambient material to make up the deficit.

Using the above concepts, calculations of engine performance when the thrust depends linearly upon the magnetic field strength have been made by Bennett and John at AVCO-RAD (Ref. 3).

Early in the development of the present Hall current accelerator, it was realized that the device magnetically confined the plasma flow in the radial direction. It also appeared that energies in the order of 100 electron volts were transferred to the heavy particles from the electromagnetic field. These properties of the device appeared interesting enough to initiate a program at EOS to investigate the potential of using the processes occurring in it to heat and confine a plasma to temperatures and pressures where it could be of value to thermonuclear research. This program was funded by EOS and Xerox. One aspect of the investigations conducted appeared very relevant to the accelerator operation and the results are reported here in Appendix II.

As mentioned earlier, one of the main criteria for design improvement is to increase the potential drop of the discharge while keeping the energy of the electrons entering the anode low. The results of Appendix II indicate scaling laws for accomplishing this which involve major changes in the configuration. The ideal accelerator would appear to be something very close to a space charge-neutralized ion engine and propulsion devices designed to work on this principle have been called



ALPHA (ALKali Plasma Hall Accelerator) at EOS. First, it is necessary to separate the ionization process from the acceleration process so that the ion spin can be increased to a value higher than

$$V_{cr} = \sqrt{\frac{2 |e| V_I}{m_a}}$$

This is accomplished by:

1. Introducing a new ionizer electrode downstream of the anode.
2. Shaping the magnetic field so that the electron current between the cathode and anode is reduced to a minimum.

Second, two separate flows are set up, a cathode jet and an anode sheath. The former comprises high density plasma formed by injecting gas over the buffered cathode. The total arc current is carried by electrons in the cathode jet. This plasma slowly expands across the magnetic field lines and as it does so, the following things happen:

1. The plasma spins up.
2. The arc current forms into an annulus surrounding the plasma column.
3. The plasma heats up.
4. As the diameter of the column increases, the potential drop along the column increases.

The anode sheath is composed of ions formed by electron collisions with the gas injected through the anode. These ions, together with the electrons which space charge neutralize them form a collisionless plasma which drifts downstream and spins. The ions have a radius of closest approach to the axis which depends upon the potential drop between the anode and the magnetic field line at that radius. Third, it is postulated that, if a long enough region of uniform magnetic field is supplied, the cathode jet and anode sheath will meet to complete the current path in such a manner that the total potential drop is a minimum. This postulate defines an interaction length for the device which then becomes one of the basic design variables. The

above approach represents a very definite break with conventional MPD arc technology. In particular, the approach of AVCO-Everett and AVCO-RAD appears to be that of promoting electron conduction only and thus having almost all of the discharge current cross between anode and cathode very close to the electrodes (Refs. 4 and 5), thus justifying the name MPD arc. The evolution of the ALPHA concept from earlier work at EOS on MPD arc technology now raises the possibility of a dual approach to the design of steady-state plasma thrusters, reminding one of the state of affairs in ion engine development, where contact ion engines compete with bombardment ion engines.

## SECTION II

### SUMMARY

During this phase of the program a number of significant advances have been made in the technology of steady-state plasma thrusters. The effects of the testing environment upon the measured performance have been intensively investigated and criteria developed for determining when the measurements can be relied upon. The performance of potassium propellant has been investigated and found to be comparable to that of lithium at low specific impulse and worse at higher specific impulses. This is tentatively explained by multiple ionization of the potassium.

Two major modifications to the design of the engine have been made. First, the cylindrical cathode has been replaced by a buffered cathode with separate propellant injection. A fairly extensive experimental program was required to effect this change. The advantages gained are as follows:

1. A small cross-section for cathode attachment is maintained, thus producing more thrust per unit current, and also less power loss per unit current to the cathode.
2. The discharge is moved away from the insulator between the cathode and anode, thus greatly increasing the lifetime of the insulator.
3. The cathode jet is made an independent entity, thus helping to separate the ionization and acceleration processes.

Second, the region of strong magnetic field has been extended downstream by placing a second coil on the engine. This has accomplished the following results:

1. The magnet power required to obtain good engine performance has been reduced by a factor of almost five. It is now possible to operate a 20 kW arc with under 5 kW in the magnet.



2. The results of adding the magnet indicate that the concept of separating the acceleration and ionization processes by increasing the interaction distance may be valid and that significant advances can be made by pursuing this approach. With the present configuration, it has been possible to obtain an overall efficiency (including magnet power) of about 45 percent at an  $I_{sp}$  of 6000 sec.

The lithium test facility has undergone major changes during this phase. The vacuum tank has been increased in length by a factor of two. Simultaneously, more diffusion pumps have been added to the tanks so that the background pressure has been reduced by almost an order of magnitude during a typical test. The thrust balance has been modified to reduce tare and interaction forces. This allows us to measure the thrust with an accuracy of about  $\pm 2$  percent.

A design for a new high capacity feed system has been developed. Preliminary tests indicate that this feed system will work reliably for periods of over 100 hours and give accurate, continuous, flow rate measurements, at levels around 10 mg/sec.

A theory has been developed for one specific mode of operation of the accelerator, characterized by the use of an alkali metal as propellant, by energy transfer mechanisms involving Hall current interactions, and by ion conduction rather than electron conduction across magnetic field lines. In order to differentiate a thruster operating in this mode from other types of MPD arc jets and to underscore the evolutionary advances which it embodies, this thruster has been termed ALPHA (ALKali Plasma Hall Accelerator). Calculations, based upon the theory, indicate that significant improvements can be made over present engine performance. Equally important, the theory gives design parameters that can be tested and then used in the development of optimum thrusters.

## SECTION III

### THEORY AND MECHANISMS

#### 1. INTRODUCTION

Analysis has been completed for several isolated features of the Hall current accelerator. The Hall current accelerator, or MPD arc, has two concentric electrodes in a magnetic field coil, a propellant feed, and sometimes a nozzle. In spite of this simple construction, the physical processes which occur are very complex. So far no complete analysis of all mechanisms exists.

Thrust comes from at least three mechanisms which can be identified. The proportion of thrust of the several types will vary with the experimental conditions. Thrust can arise due to:

1. Heating and expansion through a nozzle.
2. Interaction of the currents with the applied magnetic field.
3. Interaction of the currents with the induced magnetic field.

In addition to the real complexity due to the distinct processes causing thrust, there can be more than one way to describe the same thrust. As an example, electrostatic acceleration of ions through trapped electrons can be the same as interaction of induced azimuthal currents with the applied magnetic field. In this report, attention has been focused upon a mode of operation in which most of the thrust is due to an interaction of induced azimuthal currents with the applied magnetic field.

The electrodes are important since they are a major area of power loss, the primary factor for determining lifetime, and a factor in the ionization efficiency. Electrode behavior is complicated by the fact that attachment may be nearly a point or diffuse. The complete solution for electrodes is not available, but results show that point attachment to the cathode will result in less power loss.

## 2. ACCELERATION MECHANISMS

The ability of axisymmetric Hall current plasma accelerators to produce significant amounts of thrust has definitely been established. However, the mechanisms by which the propellant is accelerated are still not completely understood, making it difficult to design optimum engines. Some general considerations of this problem are discussed below and one mechanism is identified as that most likely responsible for the axial acceleration of the gas, which results in the production of thrust.

A few general rules that are of value in guiding the discussion are listed below:

1. Thrust is produced only by the expulsion of high-velocity particles from the thruster. In electromagnetic devices these particles must be predominantly ions. These ions will be accompanied by an equal number of electrons moving at the same exhaust velocity. Because of their low mass, the electrons do not make any significant contribution to the momentum of the exhaust beam.
2. The ions can attain high axial velocities through the following mechanisms:
  - a. Conversion of ion enthalpy into kinetic energy by expansion through a mechanical or a magnetic nozzle.
  - b. The conversion of ion azimuthal energy into axial kinetic energy by expanding the rotating plasma through a magnetic nozzle.
  - c. Acceleration of the ions through an applied axial potential when either radial or azimuthal magnetic fields are present.
  - d. Acceleration of the ions through an axial potential drop which is supported by an electron pressure gradient. Except for elastic collisions, this is the only mechanism through which electron energy can be transferred to the ions and is, by far, the most effective at low number densities.

3. When an electric discharge occurs such that the current flows along axial magnetic field lines, no momentum in the axial direction is transferred between the plasma and the electromagnetic field. The energy dissipated in such a discharge is all transferred originally into the internal energy of the electrons.
4. In the discharge region ions are produced by inelastic collisions of atoms and electrons. The electrons gain the energy necessary to ionize the gas by carrying some fraction of the discharge current.

In discussing the thrust-producing mechanisms, it is convenient to divide the discharge into two regions, the cathode jet and the anode sheath. The cathode jet and anode sheath are those regions of the discharge emanating from the electrodes and following the direction of the magnetic field. These distinct current-carrying regions are visible and their existence has been verified by measurement of the axial current distribution across and along the discharge.

a. The Anode Sheath

The acceleration mechanisms in the anode jet can most conveniently be investigated by assuming that all of the mass in the anode jet leaves the anode through a thin annulus in the anode front face at a radius of  $R_{A_0}$ . We shall also assume that the gas is fully ionized as it leaves the anode. The analysis of the anode sheath indicates that it cannot grow faster than the magnetic field. Since the magnetic field diverges slowly near the anode, little loss of accuracy occurs if we assume the discharge occurs in a uniform magnetic field followed by a diverging field or "magnetic nozzle".

Because of the low density of the gas in the anode sheath a negligible amount of the energy transferred out of the electric discharge is in the internal energy of the ions as they enter the cathode jet. This, then, indicates that for the gas in the anode sheath, the

energy is originally almost all transferred into the rotational energy of the gas in the discharge region. As the gas then expands through the magnetic nozzle and conserves angular momentum, a large fraction of this energy can be converted into axial kinetic energy. If this is indeed the mechanism by which most of the thrust is produced by the engine, then some of the consequences would be:

1. When some of the current in the anode sheath is carried by electrons the ions will be spun up to velocities such that

$$\frac{1}{2} m_a v^2 > |e| V_A$$

where  $V_A$  is the potential drop which occurs along the anode sheath. This gives a logical and believable mechanism by which the gas exhaust energy per particle can be greater than would be obtained by falling through the arc potential drop.

2. The propellant should be injected through the anode.
3. The propellant should be ionized as near the anode as is possible, preferably inside of the anode.

At this point in the discussion it is of value to ask what role the Hall currents play in the acceleration mechanism postulated above. First, the azimuthal electron drift which comprises the Hall currents occurs because of the poor mobility of the electrons across the axial magnetic field. In order to draw a radial current the radial electric field is thus strengthened to the point where any ions that are produced in the anode sheath are accelerated through the radial potential drop and thus can conduct an appreciable fraction of the current. This ion energy, which is gained directly from the radial electric field, appears as rotational energy of the ions due to the turning effect of the axial magnetic field. The first effect of the Hall currents is thus to produce a radial electric field and to make

possible ion conduction so that momentum and energy can be transferred directly from the electromagnetic field into the azimuthal motion of the ions. Because of the centrifugal force on the ions they will never spin up to an azimuthal velocity as high as that of the electrons, which is probably quite close to the local value of  $|E_r/B_z|$ . This insures that Hall currents will always flow, even when particle mean free paths are very large compared to the diameter of the jet. A second effect of the Hall currents upon the acceleration mechanisms occurs precisely because the electrons are spinning faster than the ions, i.e., azimuthal momentum is transferred from the electrons to the ions through collisions. This insures that the ion energy is greater than what it gains by dropping through the radial potential drop.

The fact that the Hall currents are responsible for putting the energy and momentum initially into ion rotation rather than into axial velocity should not deter us from considering the device as primarily a Hall current accelerator. Also, most of the observations and measurements made so far upon MPD arc devices can be explained through Hall currents producing the accelerations discussed above. For this reason, it is believed that an analytic investigation based upon the action of the Hall currents is likely to be much more useful than attempts to develop other explanations for the performance capabilities of MPD arc devices.

An analysis of the anode sheath of sufficient density for many collisions to occur has been completed and reported in Ref. 6. A mode of operation with no collisions (other than for ionization) is theoretically possible. Ions formed near the anode are electrostatically accelerated through the magnetic field to the exit region. Electrons are emitted at the cathode and can leave with the ions without crossing the magnetic field. Sufficient electrons are present throughout the volume to keep the plasma neutral.

For the collisionless case the equations of motions for individual particles can be written, and (except for algebraic difficulties) integrated. This requires knowledge of the magnetic and



electric fields. For low density operation it is valid to assume that the magnetic fields are unperturbed from those supplied by external magnets. The same is not true for electric fields which can be greatly affected by space charges even at low density. Hence the approach is to model the electric fields such that the electric potential matches the applied potential at the electrodes.

If the applied potential is great enough, it is possible for an ion to escape the field without any collisions. It is possible to mathematically eliminate the azimuthal motion from the equations, and to introduce a pseudo-potential for the r-z motion that involves the centrifugal and magnetic effects. For the r-z motion the ion acts as if it were under the influence of the applied potential plus the pseudo-potential. The pseudo-potential is a barrier which must be crossed for the particle to escape. A necessary condition for an ion to escape is that the applied potential drop is greater than the pseudo-potential rise for all points along the trajectory. This can always be done by making the applied potential sufficiently large.

When the particle density is sufficiently low that short range encounters may be neglected, charged particles interact only through the average induced fields, and the motion of each particle can be found from Newton's law. When there is axial symmetry, the azimuthal equation of motion can be integrated, and the radial and axial equations simplified. This is useful either as an aid for finding the exact solution or for increasing our understanding or intuition.

The derivation is not original (see, for example, Ref. 7). A brief outline follows. For the motion of a charged particle in steady axisymmetric field the equations of motion are:

$$m(\ddot{r} - r\dot{\theta}^2) = e(E_r + r\dot{\theta}B_z - \dot{z}B_\theta) \quad (1)$$

$$m(r\ddot{\theta} + 2\dot{r}\dot{\theta}) = e(\dot{z}B_r - \dot{r}B_z) \quad (2)$$

$$m\ddot{z} = e(E_z + \dot{r}B_\theta - r\dot{\theta}B_r) \quad (3)$$

The equations have been written in cylindrical coordinates. Because of the assumption for the fields of axial symmetry ( $\partial/\partial\theta = 0$ ) and steady ( $\partial/\partial t = 0$ ), it follows that  $E_r = -\partial\phi/\partial r$ ,  $E_\theta = 0$ ,  $E_z = -\partial\phi/\partial z$ ,  $B_r = -\partial A_\theta/\partial z$  and  $B_z = \partial(rA_\theta)/\partial r$ . The scalar potential  $\phi(r, z)$  and the azimuthal component of the vector potential  $A_\theta(r, z)$  give all radial and axial electromagnetic fields. Equation 2 can be integrated to give the angular momentum integral

$$mr^2\dot{\theta} + erA_\theta = P_\theta \quad (4)$$

where the canonical angular momentum  $P_\theta$  is a constant along any trajectory. Equation 4 can be solved for  $\dot{\theta}$ , and  $\dot{\theta}$  can be eliminated from Eqs. 1 and 3 to give (after some calculus)

$$m\dot{r} = -e \frac{\partial\phi}{\partial r} - \frac{\partial H}{\partial r} - e\dot{z} B_\theta \quad (5)$$

and

$$m\dot{z} = -e \frac{\partial\phi}{\partial z} - \frac{\partial H}{\partial z} + e\dot{r} B_\theta \quad (6)$$

where

$$H = (P_\theta - erA_\theta)^2/2mr^2 = \frac{m}{2} (r\dot{\theta})^2 \quad (7)$$

In Eqs. 5 and 6,  $H(r, z)$  plays the role of a potential, and hence will be called a pseudo-potential (or effective potential). Equations 5 and 6 allow solution for the  $r$  and  $z$  motion without specifically considering  $\theta$  motion.

The azimuthal motion effects upon the  $r$ - $z$  motion are provided by the pseudo-potential  $H$ . These include the centrifugal and the Lorentz forces due to azimuthal velocity. The Lorentz forces  $\dot{z}B_\theta$  and  $\dot{r}B_\theta$  in Eqs. 5 and 6 do not come as gradients of the pseudo-potential. One other feature of  $H$  is that it depends not only upon the spatial location, but also upon the initial condition for the particle. Thus two particles which pass through the same point may



not have the same pseudo-potential. The advantage of introducing the pseudo-potential is that it allows solution of a 3 dimensional motion (Eqs. 1 to 3) as a two dimensional problem (Eqs. 5 to 6).

The energy integral of Eqs. 5 and 6 is

$$\frac{m}{2} (\dot{r}^2 + \dot{z}^2) + e\phi + H = E_0, \quad (8)$$

where  $E_0$  is a constant. Further integrals require knowledge of the detailed form for  $\phi$ ,  $H$  and  $B_\theta$ .

The analogy of a ball rolling on a hilly surface in a gravity field is helpful for visualizing the motion. Since the picture is a bit more difficult when the  $B_\theta$  term is included, we shall neglect  $B_\theta$  in what follows. (It could have been included by having a charged ball roll on a surface which has a vertical magnetic field.) Equations 5 and 6 are analogous to the equations

$$\ddot{r} = -mg \frac{\partial h}{\partial r} \quad (9)$$

$$\ddot{z} = -mg \frac{\partial h}{\partial z} \quad (10)$$

for a rolling ball, where  $h$  is the altitude and  $\partial h/\partial r$  and  $\partial h/\partial z$  should be small compared to one. In the analogy we should not consider the effects of angular inertia of the ball, increased path length due to slope, etc. The vertical velocity of the rolling ball has no relationship to the azimuthal velocity of the charged particle. Finally since the shape of the hill depends upon the initial position, two particles moving through the same volume may see quite different hills in the analogy.

To understand the acceleration in an accelerator, we must examine the pseudo-potential of a charged particle moving in the magnetic field of a magnetic coil. The pseudo-potential depends upon magnetic field, initial angular momentum, charge and mass of a particle

(Eq. 7). A visualization of this potential is helpful to understand the motion of charged particles. In this section the topology will be discussed. A typical example is shown in Figure 1. The first feature, which would occur without any magnetic field or charge, is a zone of potential which approaches infinity as  $1/r^2$  as  $r$  tends to zero. A second feature is that it is always positive or zero. Since the quantity  $P_\theta = e r A_\theta$  will be positive in some areas and negative in other areas, a line where  $H$  equals zero exists. Thus "the valley floors are flat". These lines of zero pseudo-potential follow magnetic field lines since they occur where  $e r A_\theta$  is constant ( $-p_\theta$ ) and  $r A_\theta$  is constant along a magnetic field line. The other contour lines do not follow the field lines. The altitudes involved are inversely proportional to the mass of the particle. There is a ridge line of high potential surrounding the coil which serves as a barrier to stop particles from escaping.

An ion can escape from a magnetic field either with sufficient velocity, or with sufficient potential change. This follows from the fact that, except for a singularity along the axis, the pseudo-potential goes to zero at large distances. The solenoidal magnetic field due to coils of finite size has an asymptotic form of a dipole, for which the vector potential  $r A_\theta$  goes to zero in all directions at great distance from the coil. Thus at large distance, the only part of the pseudo-potential which remains is the part which produces centrifugal forces. Thus the Lorentz forces (gradients of the pseudo-potential) die off sufficiently rapidly that only a finite amount of energy is necessary to infinity. The barriers in the close field are all of finite height.

The primary difference between electrons and ions for escape is the large mass difference. For equal field strengths and initial locations and velocities, the pseudo-potential gradients for electrons are larger than those for the ions, by the inverse of the mass ratio.

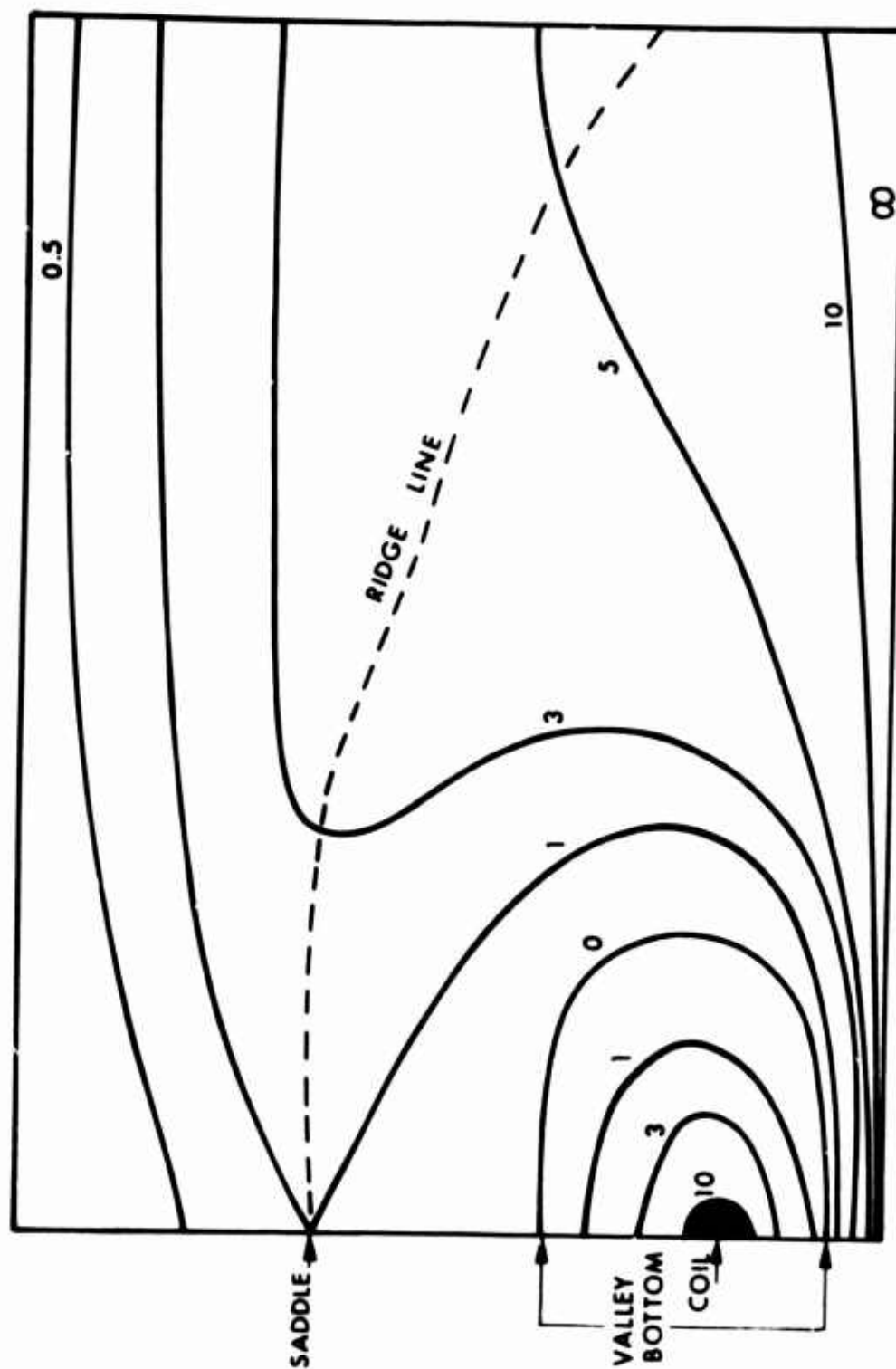


Figure 1 Typical Contour Lines of Constant Pseudo-Potential For a Magnetic Coil

Thus the "hills" which trap the electrons are much "higher". It would take several thousand times as much electrical potential drop to make an electron escape as an ion, except for electrons introduced along the axis which do need to cross fields to get to large distances.

The effect of an occasional collision can be explained by the change the collision produces in the pseudo-potential. The canonical angular momentum  $P_\theta$  which is constant between collisions may be changed by a collision. Thus after any collision the location of the valley will change. This explains how electrons can cross the field, since even though they are trapped in very deep valleys, the valleys are swept across the field as a result of collisions.

This explanation of a collisionless mechanism describes a limiting case of operation which is probably not typical of the actual operation of Hall accelerators.

#### b. The Cathode Jet

Recent investigations indicate that the cathode jet is an important zone where much of the energy addition occurs. Early statements made during the evolution of the theory were to the effect that the cathode jet was primarily a virtual electrode, and the only thrust produced in the cathode jet is that due to the confining force of the self-magnetic field creating a pressure which reacts on the cathode to produce thrust. It is now felt that much energy is added in the form of rotation and internal energy (which will become thrust in the magnetic nozzle) and that pressure is supported by a radial diffusion across the applied magnetic field. A discussion of the mechanisms is given in Appendix II for the case of a high density cathode jet.

### 3. ELECTRODE MECHANISMS

#### a. Cathode Mechanisms

The current can be carried into the cathode by either ion bombardment or electron emission. For the latter process to occur the cathode requires a heat source to "boil off" the electrons. In

practical accelerators both processes are occurring simultaneously. However, in most cathode configurations it is likely that one process will be dominant and hence control the nature of the cathode attachment region. Care should be exercised in cathode design to insure that both mechanisms are not equally likely to occur, since unstable or oscillatory cathode attachment might result.

Although criteria that can be used to identify the cathode mechanism are not well defined, the following shall be used.

1. If the attachment is diffuse, the process is dominated by ion bombardment.
2. If a point attachment occurs, the process is dominated by electron emission.

In our accelerators, which have extended cylindrical cathodes, it is observed that the cathode attachment occurs on the outer cylindrical surface; hence it is dominated by ion bombardment. This ion bombardment energy is partly conducted away and partly used up on electron thermionic emission. Because of the geometry, most of the ion energy is conducted away and a large fraction of the current must be carried by the ions. Calculations indicate that the cathode power loss for this case is many times larger than for a point attachment cathode carrying the same current. Also, the ion current used to heat the cathode does not produce any thrust, hence the thrust per unit current for an ion bombardment cathode will be considerably lower than for a point attachment cathode used in a similar engine configuration. These considerations indicate that considerable effort should be made to develop a reliable point attachment cathode.

Considerable analysis has been made of some idealized models of accelerator cathodes. The important phenomena of electron emission, cathode heating, and cathode heat loss have all been incorporated into the analysis. It was concluded that one of the most important aspects of the "stability" of the attachment is the radial equilibrium of the ions. In a point attachment, the self-magnetic forces can be large



enough to accelerate the ions away from the cathode tip as the cathode jet expands. The ions then move against the electric field and have an outward force exerted on them even though the net radial body force or pinch is radially inward.

b. Cathode Heat Transfer Calculations

To improve the efficiency and lifetime of arc jet cathodes it is important to determine the mode of cathode arc attachment which results in the smallest power losses. Basically the problem may be divided into two categories: geometry of attachment, and form of the energy distribution over the surface of the attachment region.

A comparison was made between a cylindrical "ring" attachment and a "conical tip" attachment. It was assumed that both regions pass the same total current and operate at the same surface temperature (e.g., the melting point of tungsten). The results (derived in Appendix III) indicated that the loss of power to the cathode cooling water is smaller for conical tip attachment than for ring attachment. The numerical value of the power ratio,  $p_{\text{tip}}/p_{\text{ring}}$ , depends upon the half-angle of the cone and the radius of the cathode. The results (see Figure 2) show that for  $\theta = 90^\circ$  (i.e., flat-ended cylinder), this ratio is less than  $1/2$  and for  $\theta = 45^\circ$ , it is less than  $1/4$ . The analysis predicts a ratio of zero in the limit  $\theta \rightarrow 0$ , but it is expected that this heat-conduction model is not valid in this limit since convective effects are certainly important for the case of a long, slender cone.

A comparison was also made between the two limiting cases of energy distribution over a cylindrical attachment region; a delta function energy input (i.e., a "ring" attachment of infinitesimal thickness), and a uniform energy input over the entire surface. These were chosen because the equations could be readily solved and the actual physical situation was felt to be somewhere between these limits.

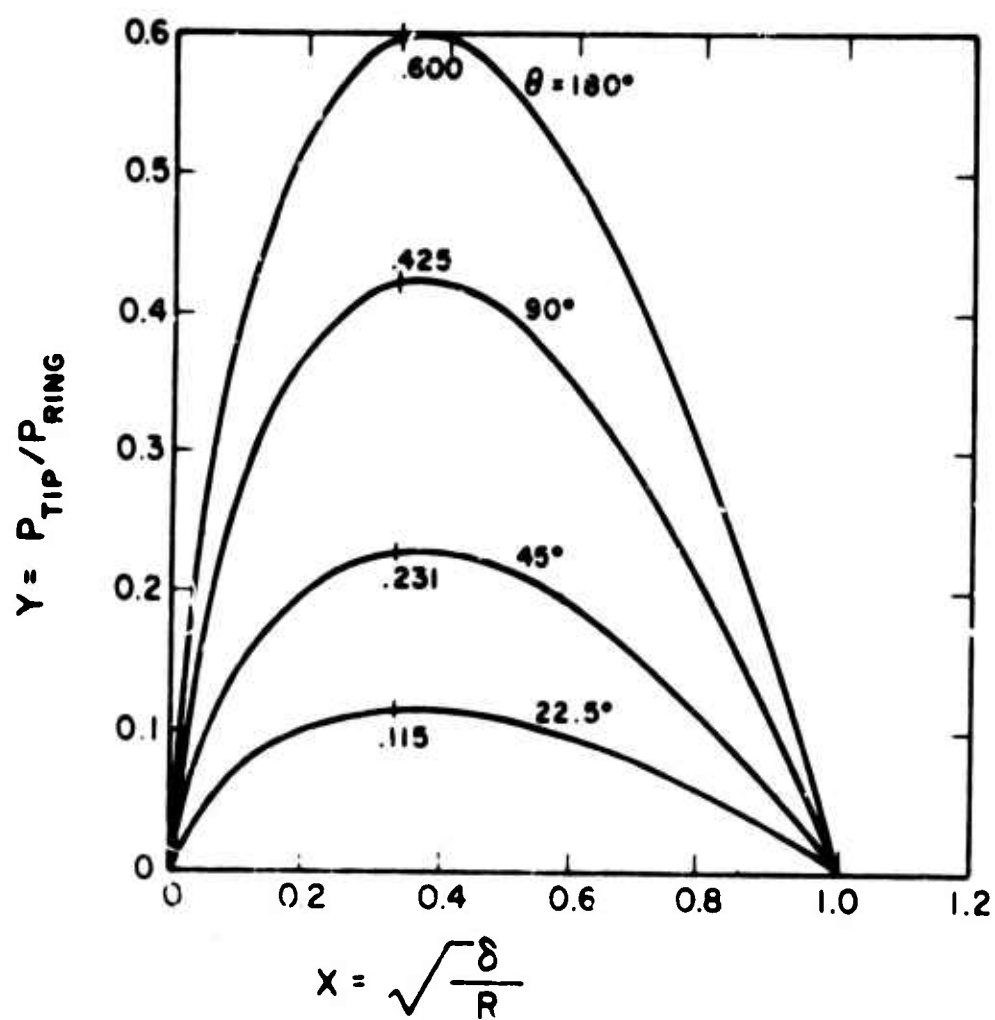


Figure 2 Comparison of Ring and Tip Cathode Attachments

The power loss for the delta function distribution is less than that for the uniform distribution (see Appendix III). The exact power ratio,  $P_{\text{delta}}/P_{\text{uniform}}$ , depends upon the applied arc potential, the surface work function and a complicated integral involving the uniform energy-distribution. A rough approximation of this integral indicates that the power loss for the delta function case can be considerably smaller than that for the uniform case under typical arc jet conditions.

These results therefore indicate that the best possible cathode attachment mode is a point attachment on a conical cathode. Previous experimental results appear to confirm these conclusions.

#### c. Anode Attachment

Investigations are being made to determine the relation between the anode attachment and the ionization phenomena. The possibility of producing a significant percentage of the ions inside of the anode is being studied. If the anode is run hot, e.g., about 3000°K near the attachment region, it is possible to create a reasonable equilibrium ionization level in the propellant vapor as it passes through the anode. If the passage is placed parallel to the magnetic field, then the ions can be exhausted from the anode with the propellant.

An expression for the anode heat loss has been derived which depends upon the gas properties and the specific impulse at which the engine is being operated.

Using a simple model of the anode sheath it is possible to derive the following expression for the power loss to the anode

$$P_A = \frac{10}{3} \frac{T}{\psi} \bar{w}$$

where

$T$  = thrust

$\psi$  =  $\frac{|e| \dot{m}}{m_a I}$

$\bar{w}$  = average axial velocity of the gas near the anode.

This expression exhibits most of the characteristics observed for the anode power loss, provided that  $\psi$  is interpreted as the "effective" value of  $\psi$ .



## SECTION IV

### FACILITY MODIFICATIONS

#### 1. IMPROVEMENTS OF MEASUREMENT TECHNIQUES

During this second phase of the contract improvements have been made in the accuracy, reliability and ease of operation of the propellant feed system that thrust measurement system (thrust balance). The objective has been to achieve 2 percent or less probable error in the measurements of thrust and propellant mass-flow-rate. These efforts and the results obtained to date are presented below. Additionally, the status of development of a feed system with much larger capacity, needed for future endurance tests is presented. The bellows design is not adequate for the high-capacity system and a modified concept discussed below is under development.

##### a. Bellows Feed System Calibration

The bellows feed system calibration included a measurement of the effective displacement area of the bellows as a function of its length, determination of the rate of change of the bellows volume with respect to pressure differential (i.e., actuator force), and a measurement of the bellows spring force as a function of its length. These calibrations used the apparatus described in Ref. 1. The necessity of these measurements is evident from the following equation which expresses the mass-flow-rate of propellant leaving the bellows:

$$\dot{m} = \frac{dm}{dt} = \rho \left( \frac{\partial V}{\partial x} \right) \frac{dx}{dt} + \rho \left( \frac{\partial V}{\partial F^*} \right) \frac{dF^*}{dt} + V \left( \frac{\partial \rho}{\partial T} \right) \frac{dT}{dt} \quad (11)$$

where

$m$  = mass in bellows

$x = (L_{\max} - L)$  = displacement of bellows

$V = V(x, F^*)$  = volume of bellows

$\rho$  = density of liquid in bellows  
 $T$  = temperature of liquid in bellows  
 $t$  = time  
 $F^* = F_a - F_s$  = (bellows actuator force) - (bellows spring force)

The first term is the principal one and the coefficient  $\left(\frac{\partial V}{\partial x}\right)$  is the effective piston area of the bellows. The second term is due to the deflection of the convolutions of the bellows under the pressure force. The third term represents the effect of thermal expansion (primarily of the propellant).

The second term expands to:

$$\rho \left( \frac{\partial V}{\partial F^*} \right) \left( \frac{dF_a}{dt} + \frac{dF_s}{dx} \cdot \frac{dx}{dt} \right)$$

The factors determined by calibration were:

$\frac{\partial V}{\partial x}$  = effective piston area

$\frac{\partial V}{\partial F^*}$  = volume displacement due to pressure differential

$\frac{dF_s}{dx}$  = bellows spring constant

The flow rate is obtained by measuring the actuation rate,  $dx/dt$ , and the actuator force rate  $dF_a/dt$ . The force rate is measured from a strip chart recording of the output of the actuator force transducer. It should be noted that the force rate term is a "correction" term - usually small compared to the first term. The thermal expansion term is kept small by precise control of the temperature - accomplished with the aid of a two-phase tin constant-temperature bath surrounding the feed system.

Figures 3, 4, and 5 show the calibration results in terms of volume as a function of displacement, volume change as a function of actuator force, and spring force as a function of displacement.

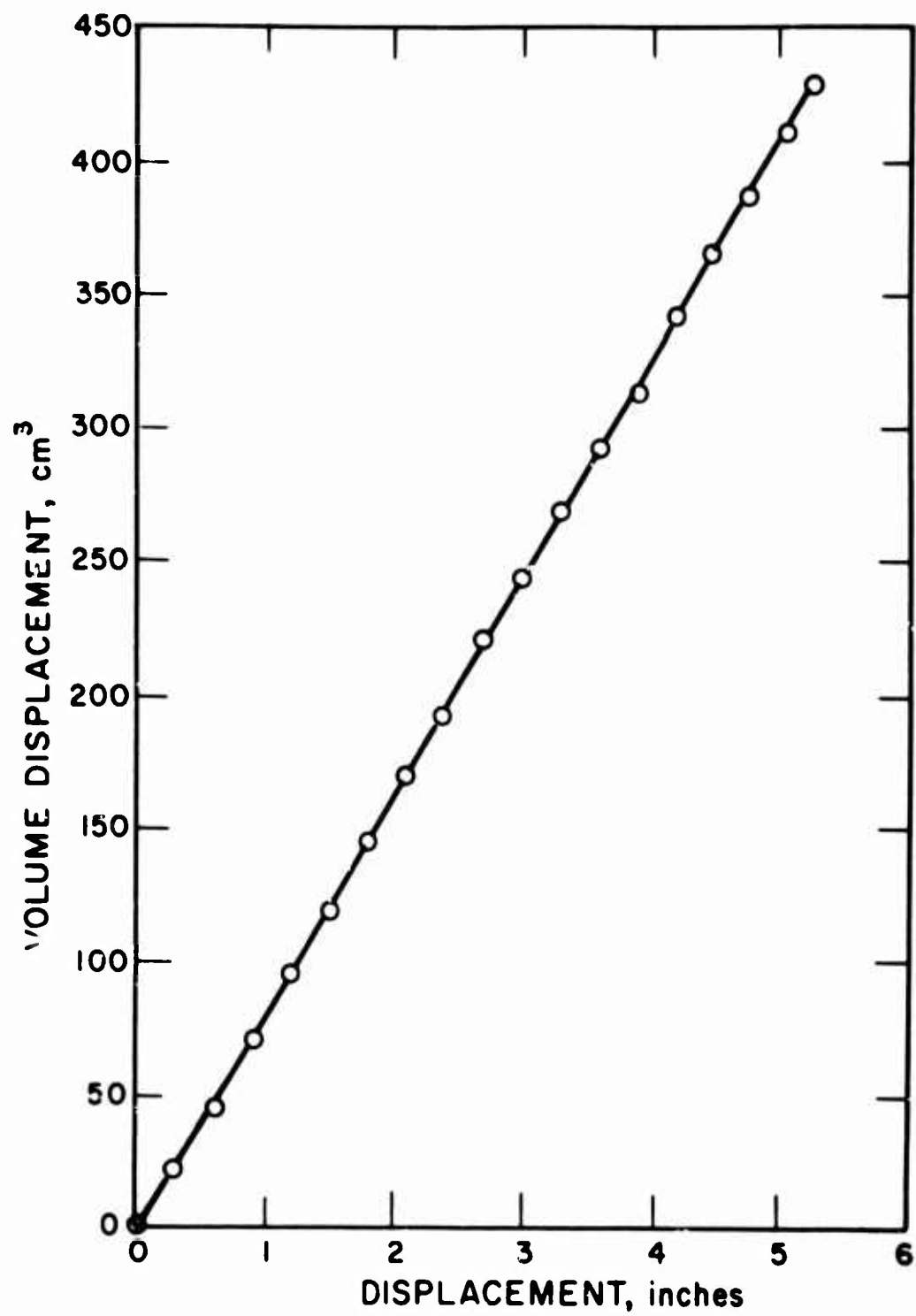


Figure 3 Feed System Bellows — Volume Displacement versus Linear Displacement

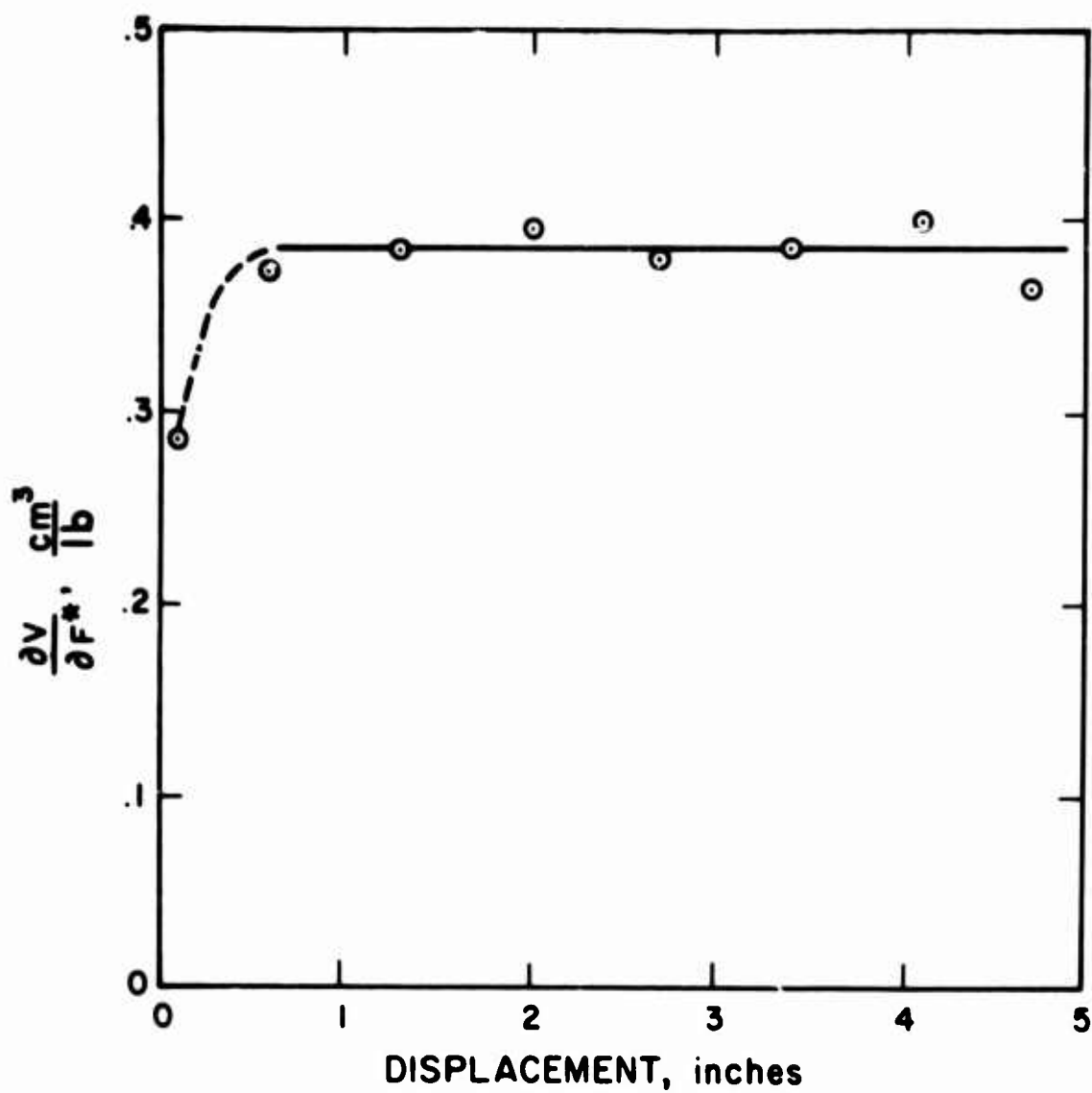


Figure 4 Feed System Bellows - Volume Change Due to Pressure Difference

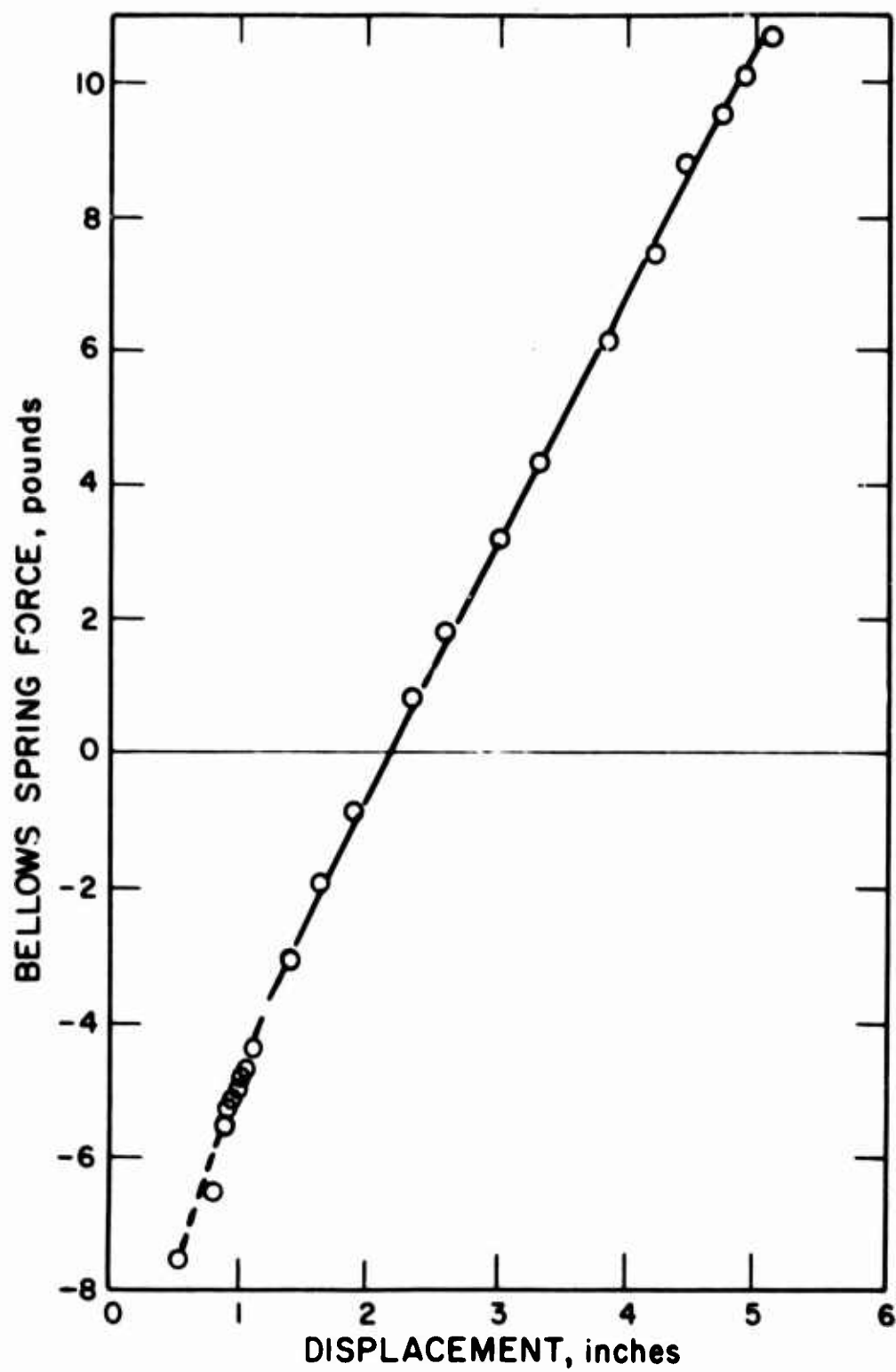


Figure 5 Feed System Bellows Spring Force Calibration

Note that near the fully-compressed position all of these become non-linear. For best accuracy this nonlinear region should not be used in testing. The calibration factors have been determined to an accuracy of 2 percent or better.

b. Vaporizer for Bellows Feed System

The function of the vaporizer is to localize and stabilize the process of evaporation which must occur as the liquid flows from the feed system into the arc. Previous work made no special provisions to control the location of vaporization but depended upon the liquid vaporizing as it flowed into the hot anode. This had the advantage of simplicity and more effective regenerative cooling. However, the vaporization was frequently unstable and the flow into the arc would pulsate. An additional bad feature of vaporization in the anode was the frequent occurrence of "flooding" at the beginning of runs when an excessive amount of liquid would flow into the space between cathode and anode.

These difficulties have been relieved, at least with potassium propellant, by the vaporizer shown in Figure 6. The essential feature of this vaporizer is a steep temperature gradient which localizes and stabilizes the vapor front in the porous plug. The temperature gradient results from the heating coils located on the upper end, the low heat conductance of the tube-porous-plug assembly, and the radiation from the exposed, unheated section of the vaporizer.

Another feature of this system is that it operates at low pressures (a few psi). Thus, changes and rates of change of pressure with respect to time are low, and the force-rate correction term (second term in Eq. 11) is small. This enhances the accuracy of mass-flow-rate measurements.

Though this vaporizer in combination with the bellows feed system operated satisfactorily with potassium, difficulties were encountered with lithium due to its higher vaporization temperature. Neither the tantalum heater coils nor the seal between the vaporizer



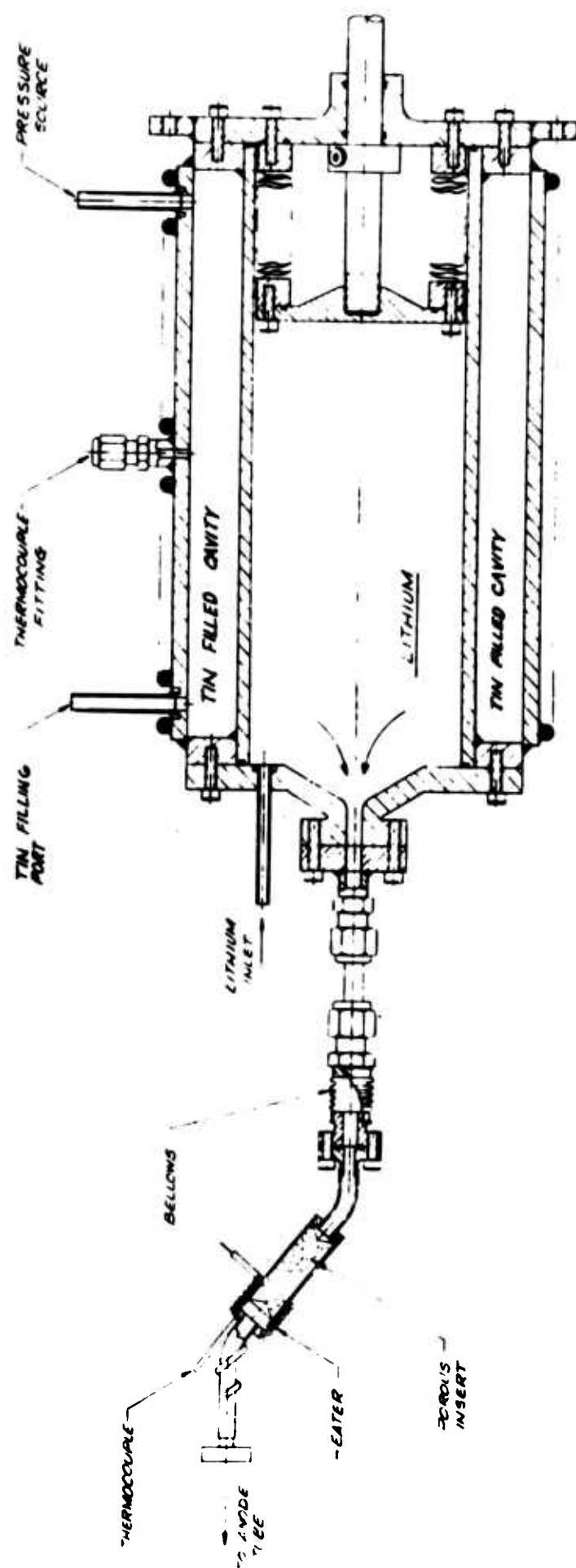


Figure 6 MK-1B Lithium Feed System and Vaporizer



and engine were reliable at the temperature ( $\sim 1500^{\circ}\text{K}$ ) required for lithium vaporization especially at the higher pressures ( $> 0.5 \text{ atm}$ ) necessary for the buffer-fed engine described in Section VII. For lithium the vaporizer was brazed directly to the anode so that heat transferred from the arc discharge to the anode could be used for vaporizing. This arrangement is shown in Figure 7, with the CG engine configuration.

c. High-Capacity Feed System

A concept for a high-capacity feed system as shown schematically in Figure 8 is currently under development. This approach is based on equilibrating the vapor pressure above the lithium in the vaporizer to the pressure of argon gas above the liquid reservoir. Under this condition the sonic vapor flow-rate through the exit orifice is proportional to the applied gas pressure which can be easily measured with a pressure gauge. To meet this condition the system must have the following characteristics:

1. The liquid surface temperature (and hence vapor temperature) must increase as the gas pressure is increased and as the level of the liquid in the vaporizer moves up.
2. The hydrostatic pressure of the liquid column and the pressure drop due to the steady-flow should be low (less than 1 percent) compared with the vapor pressure.
3. The amplitude of pressure fluctuations must be small compared with the vapor pressure, or the system should be linear or symmetrical so that the average of the unsteady pressure component is negligible.

Compared to alternate techniques, this design eliminates the requirements of measuring pressure at high-temperature, deducing pressure from temperature, or measuring and controlling the liquid level. An additional benefit is the location of the heaters in the argon environment which minimizes oxidation and embrittlement of the heater materials.



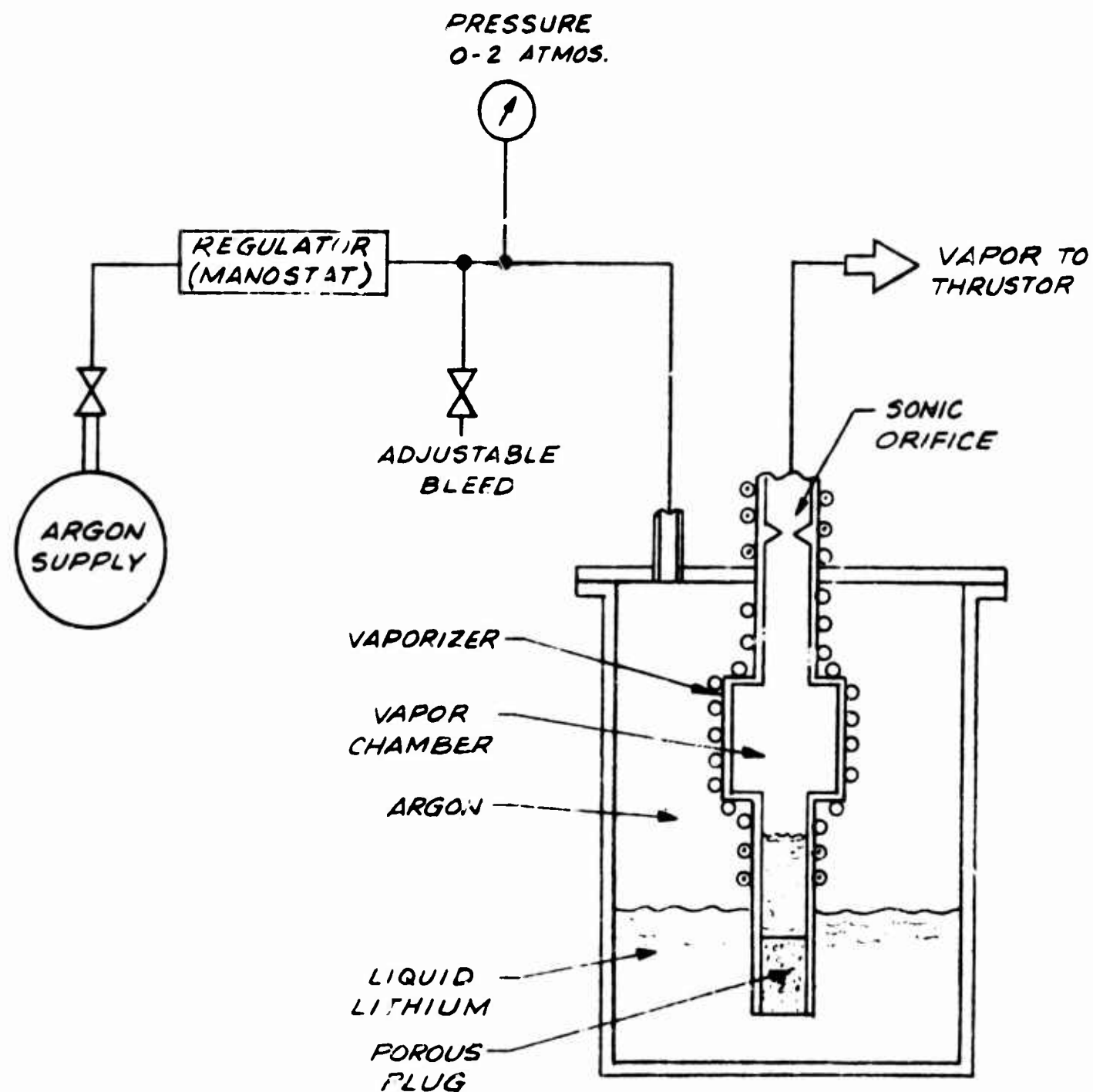


Figure 8 Lithium Feed System

One possible disadvantage is that the process tends to be unstable and some means for damping oscillations is necessary. Because of the stability problems a simple Pyrex model of the system was built and tested. The tests showed that stability could be achieved by providing viscous damping in the tube below the vaporizer and by providing a steep temperature gradient in the vaporizer region.

Figure 9 illustrates major parts of the final design. Operation of the system is initiated by the argon gas pressure in the reservoir which forces liquid lithium through the porous plug and up the liquid feed tube into the vaporizer section. The liquid flow is here divided into four 0.060 diameter passages in the molybdenum body which is enclosed in concentrated tantalum-sheathed heaters. The high lithium surface area-to-volume ratio and relatively large heat storage capacity of the body force vaporization to occur in this region. The vapor is superheated by heaters attached to the vapor reservoir to prevent condensation in the sonic orifice.

An important consideration in the design of the lithium feeder was elimination of the instability observed in the Pyrex water-models. This instability, in the form of large liquid oscillations in the feed tube, was promoted by an unrestricted liquid column driven at each end by compressible gas, steam on the top and argon on the bottom. Also, lack of a sharp temperature gradient in the region of vaporization allowed boiling below the liquid surface.

Three components have been specifically designed to minimize this form of instability in the lithium system. A porous nickel plug, which presents a negligible restriction to normal lithium flow rates, is attached to the lower feed tube to dampen large flow fluctuations. A steep temperature gradient in the vaporization region is established by the concentrated heaters and multiple small diameter passages. The vapor pressure fluctuations should be partially damped by the large volume above the vaporizing section. An additional stabilizing factor in the lithium system, as compared with the water model, is the higher

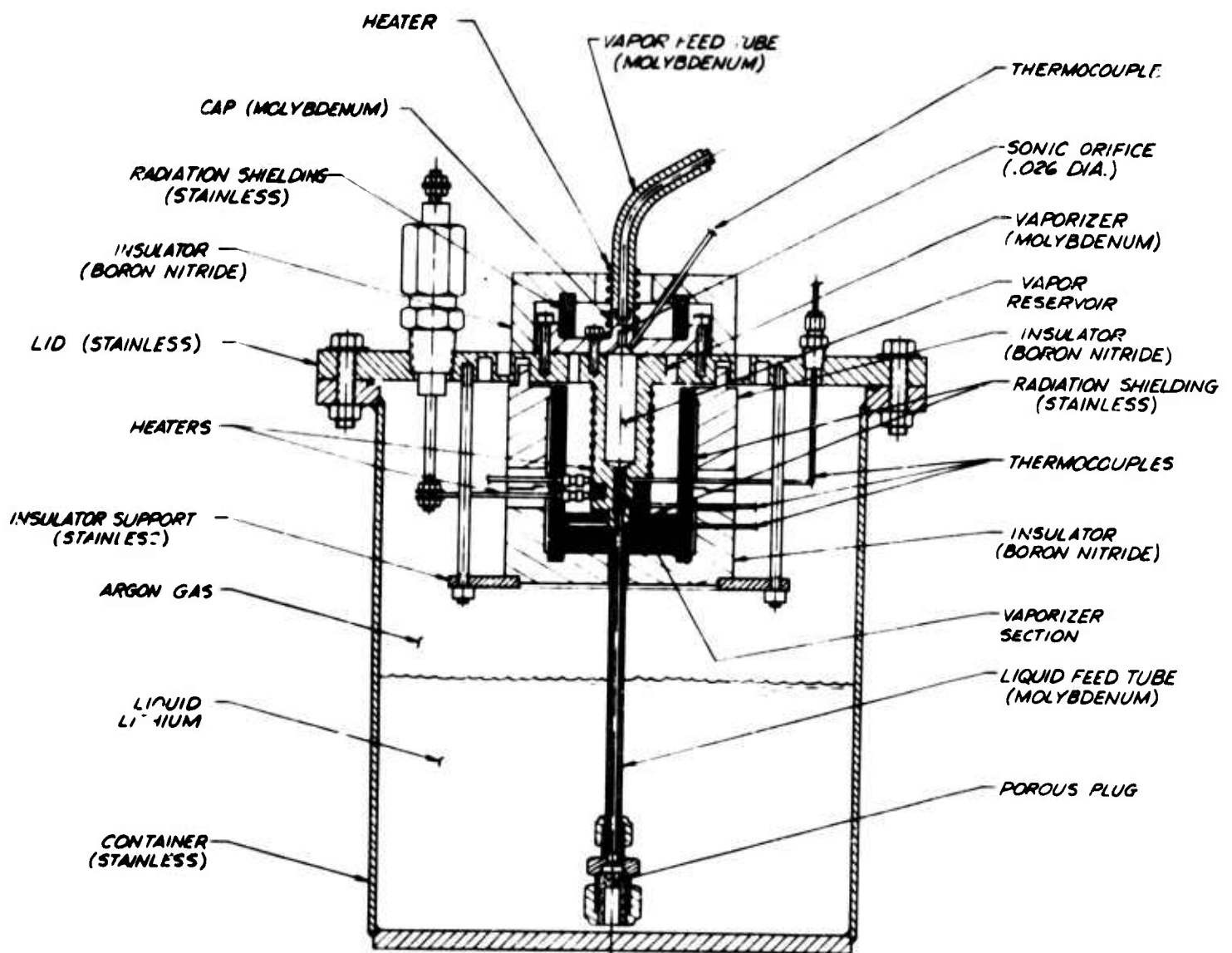


Figure 9 Lithium Feed System - Model LV 4-1

thermal conductivity of the liquid. Due to the high thermal diffusivity and high critical nucleate boiling heat flux of lithium, boiling beneath the liquid-to-vapor face will be minimized.

Two tests of the lithium vapor feed system were performed. The first test, with the configuration shown in Figure 9 failed at  $1150^{\circ}\text{K}$  due to burn-off of the heater end-termination.

Several modifications of the vaporizer were designed to eliminate these problems for the second test. Larger size tantalum heater wire (0.104 O.D., 0.042 diameter conductor) was selected to permit higher input powers and to avoid fragile constructions. New heater end-terminations were designed around three criteria: high structural strength by attaching the sheath to a massive body extension, support for the inner conductor by close-fitting concentric insulators, and elimination of excessive heating at the conductor-lead wire junction by increased contact area and heavy heat sink attachment. Tungsten-rhenium thermocouples were used for greater reliability of the temperature measurement.

This configuration was successfully temperature-cycled several times to  $1350^{\circ}\text{K}$  but failed while maintaining the required design temperature of  $1700^{\circ}\text{K}$ . This level was chosen to permit operation of the argon-driver system at two atmospheres pressure. The heater failure was attributed to lack of sufficient heat conduction from the outer sheath at a point of poor contact with the vaporizer body.

Alternate heating methods were investigated in order to increase the system reliability. Radiation heating from bare tungsten wire, electron bombardment, and radio-frequency induction heating were considered. It was decided to test the concept using a vaporizer closely coupled to the anode prior to testing an alternate heating method. This vaporizer is similar to that shown in Figure 9 with the exception of the heating coils which were eliminated in favor of heating the vaporizer directly by the anode.



## 2. THRUST BALANCE IMPROVEMENTS

Efforts to improve the accuracy of thrust measurement were concentrated on:

1. Reduction of tare forces due to the interaction between the applied magnetic field and current leads.
2. Reduction of forces caused by cooling-water pressure, flow and temperature changes.

The effects of the magnitude and variation of these forces are the principal sources of error in a thrust measurement.

To reduce the electromagnetic tare forces, the power lines to the thruster electrodes and the magnet coil were transmitted across the balance coaxially. As in previous balance designs, these connections are made through mercury to avoid interference of rigid power cables. Two coaxial mercury pots were designed, fabricated, tested, and incorporated into the existing balance during the reporting period. Figure 10 includes a sketch of the coaxial mercury pot design.

For reduction of the forces caused by coolant flow across the balance the U-tube arrangement shown in Figure 10 was adopted. The U-tube concept allows thermal expansion of a metal tube without a force on the balance by connecting the ends of the tube at the same vertical position - one side to the suspended balance platform and the other side to the fixed balance support. Bench tests showed that the relative position between the inlet and outlet of the tube did not shift measurably (less than  $5 \times 10^{-4}$  in.) with changing temperature and pressure in the tube. Subsequent tests of a single coolant circuit (two U-tubes) mounted temporarily on the balance showed that the maximum force due to water pressure and flow was about one gram. Five such circuits (10 U-tubes) were permanently mounted on the existing balance along with the coaxial mercury pots.

After completing these modifications, the force tare due to water flow and pressure was reduced to about 1 gram compared to 10 to 20 grams before modification. The coaxial mercury pots reduced the magnetic tare force from about 50 grams to about 5 or less. As a result of these improvements the balance is considerably more stable and accurate.



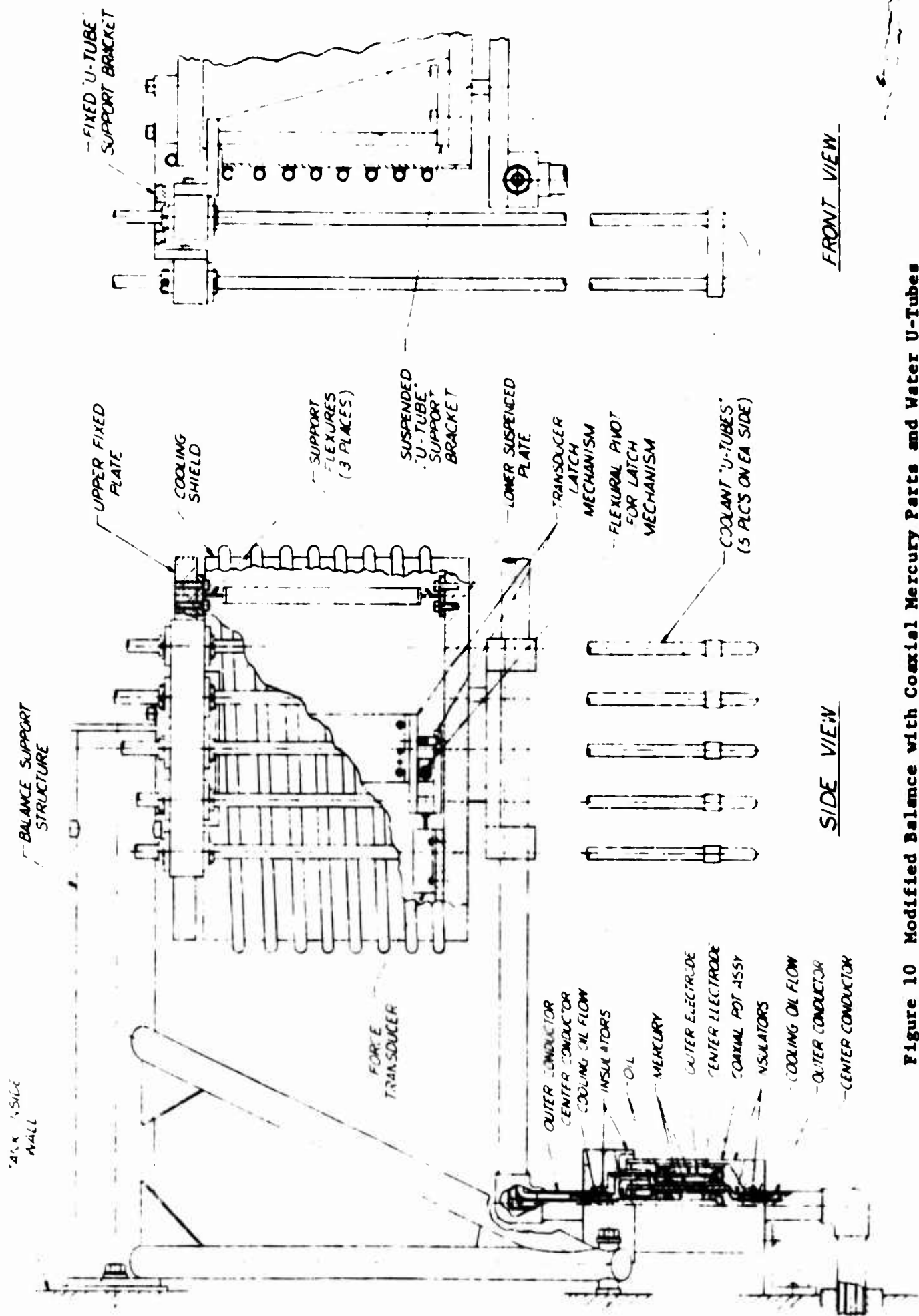


Figure 10 Modified Balance with Coaxial Mercury Parts and Water U-Tubes

## SECTION V

### HIGH VACUUM TESTS

#### 1. HIGH-VACUUM TESTS OF A LITHIUM THRUSTOR

The high-vacuum tests were conducted as one step in the process of determining the effect of test chamber pressure on thruster performance so that the pressure level necessary for adequate space simulation can be assessed. Additional data were later obtained in the 6 ft x 6 ft chamber by measuring the thrust as a function of pressure over a range from  $10^{-4}$  to  $10^{-2}$  torr. These results are presented in Section VII. A Model LAJ-AF-6D lithium arc jet shown in Figure 11 was tested in the ion engine 5 ft x 12 ft (5 ft diameter by 12 ft long) vacuum chamber at pressures down to  $2 \times 10^{-7}$  torr. For the tests in the 5 ft x 12 ft chamber the thruster and lithium feed system were mounted on the same thrust balance used with tests in the 6 ft x 6 ft chamber. Figure 12 shows the thrust balance and Figure 13 shows the balance, thruster and feed system mounted in the 6 ft x 6 ft chamber. The temporary installation in the 5 ft x 12 ft chamber was similar to that shown by Figure 12.

The thruster tested at high vacuum was identical to the one endurance-tested for 10 hours as reported in Ref. 1. In the 5 ft x 12 ft chamber the thruster was operated at the same current and at about the same mass-flow-rate used in the life test. The thrust and voltage were close to those measured during the endurance test in the arc jet 6 ft x 6 ft chamber at  $6 \times 10^{-3}$  torr.

Table I lists the results from both the high-vacuum tests and the previous tests at higher pressures. Although the thrust level in the high-vacuum tests was about the same as in the higher pressure test, the efficiency was slightly lower due to the higher mass-flow-rates.

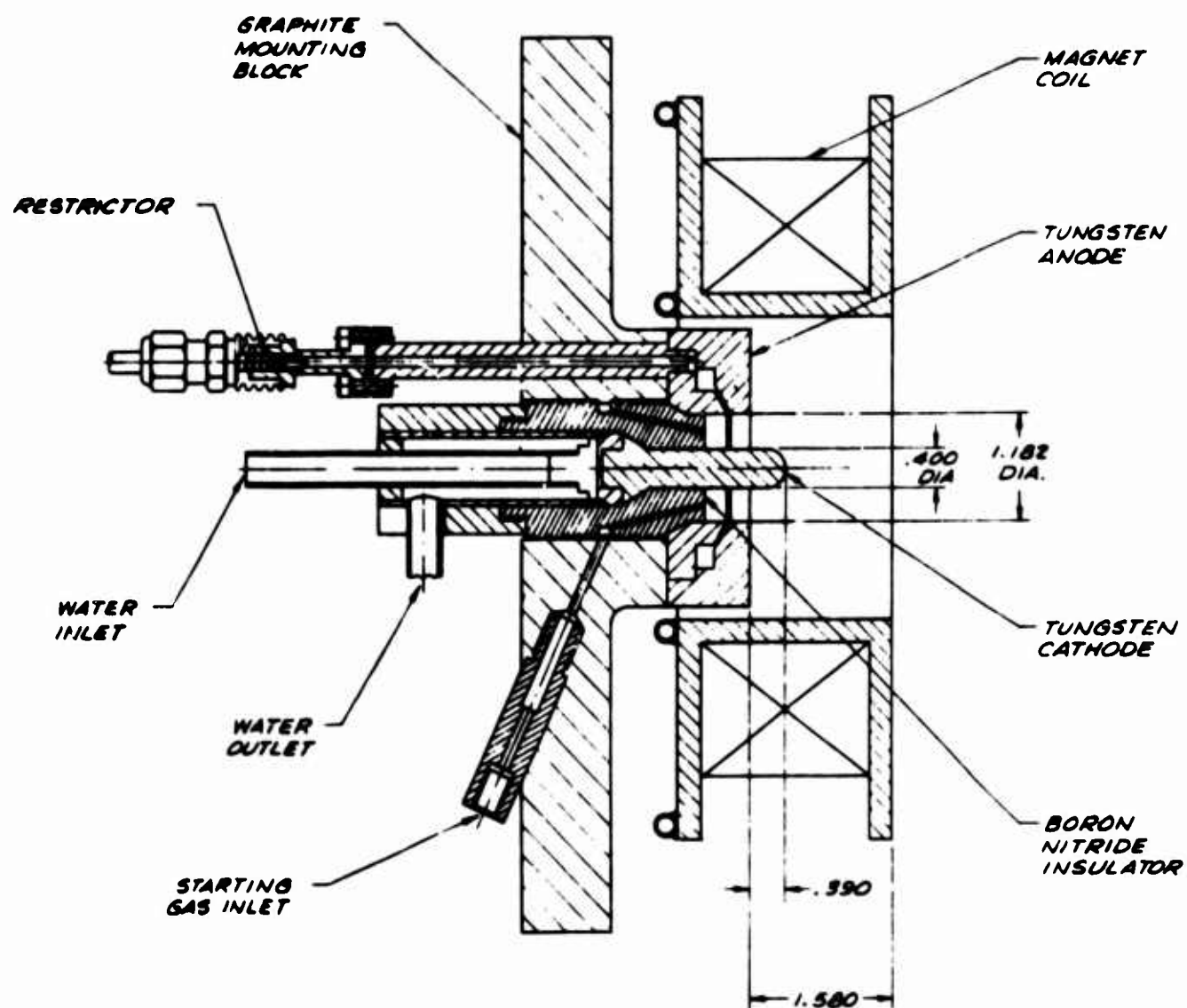


Figure 11 Arc Jet Model LAJ-AF-6D

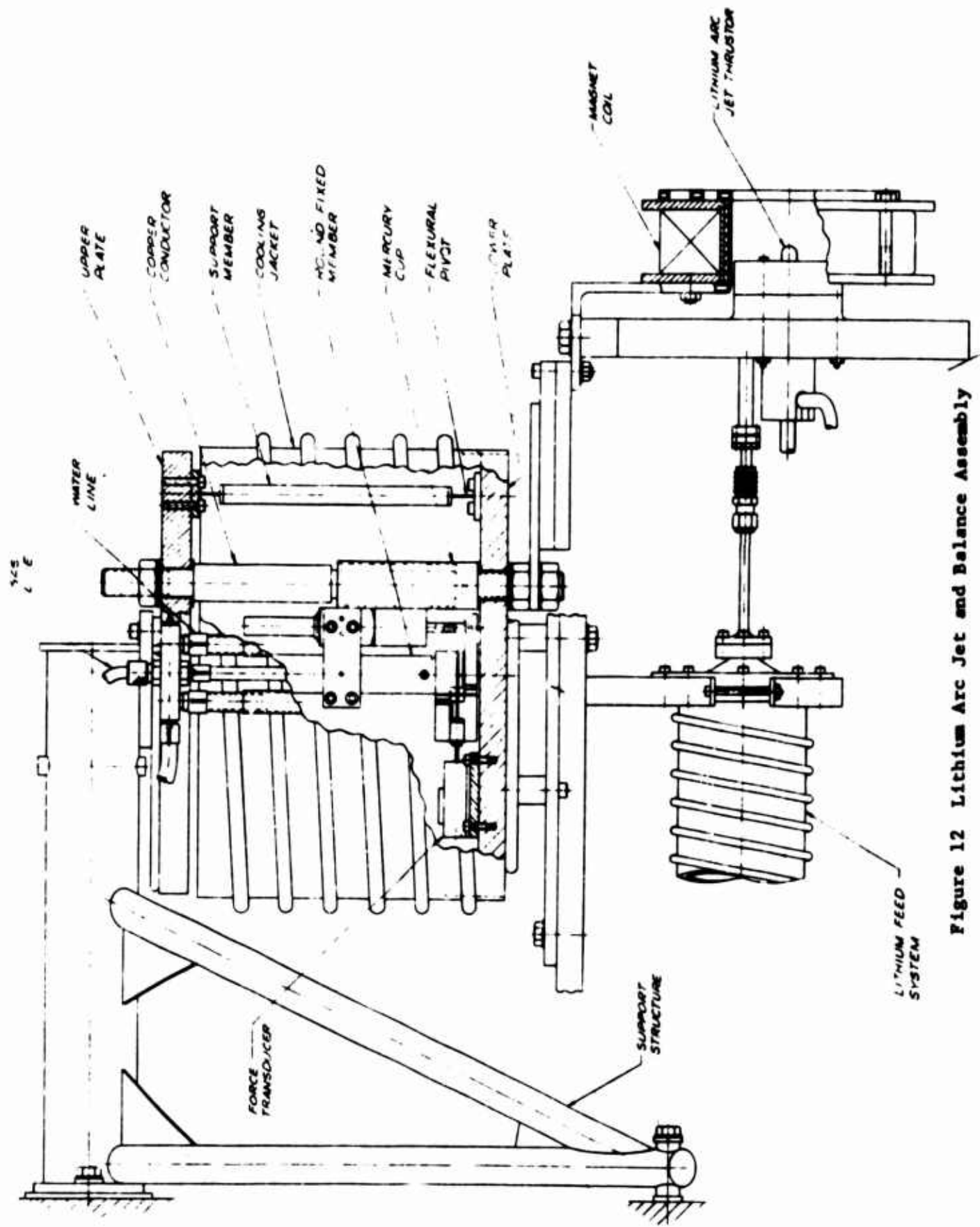


Figure 12 Lithium Arc Jet and Balance Assembly

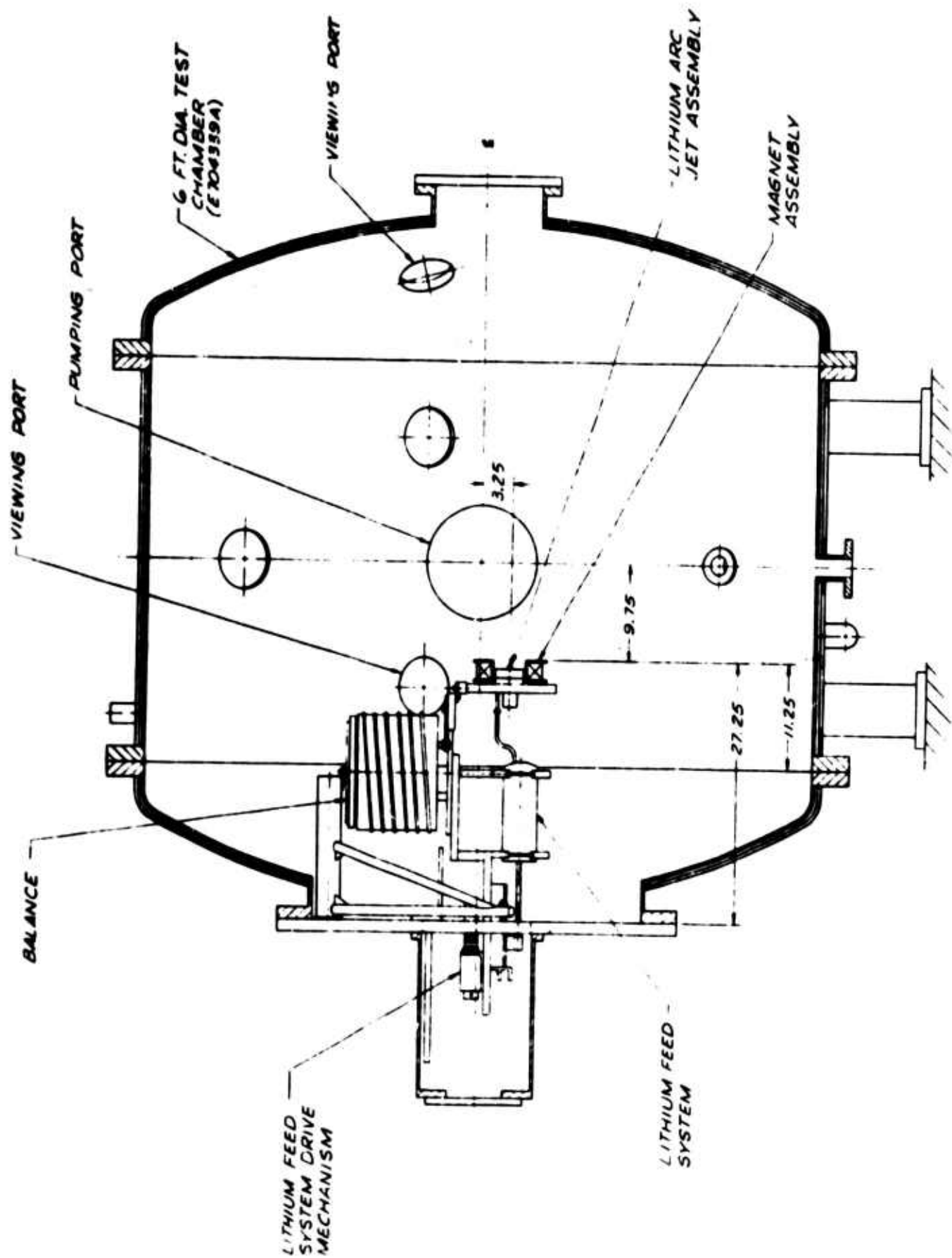


Figure 13 Lithium Arc Jet 6-Ft-Diameter Test Chamber



TABLE I HIGH VACUUM TEST RESULTS

<u>Arc Current (amps)</u>	<u>Arc Voltage (volts)</u>	<u>Power Input (kw)</u>	<u>Coil Current (amps)</u>	<u>Thrust (grams)</u>	<u>Mass Flow Rate (grams/sec)</u>	<u>I<sub>ap</sub> (acc)</u>	<u>Efficiency</u>	<u>Tank Pressure (mm-Hg)</u>
250	40	10.0	1800	22.5	0.00453	4950	0.53	$6 \times 10^{-3}$
250	42	10.5	1800	24.4	0.0054	4540	0.51	$2 \times 10^{-7}$
250	40	10.0	1800	22.8	0.0058	4040	0.44	$3 \times 10^{-7}$
250	42	10.5	1800	22.8	0.0058	4110	0.45	$2 \times 10^{-7}$



The high-vacuum test was stopped when the arc attached to the condenser baffle plates connected to the liquid-nitrogen-cooled liner adjacent to the wall of the tank. This attachment was caused apparently by the buildup of lithium condensed on the baffles. The baffles were removed and additional tests were attempted; however, the power density to the liner was then excessive and the liquid nitrogen in the liner boiled. As a result the test chamber pressure fluctuated over a large range. The test was stopped because of the danger of over-pressurizing the liner due to liquid nitrogen boiling.

## SECTION VI

### POTASSIUM PERFORMANCE MEASUREMENTS

Potassium was investigated as a propellant in the Hall arc jet because of its potentially higher frozen-flow efficiency. Assuming the predominant energy loss to be ionization and further that all propellant atoms are ionized only once, the propellant with lowest loss and highest efficiency is the one with the lowest first ionization potential per atomic mass unit. Among the alkali metals this ratio,  $V_I/m_a$ , is higher for higher atomic-weight elements. On the other hand, for higher atomic weights the second ionization potential,  $V_{II}$ , is lower, the kinetic energy for a given specific impulse is higher, and the number density of the plasma is higher for the same power density and specific impulse. Therefore, second ionization and energy losses, in addition to first ionization losses, are most likely to occur with higher atomic weight. Since it was not possible to evaluate these effects and calculate the efficiencies on the basis of data with other propellants, the potassium experiments were carried out.

The results were quite different from predictions based on first-ionization energy losses. The efficiency was lower than with lithium at the same specific impulse and the maximum specific impulse attainable was only 1500 sec compared to 6000 to 8000 sec with lithium.

To eliminate geometry effects from the comparison of lithium and potassium, the same thruster configuration (Model LAJ-AF-6D, Figure 14) was used with both propellants. This eliminated one ambiguity in the results but may have created another since that configuration was developed for lithium. It is possible that through a systematic variation of thruster geometric parameters using potassium, improvements in performance could be found, and the performance characteristics might compare differently. The principal geometric variable of

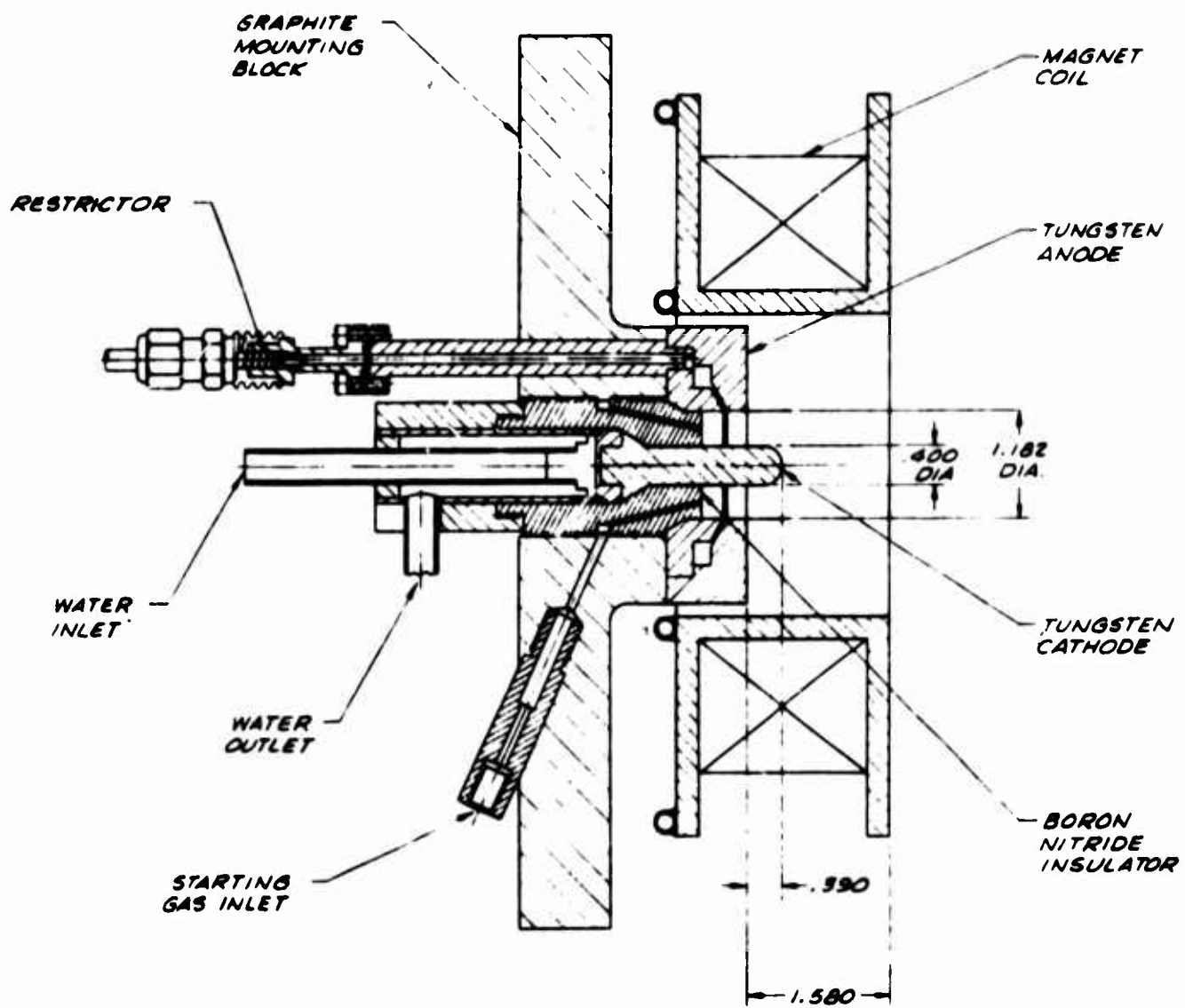


Figure 14 Arc Jet Model LAJ-AF-6D

concern is the jet diameter, which directly affects the number density of the plasma in the acceleration region. This points out the need for additional fundamental understanding and analytic parameters to describe the effects of geometry and propellant properties on the thruster performance.

Although the studies of potassium performance did not include variations of geometric parameters, the effects of the magnetic field strength, arc current, and test chamber pressure on thrust, total arc voltage, tank floating voltage, and anode power loss, were measured.

As Figure 15 shows, the specific impulse was varied over the range of about 600 to 1600 seconds. The corresponding thrust efficiency varied from about 12 percent to 28 percent. Note that the thrust efficiency increases with specific impulse when the specific impulse is less than about 1200 sec, but does not appear to increase between 1200 and 1700 sec. This asymptotic behavior may indicate the beginning of second ionization. This maximum specific impulse is related to the tendency of the thrust to decrease as the mass-flow-rate is decreased at constant arc current.

The results of Figure 15 were measured in a chamber-pressure range ( $2 - 8 \times 10^{-4}$  torr) where the thrust is independent of pressure level. Figure 16 shows thrust as a function of chamber pressure over a range from  $10^{-4}$  to  $10^{-1}$  torr. These results are approximate because they were obtained in a transient condition during which the pressure was first increasing and then decreasing. The pressure was varied by bleeding argon into the chamber. The sequence was begun at the point indicated by (1) on Figure 16. The pressure rapidly rose and the thrust decreased to a minimum value and then increased. Beginning at point (2) (Figure 16) pressure was recorded as a function of thrust. The pressure rose to  $10^{-1}$  torr (at point (3)) and then began to drop. The thrust was maximum roughly at the maximum pressure and then dropped as the pressure decreased. The thrust reached a minimum at about  $2 \times 10^{-2}$  torr (point (4)) and then increased to an apparent asymptotic

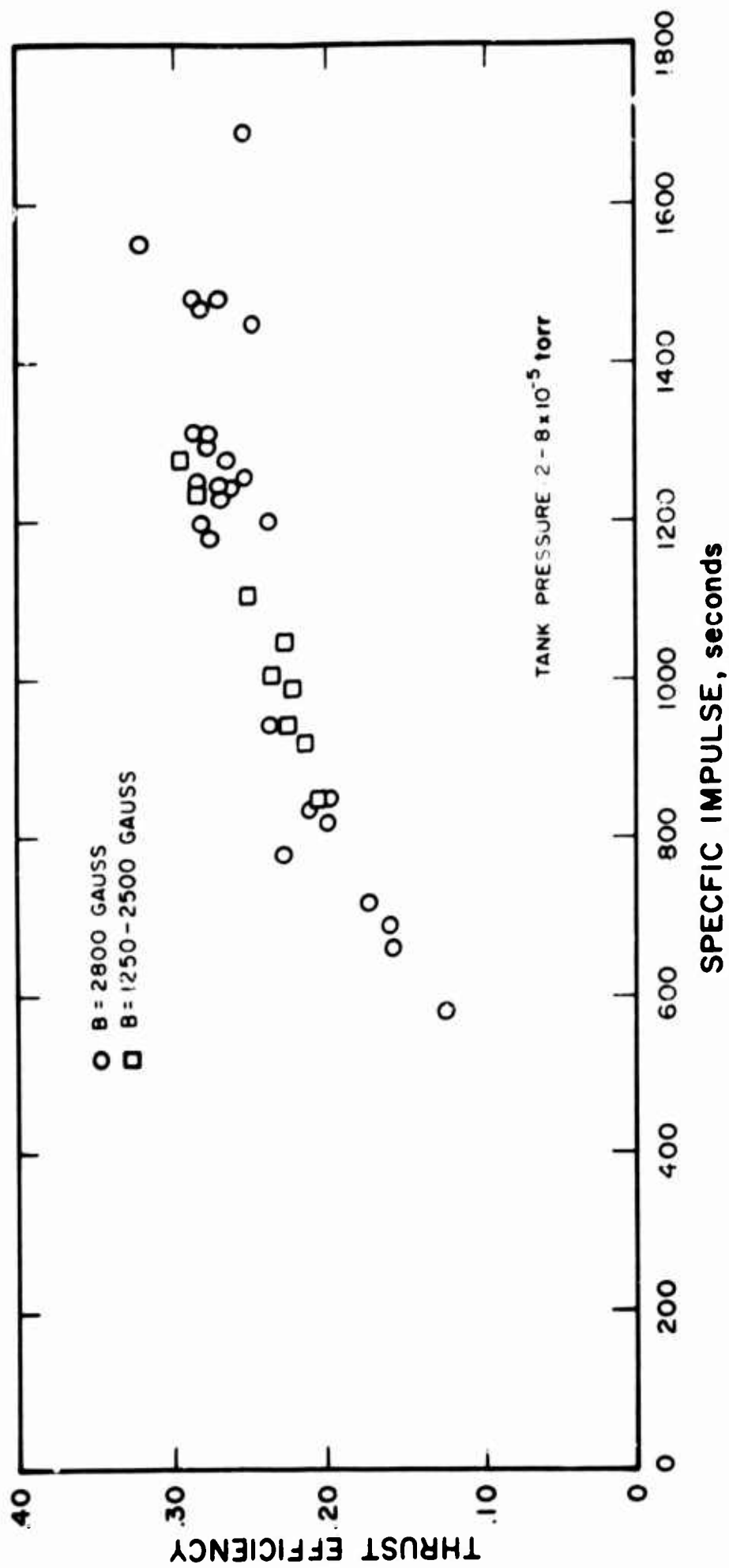


Figure 15 Hall Arc Jet Performance With Potassium

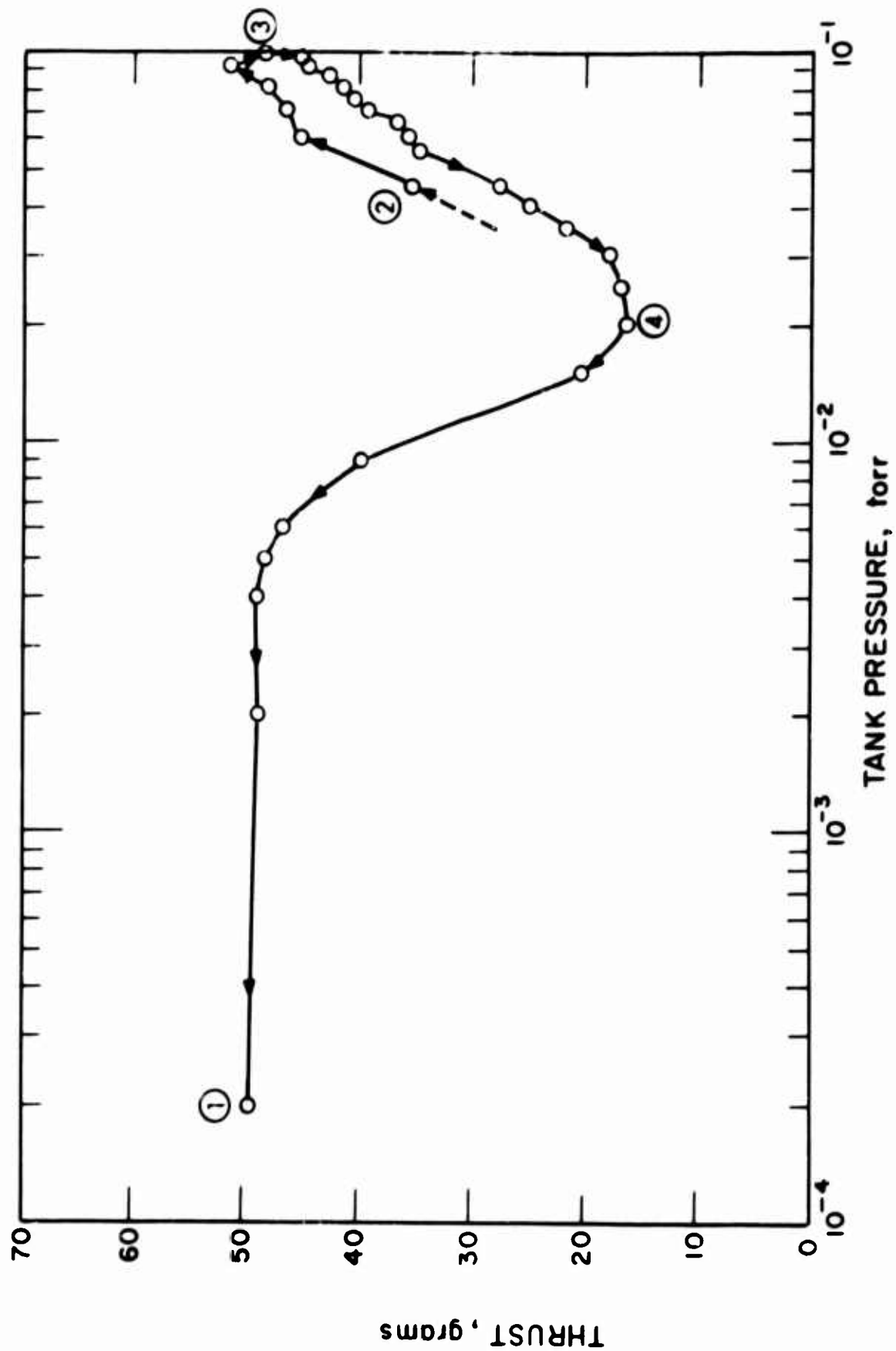


Figure 16 Thrust versus Tank Pressure with Potassium



level at about  $4 \times 10^{-3}$  torr. (Pressures above  $10^{-3}$  torr were measured with a thermocouple type vacuum-gauge and below  $10^{-3}$  torr with an ionization gauge.)

It appears that in the region to the right of the asymptotic level of pressure, gas is entrained at a significant rate into the acceleration region of the discharge. The asymptotic level probably varies with the thruster operating conditions, and should be investigated further.

The effects of magnetic field strength on thrust and voltage are shown in Figure 17. The thrust increased with increasing magnetic field up to about 2500 gauss. Above 2500 gauss the behavior is not clear because of insufficient data; however, it appears that the thrust is independent of field strength, or may reach a maximum and then decrease with increasing field strength. This tendency may also be due to the onset of second ionization. As Figure 17 shows, the total arc voltage increased with increasing magnetic field strength from about 24 volts at 1200 gauss to about 40 volts at 2800 gauss.

Figure 18 shows the effect of the magnetic field strength on the voltage measured between the anode and the tank and between the tank and the cathode. Similar measurements with sodium<sup>1</sup> as the propellant are shown for comparison. As Figure 18 shows, the anode-to-tank voltage increases with magnetic field strength while the tank-to-cathode voltage appears to be independent of the magnetic field. Since the tank floats near the cathode potential or at least near the potential of the cathode jet, this result seems to indicate that the conductivity along the cathode jet is independent of the magnetic-field strength.

Figure 19 shows a correlation of the power loss to the anode for both potassium and sodium.<sup>1</sup> Note that the anode power loss divided by the arc current has the same value for sodium and potassium when the straight lines through the data are extrapolated to zero field

---

<sup>1</sup>Sodium measurements were made on NASA Contract NAS3-5909

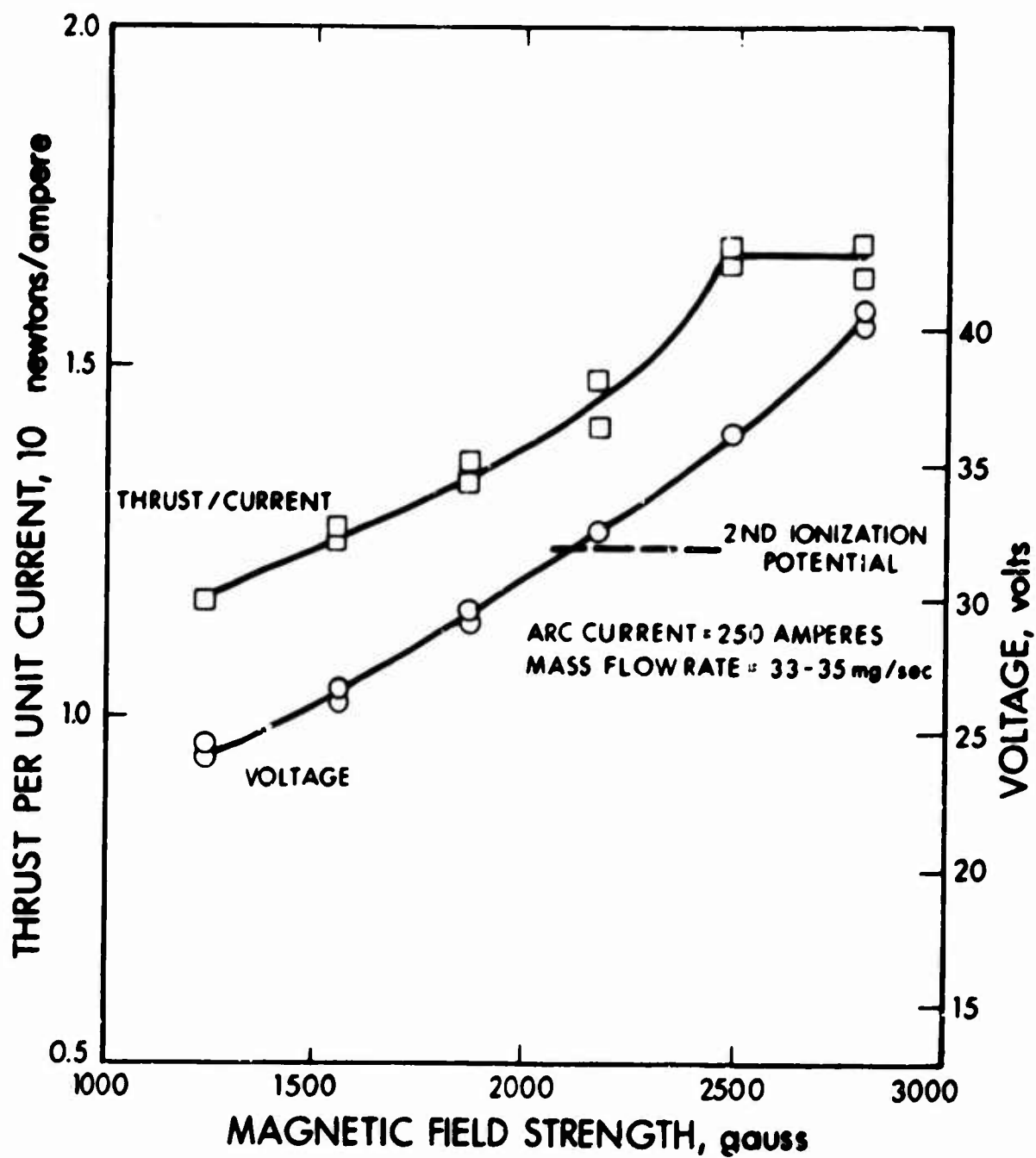


Figure 17 Effect of Magnetic Field Strength on Thrust and Voltage for Potassium

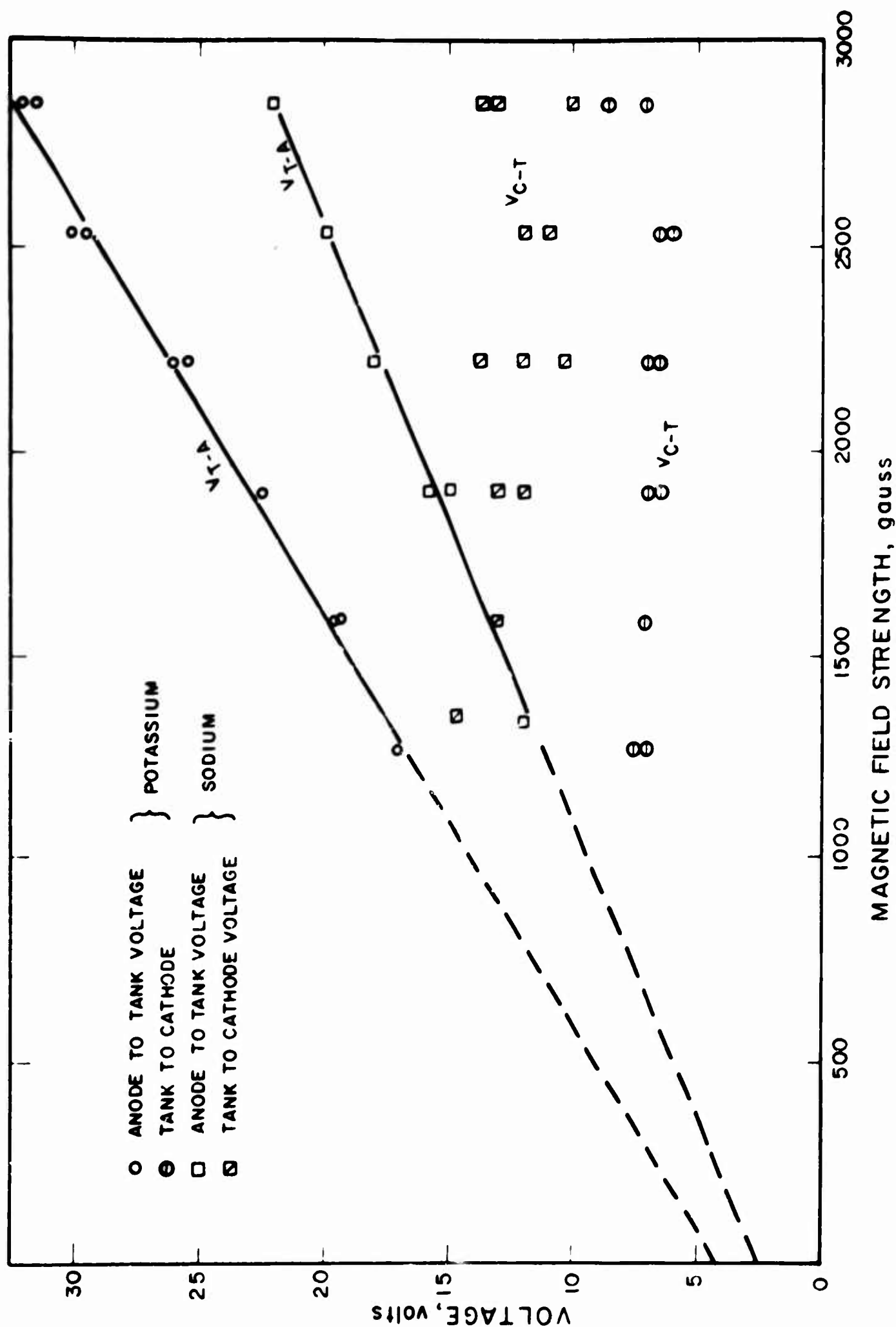


Figure 18 Effect of Magnetic Field on Arc Potentials for Sodium and Potassium

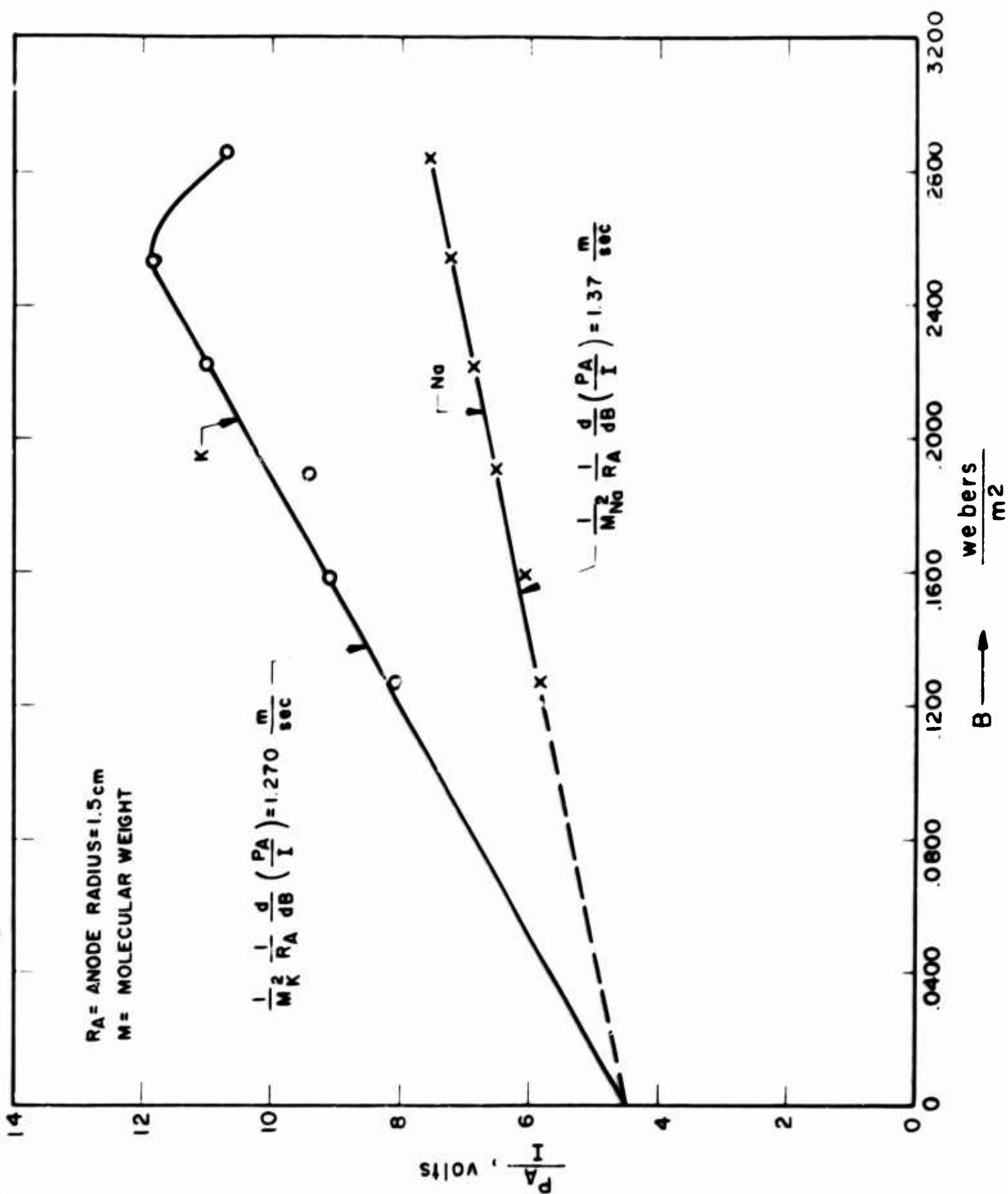


Figure 19 Effect of Magnetic Field Strength on Anode Power Loss for Sodium and Potassium.

strength. Also, the slopes for potassium and sodium differ in magnitude approximately by the inverse of the square of their molecular weights. This may be a coincidental rather than a universal relationship since the mass-flow-rate, arc current, and values of  $\psi$  were different for the two propellants.

Power loss to the cathode as a function of the arc current is shown in Figure 20. The power loss depends primarily on the arc current and as the data show it is relatively insensitive to the mass-flow-rate and magnetic field strength. The average power loss divided by the arc current (apparent cathode voltage drop) is about 5 volts.

Thrust varies about linearly with arc current as Figure 21 shows. The maximum current during these runs was 400 amperes where the cathode-anode insulator and the cathode began to erode. Figure 22 shows the thrust per unit current and total arc voltage for potassium plotted as a function of the parameter  $\psi = \frac{e \dot{m}}{m_a I}$ . This parameter seems to correlate the data reasonably well. A region ( $\psi > 0.35$ ) is indicated where the thrust per unit current is independent of  $\psi$ . In the region where  $\psi < 0.35$  the thrust per unit current decreases with decreasing  $\psi$ , i.e., with decreasing mass-flow-rate or increasing current. The arc voltage decreases with increasing  $\psi$  as the analysis of Ref. 6 predicts.

For the potassium experiments the thruster and feed system were mounted directly on a thrust balance (described in detail in Ref. 1) and installed in the 6 ft x 6 ft test chamber. The arrangement was identical to that used in tests of the Model AF-6D lithium engine of Ref. 1. The variables measured were thrust, mass-flow-rate, arc current and voltage, magnet-coil current and voltage, test chamber pressure, and heat transfer to the coil, cathode, anode, and test chamber.

Since the anode was radiation-cooled it was necessary to use an oil-cooled shield to absorb the radiation from the anode radiation fin. This shield intercepts only the radiation from the rear

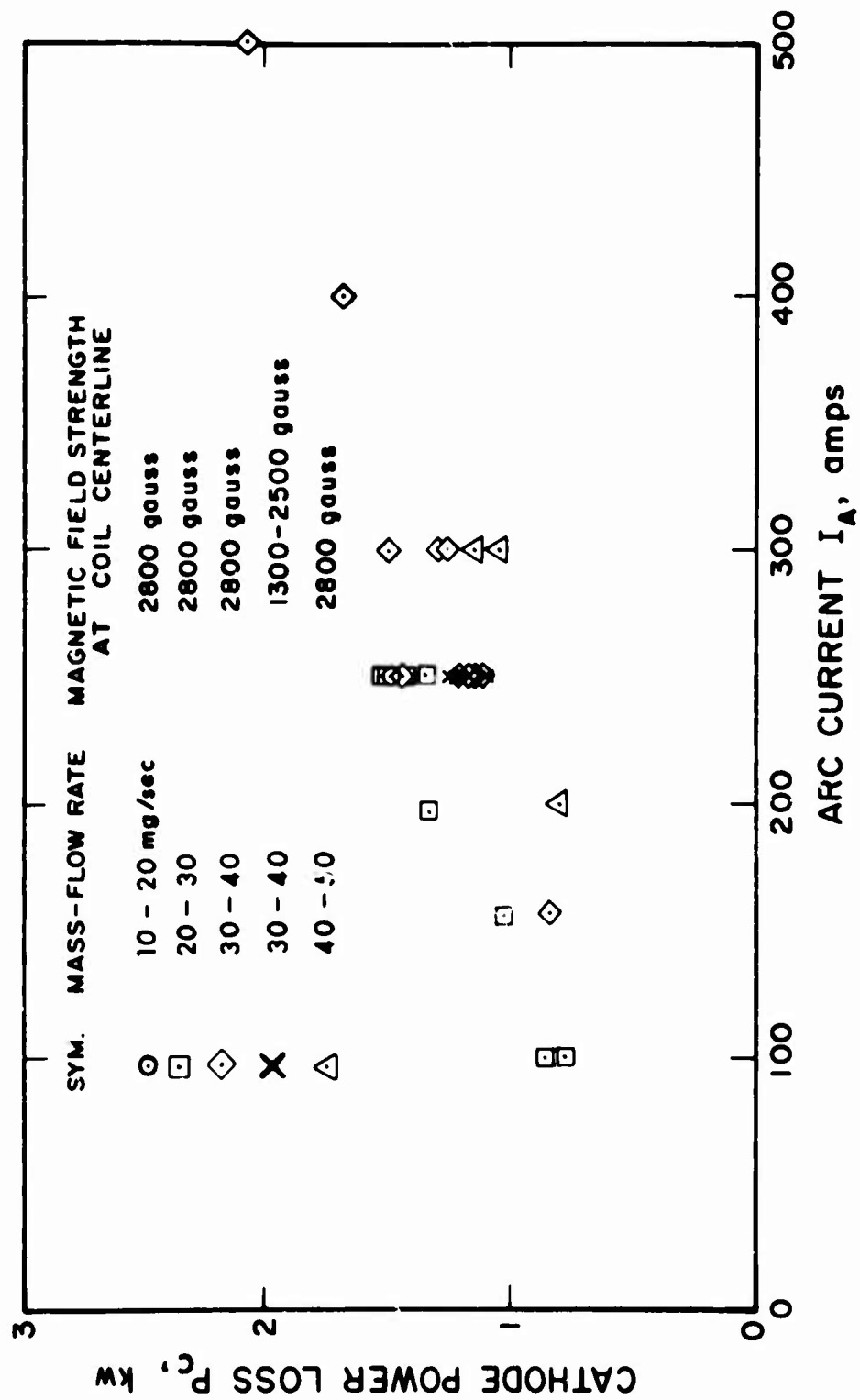


Figure 20 Cathode Power Loss as a Function of Arc Current



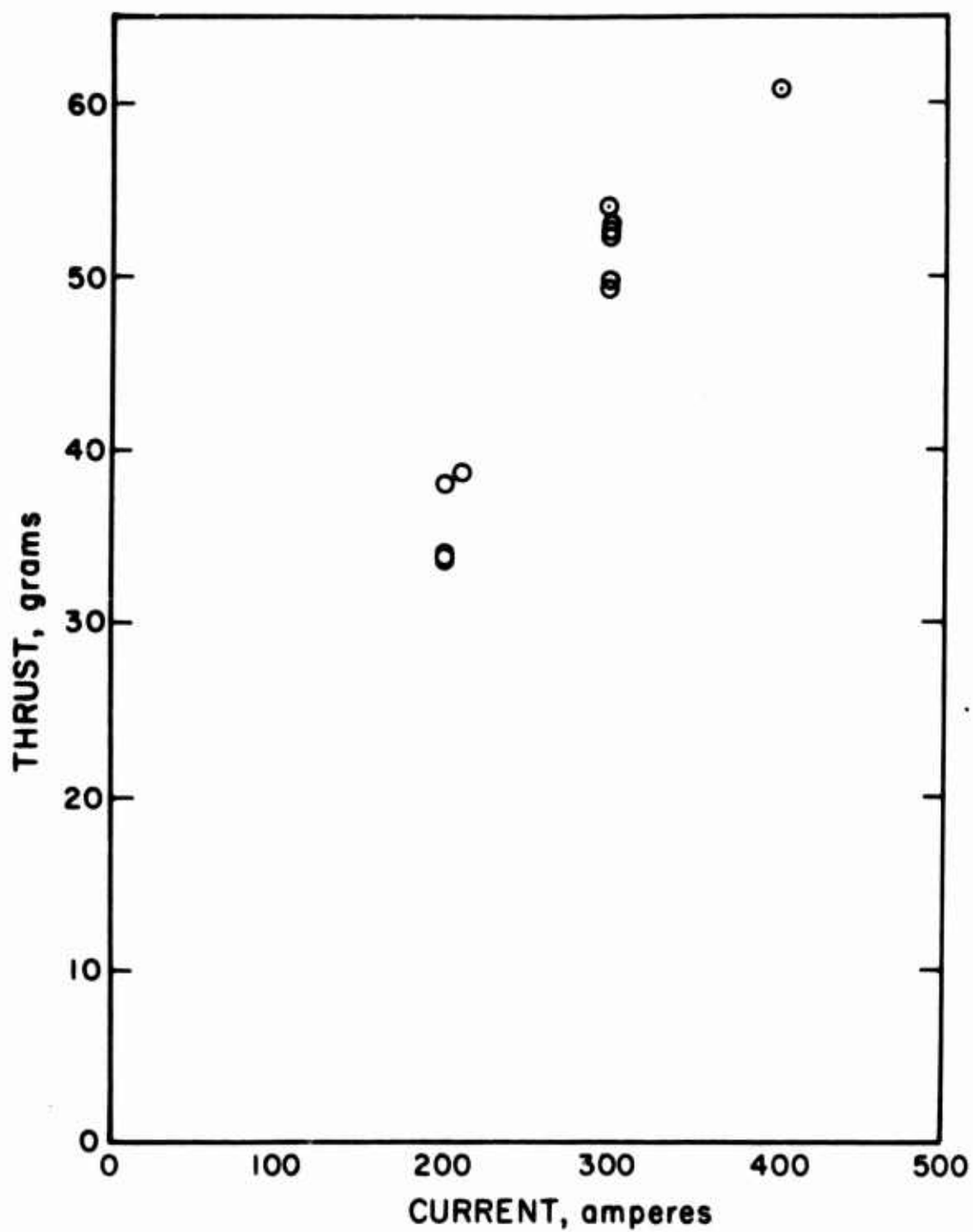


Figure 21 Thrust versus Current with Potassium

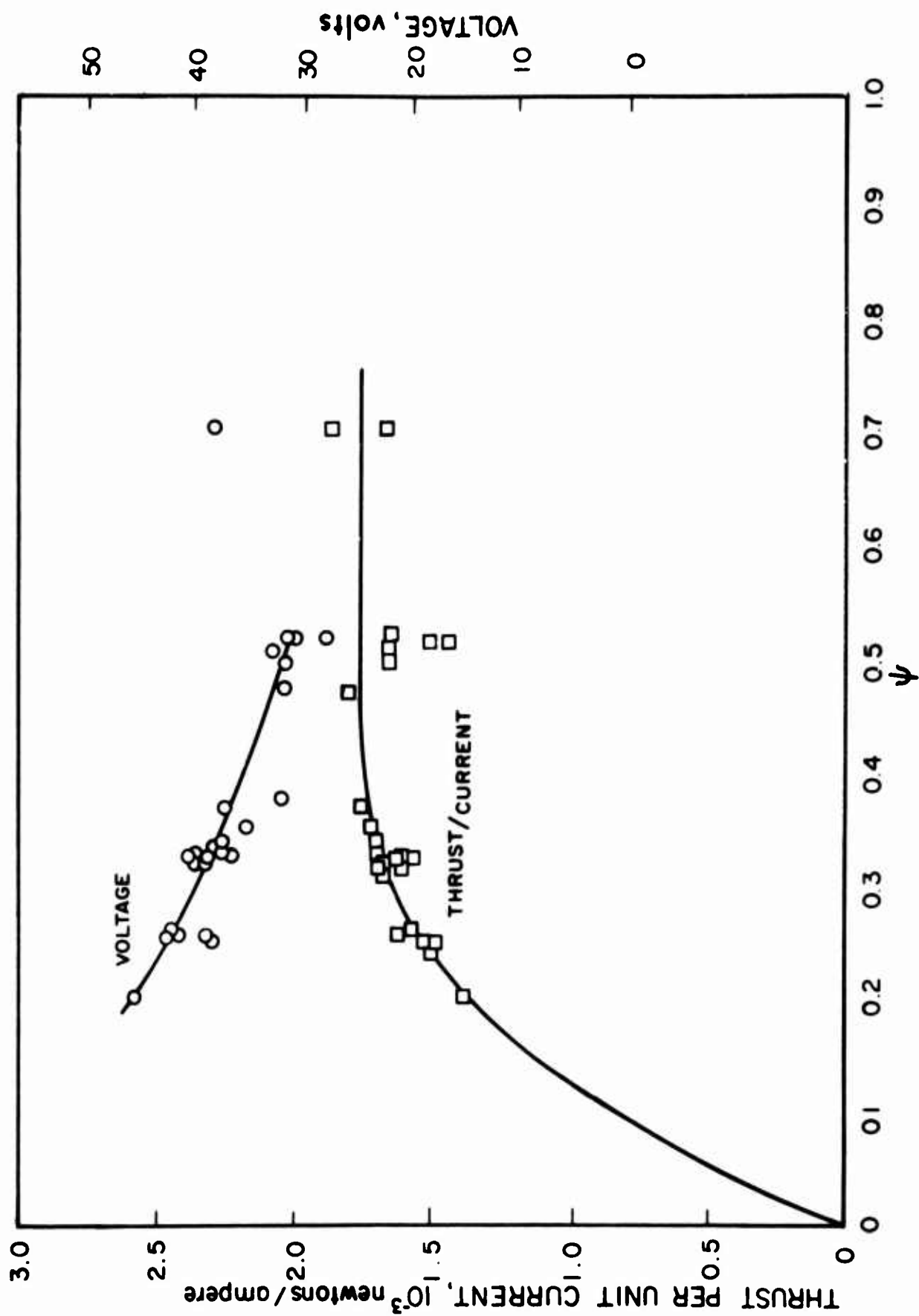


Figure 22 Thrust per Unit Current, Voltage as a Function of Parameter  $\psi = \frac{e h m}{m_a I}$ , for Potassium

(upstream) surface of the fin. Radiation from the front surface of the fin, from the outside cylindrical surface of the anode, and most of the radiation from the front surface of the anode itself is absorbed by the magnet coil housing. The sum of the powers transferred to these oil-cooled components is approximately equal to the anode power loss. Power transfer was determined by measuring the cooling-oil flow rate and temperature rise.

The potassium was fed into the thruster with the bellows feed system developed for lithium. A recent calibration of the feed system accomplished during the reporting period is presented in Section IV.

## SECTION VII

### CONFIGURATION STUDIES

#### 1. BUFFERED CATHODE THRUSTOR STUDIES

The objective of the buffered-cathode configuration shown in Figure 23 was to operate the cathode in a spot-attachment mode. Experience with gases has indicated that the attachment mode is determined primarily by the pressure level, although the geometry and flow pattern around the cathode are also important parameters. In the cathode study reported in Ref. 8 the stable spot-attachment mode prevailed at pressure levels above about 1 psia. In this mode the apparent cathode voltage drop (defined as power loss divided by arc current) was only about one volt and the cathode erosion rate was negligible. At pressure levels below about 1 psia, the attachment region became more diffuse, was unstable, the apparent voltage drop increased to several volts, and the erosion became severe. In the previous alkali-metal arc jets (Refs. 1 and 9) the pressure at the cathode was very low (not measured but estimated to be about 10 torr). The attachment mode was diffuse and in some cases unstable. The apparent cathode voltage drop was about 6 to 7 volts and the erosion rate was greater than desired. This limited the maximum current capacity of the engine to a level lower than desired. The intent in designing the buffered-cathode was to increase the pressure level at the cathode so that the power loss and erosion would decrease. The unstable behavior at low pressure may be due to oscillation between an electron-emission mode and an ion-bombardment mode of current conduction across the cathode surface as discussed in more detail in Section III.3.a. The lower heat loss in the conical cathode with attachment at the tip can be explained by considering the heat conduction through the cathode as calculated in Appendix III.

The first apparent published account of the operation of a cathode with a buffer for stabilization of the cathode attachment in

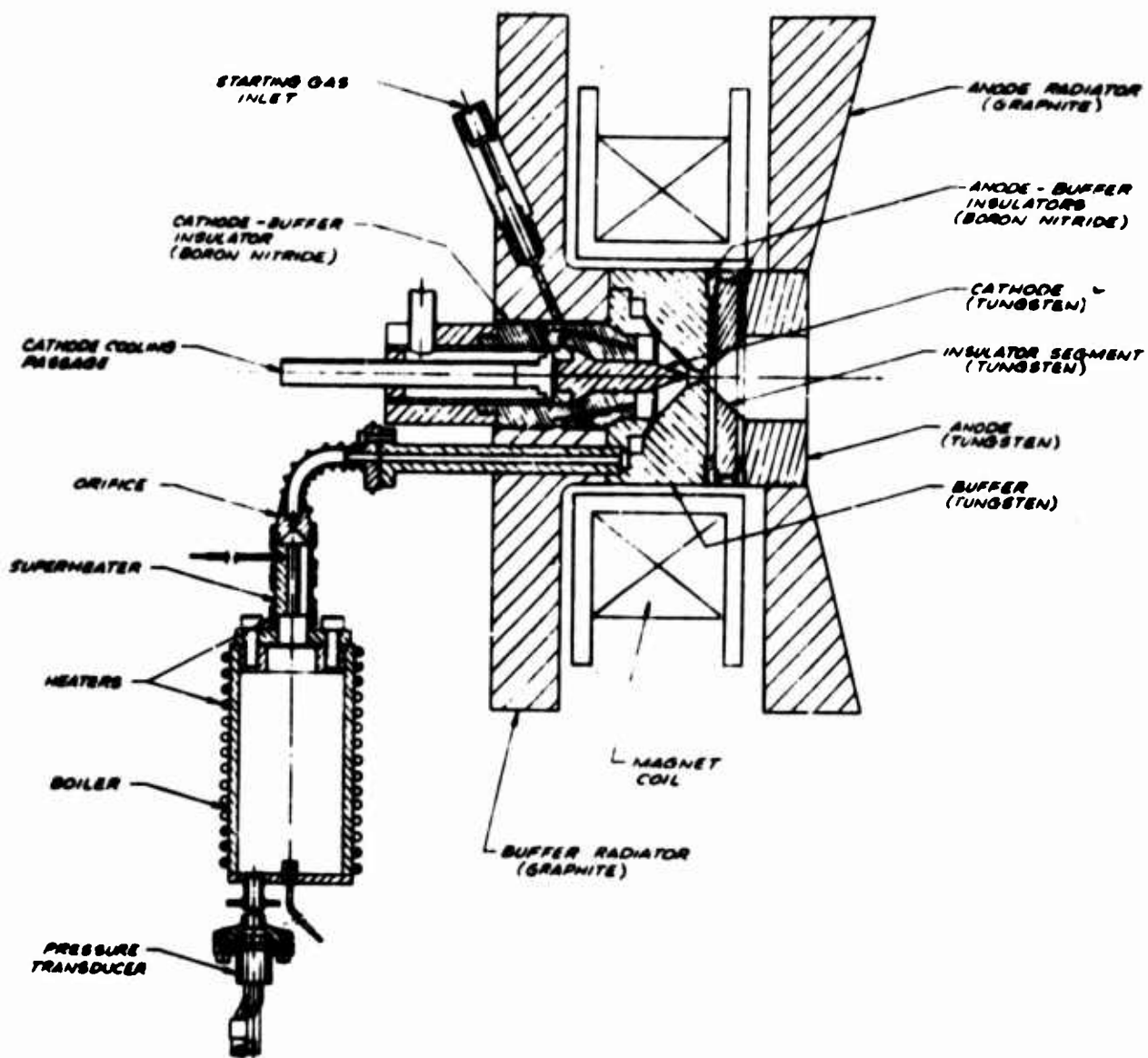


Figure 23 Buffered-Cathode Thrustor Configuration, Model LAJ-BF-1

gas appears to have been given in Ref. 10. This was embodied in hydrogen arc jet configurations (Refs. 11 and 12) which were forerunners of the present alkali-metal investigations. Additionally, in the first phase of the present program (Ref. 1) a buffered cathode with hydrogen gas stabilization was used with a lithium-fed anode. The latter experiments were inconclusive because an insulator between the buffer and anode failed before test conditions were achieved with sufficiently low hydrogen flow rate to achieve a specific impulse high enough to be of interest. The work reported here included investigation of operation of a buffer with sodium and lithium injected into the buffer and additional studies of the hydrogen-stabilized buffer with lithium injected at the anode.

Three classes of buffered-cathode configurations were tested. These were designated Models LAJ-BF-( ) for buffer-feed, LAJ-AF-BG-( ) for anode-feed with gas flow through the buffer and LAJ-AF-CG-( ) for anode-feed with gas-stabilized cathode. These designs are illustrated in Figures 24 through 26. The difference between the buffer designation (BF and BG models) and the gas-stabilized cathode designation is subtle and somewhat arbitrary. The buffer designation was used where the cathode tip was definitely located upstream of the throat whereas in the so-called gas-stabilized cathode design the cathode tip either protruded downstream of the throat or was located in the throat.

a. Thrustors With Alkali-Metal Fed Through the Buffer

The original basic BF thruster design is shown in Figure 23. The propellant vapor was injected through the annular slot of the buffer upstream of the cathode tip and the buffer throat, which is 0.10 inch in diameter. With a propellant flow rate of 1 to 2 mg/sec it was estimated that the pressure at the cathode tip was of the order of 0.1 atmosphere. This pressure was sufficiently high for the arc to attach in a small spot at the tip of the conical cathode.

This thruster was radiation-cooled with the exception of the water-cooled cathode. Graphite disks attached to the buffer and the anode enhanced the radiation-cooling capacity. Much of the radiation









was absorbed by the water-cooled magnet-coil housing. In addition there was a water-cooled shield (not shown in Figure 23) behind the buffer radiator. The total power lost to the buffer was determined by measuring the heat transferred to the shield and the inner and rear portions of the magnet-coil housing. The qualitative results of tests are summarized in Table II and the detailed account is presented in the following sections.

The first test of this thruster was inconclusive because of cracking of the tungsten buffer and subsequent leakage of the propellant out of the buffer. However, it was apparent that there was not significant erosion of the cathode or the buffer. To this extent the objective of stabilizing the cathode attachment spot and reducing cathode erosion was met by this configuration.

This design was not expected to be an efficient thruster because all of the propellant is injected into the buffer in the region of the cathode. The main purpose was to determine whether or not a stable point attachment could be maintained with an alkali metal propellant (as was the case with gaseous propellants). For significant Hall-current acceleration most of the propellant should be injected through the anode.

A new buffer was built to replace the one which broke during the first test. The design was modified (LAJ-BF-1B) to reduce thermal stresses in the buffer by incorporating a tungsten insert in a molybdenum sleeve as shown in Figure 24.

Sufficient experimental results were obtained with Model LAJ-AF-1B to establish the superiority of the buffered cathode configuration over the diffusely-operating cathode of the earlier thruster configurations (Ref. 1). The buffered cathode has the following advantages:

1. The arc attaches in a small spot at the tip of the conical cathode.

TABLE II BUFFERED-CATHODE CONFIGURATION

Summary of Test Results

Engine Configuration		Propellant	Qualitative Results
BF-1		K	External arcs - Buffer cracked - No cathode or insulator erosion
BF-1A	Mo buffer with W insert to eliminate cracking tendency.	K	External arcs - Propellant leak between insulator and buffer No cathode or insulator erosion
BF-1B	Extended buffer body rearward to provide threaded seal between buffer and insulator.	K	No cathode or insulator erosion No propellant leakage - Propellant not diffusing to anode sheath.
BF-1C	Incorporated bypass holes through buffer to distribute propellant to anode sheath.	K	No erosion. No propellant leakage. Arc sometimes attached in buffer bypass holes. Inadequate distribution of propellant in anode sheath.
BF-1D	Incorporated annular bypass channel between buffer and buffer-anode insulator. Decreased anode diameter from 3 to 2 cm.	K	Erosion of buffer-anode insulator. Very stable operation - apparently good propellant distribution in anode sheath. Measured $I_{sp}$ of about 1000 sec and efficiency of 20%.
BF-1E	Installed "sandwich" buffer-anode insulator and shortened anode from 2 to 1 cm. Mounted liquid lithium feed system with vaporizer.	Li	Achieved stable operation without erosion until lithium flooded engine and shorted cathode to buffer. Then arc attached to buffer and eroded "sandwich" insulator. No erosion of electrodes or cathode-buffer insulator.



2. As a result of (1) the erosion of the cathode material is negligible and the cathode power loss has been reduced.
3. The cathode insulator is well-protected in this configuration and no erosion has occurred.

The buffered-cathode tests showed that most of the propellant should be injected in the region of the anode for efficient thruster operation. It was clear from observation of the distribution of potassium condensed on the tank wall that ionization occurred in the cathode jet and most of the propellant flowed out along magnetic field lines. The low thrust under this condition is consistent with the observed difference in performance between cathode-fed and anode-fed engines reported during this program in Ref. 1.

This behavior is also consistent with the analytical model (Refs. 1 and 6) based on: (1) azimuthal acceleration of the ions as the current radially crosses the magnetic field followed by (2) conversion of azimuthally-directed kinetic energy into axially-directed kinetic energy as the plasma expands through the "magnetic-nozzle".

The next step was to modify the buffer-fed engine to provide for flow of potassium out of the cathode jet closer to the anode internal surface. The attempt was to provide eight by-pass holes through the buffer and buffer-anode insulator assembly as shown in Figure 24 as Model LAJ-BF-1C. As the sketch shows, all of the potassium is injected into the cathode chamber. It was estimated that 2/3 of the flow passes through the peripheral holes and 1/3 through the buffer throat. Some experimental difficulties and problems encountered with this thruster design are discussed below since the experience is pertinent to the technology of arc-jets which use alkali metals for propellants.

The first problem that developed was leakage of the propellant vapor out of the cathode chamber through the joint between the buffer and the cathode insulator. This caused deterioration of the graphite buffer-radiator and frequent external arcs between the buffer and anode. The original seal design was based on pressure between the graphite



radiator and the buffer maintained by a Belleville spring washer backing up the assembly bolts. The leakage was stopped by modifying the design to extend the rear portion of the buffer so that the buffer and cathode insulator were joined by a long (~ 2") threaded joint. The radiator was in turn joined to the outside of the buffer with another threaded joint. Threaded joints between boron nitride and tungsten or molybdenum generally form effective seals, apparently because of diffusion bonding of the two materials at high temperature.

Another problem was arcing between external components of the engine, feed system, power leads and test chamber even after the leakage was stopped. This was particularly acute at low test chamber pressures (i.e., between  $10^{-2}$  and  $10^{-5}$  torr) and hampered the task of performance measurement. This problem was solved by improving the insulation of the power leads.

With respect to accomplishing the desired objective of having the propellant flow un-ionized into the anode jet where it would be ionized and then azimuthally and axially accelerated, the BF-1C design was not totally satisfactory. First, the propellant flowing out of the peripheral holes appeared to be ionized as a result of part of the current flowing along the jets from the holes and into or through the buffer. Secondly, these jets of vapor did not coalesce close to the anode; thus, the azimuthal current loops did not form and the Hall-current acceleration was less effective. It appeared necessary to inject the propellant separately through an annular orifice in the anode; however, this would have complicated the test because of the requirement for two feed systems.

The thruster was then modified to the BF-1D configuration as shown in Figure 24, to improve the flow distribution of propellant. At the same time the anode diameter was decreased from 3 cm to 2 cm. These modifications improved the stability of the thruster and extended its maximum current capacity as demonstrated in a successful test over a period of about one hour at power levels between 5 and 15 kilowatts.

The current level was as high as 350 amperes for several minutes without appreciable erosion of the cathode, cathode-buffer insulator, buffer, or anode. The buffer-anode insulator, which had a large surface area exposed, suffered some erosion, part of which may have occurred near the end of the run when the propellant feed system was empty.

The maximum  $I_{sp}$  achieved during this test, which was made with potassium propellant, was about 1000 seconds where the efficiency was about 20 percent. The magnetic field strength was varied from about 2000 to 3000 gauss without an appreciable effect on the thrust level. The test chamber pressure was maintained at about  $10^{-4}$  torr. The effect of chamber pressure on thrust appeared negligible in the range of  $2 \times 10^{-3}$  to  $10^{-4}$  torr.

The next modification, shown in Figure 24 as Model BF-1E, consisted of replacing the buffer-to-anode one-piece boron nitride insulator with a segmented or "sandwich" type insulator consisting of thin disks of tungsten and boron nitride. The tungsten disks reduce the vulnerability of the insulator to the alkali-plasma environment by a shielding effect and by higher heat conduction from the inner wall to the outside radiating surface. This modification was expected to eliminate the insulator erosion problem present with the BF-1D design and provide for longer, more stable, repeatable operation.

Tests of the buffered engine prior to BF-1E were all made with potassium propellant using a boiler feed system to minimize the likelihood of liquid flow or condensation in the buffer chamber. Liquid in this chamber would probably cause a short-circuit between the cathode and buffer. Lithium was used with the BF-1E configuration. It was injected by the bellows-type feed system through a separately heated vaporizer connected to the buffer.

In tests of this thruster a strong coupling was found to exist between the gas flow<sup>2</sup> rate and the lithium feed rate because of

---

<sup>2</sup>Used during starting and preheating prior to feeding lithium

the pressure developed in the buffer cavity. Initially this led to flooding of the engine as the gas flow rate was reduced. In order to minimize the interaction between the feed systems, a vaporizer with a sonic orifice was introduced into the lithium feed line between the feeder and the engine. The combination of high vaporizer temperature and high back pressure from the engine proved to be a deadly combination for the vaporizer seals. Many seals were tried but in all cases the vapor leaked out of the vaporizer.

For this reason, no performance data with lithium were obtained for this engine configuration and it was decided that this engine configuration should temporarily be shelved. The basic ideas were, however, used in configurations for which the technology has been proven. These thrusters are described in the next sections.

b. Thrusters With Gas-Flow Through the Buffer

Based on the experience with potassium and lithium flow through the BF configurations, the BG configuration shown in Figure 25 was designed. This engine has the following characteristics:

1. Nitrogen gas flows through a conical cathode-buffer combination. Since nitrogen reacts with lithium on the walls, it was expected that the nitrogen would be chemically pumped and hence that the tank pressure could be maintained in the region of  $10^{-4}$  torr. The chemical pumping of air had been observed in previous tests with lithium.
2. The insulator consisted of layers of boron nitride and tungsten. This structure helps to eliminate the problem of electrode shorting when either propellant flooding occurs or when the insulator is slightly damaged, e.g., cracked.
3. A conventional "anode-feed" anode was used. However, to minimize the probability of flooding, the lithium propellant was vaporized in a porous plug just outside of the anode and was injected into the arc discharge at the inner surface of the anode.

This engine was tested over the ranges of parameters presented below:

Arc Current	160 to 450 amperes
Applied Magnetic Field Strength	1700 to 3500 gauss (at coil center)
Mass-Flow-Rate	
Lithium	7 to 15.5 mg/sec
Nitrogen	1.1 to 2.9 mg/sec

The tank pressure was not varied as an independent parameter, but varied slightly with operating conditions between  $8 \times 10^{-5}$  and  $5 \times 10^{-4}$  torr. This is believed to be below the regime where pressure affects the thrust.

The tank pressure level with nitrogen flow was about the same as in previous tests without nitrogen. This indicates that, as expected, the nitrogen was "chemically-pumped" by the lithium condensing on the tank walls.

The measured thrust level increased with arc current and coil current (i.e., magnetic field strength) but seemed to be relatively independent of the total mass-flow-rate over the range of 0.008 to 0.022 grams per second. The resulting specific impulse and thrust efficiency varied from about 3000 sec and 30 percent to 800 sec and 8 percent.

There appeared to be two conditions which limited the specific impulse, although this limit was not thoroughly "mapped-out" for large ranges of the independent variables.

One limiting situation appeared when the current was increased while holding the other independent test variable constant. At a "critical" value of the current an unstable or "modal" operation of the thruster was encountered. In the first or "normal" mode the thrust was higher, voltage was lower, and tank pressure was lower than in the "abnormal" mode. The jet was red (characteristic lithium radiation) in the normal mode and turned to blue-purple in the abnormal mode. The time in each mode varied between a few seconds to several minutes.

This behavior was attributed to an unstable flow of the lithium propellant resulting from movement of the vapor front in the porous vaporizer. The low-voltage normal mode occurs with excessive (i.e., greater than average) mass-flow-rate and the high-voltage abnormal mode with inadequate mass-flow-rate. During one period of the test, after the thruster had been oscillating between these two modes for about one-half hour, the mass-flow-rate was increased by 50 percent; and, though two modes still existed, the thrust and voltage were very close together (i.e., within 5 to 10 percent).

The second type of limit on specific impulse was imposed by a current limit above which there was melting and erosion of the cathode, buffer, and buffer-to-anode insulators. This current limit is definitely below the maximum current for the test of 450 amperes; however, the threshold of erosion was not precisely determined because of poor visibility<sup>3</sup> through the tank windows. At the end of the test the cathode tip had melted, the buffer had eroded to an internal diameter several times greater than its original diameter, and the segmented insulator assembly had eroded to the point where its inner diameter was about equal to the inner diameter of the anode (refer to Figure 25). The erosion current-limit is undoubtedly lower at lower mass-flow-rates and the observed erosion was probably aggravated by the unstable model operation described above.

The lithium vaporizer for this model, consisting of a porous tungsten insert in the feed tube near the anode, was a compromise for reliable operation of both the bellows feed system and vaporizer. The vaporizer is brazed into the anode and the joint between the vaporizer and tube from the feed system is far enough away from the anode that the temperature is moderate and sealing of this joint is effective with a metal O-ring. Also three small (0.063-in. diameter) holes were included in the porous tungsten insert to decrease the back

---

<sup>3</sup> Tank windows become opaque from the lithium coating.



pressure acting on the bellows feed system. This lowered the volume displacement effects in the bellows and generally improved the accuracy and stability of the feed system.

Results of the tests described above are presented in Figures 27 through 30. The overall efficiency (not including coil power and feed system power) is plotted as a function of specific impulse in Figure 27. The plot includes all of the data which appeared to be reliable and repeatable for a wide range of arc current, magnetic field strength, and mass-flow-rate. In the  $I_{sp}$  range of interest, this thruster is less efficient than previous configurations (Ref. 1). This appears to be due to lower thermal efficiency with the present configuration as a result of higher power loss to the anode and the additional loss to the buffer (not present in the earlier thrusters).

Figure 28 shows thermal efficiency as a function of specific impulse for various values of arc current and mass-flow-rate. The effect of the magnetic field strength on thermal efficiency is not clear and only those points at the maximum coil current of 800 amperes are plotted. Figure 28 indicates that the thermal efficiency increases with  $I_{sp}$  when the mass-flow-rate is held constant. (Actually  $\eta_{thermal}$  increased with increasing current.) As Figure 28 also shows,  $\eta_{thermal}$  increases with mass-flow-rate if the  $I_{sp}$  is held constant. Obviously,  $I_{sp}$  is not the proper correlating parameter for thermal efficiency in this case.

Figure 29 implies that the thrust to arc-current ratio,  $\frac{T}{I_A}$ , correlates with the parameter

$$\psi = \frac{e}{I_A} \left( \frac{\dot{m}_{Li}}{m_{Li}} + \frac{\dot{m}_N}{m_N} \right)$$

as expected from the analytical results (Refs. 1 and 6). This is reasonable, at least for constant magnetic field strength; however,



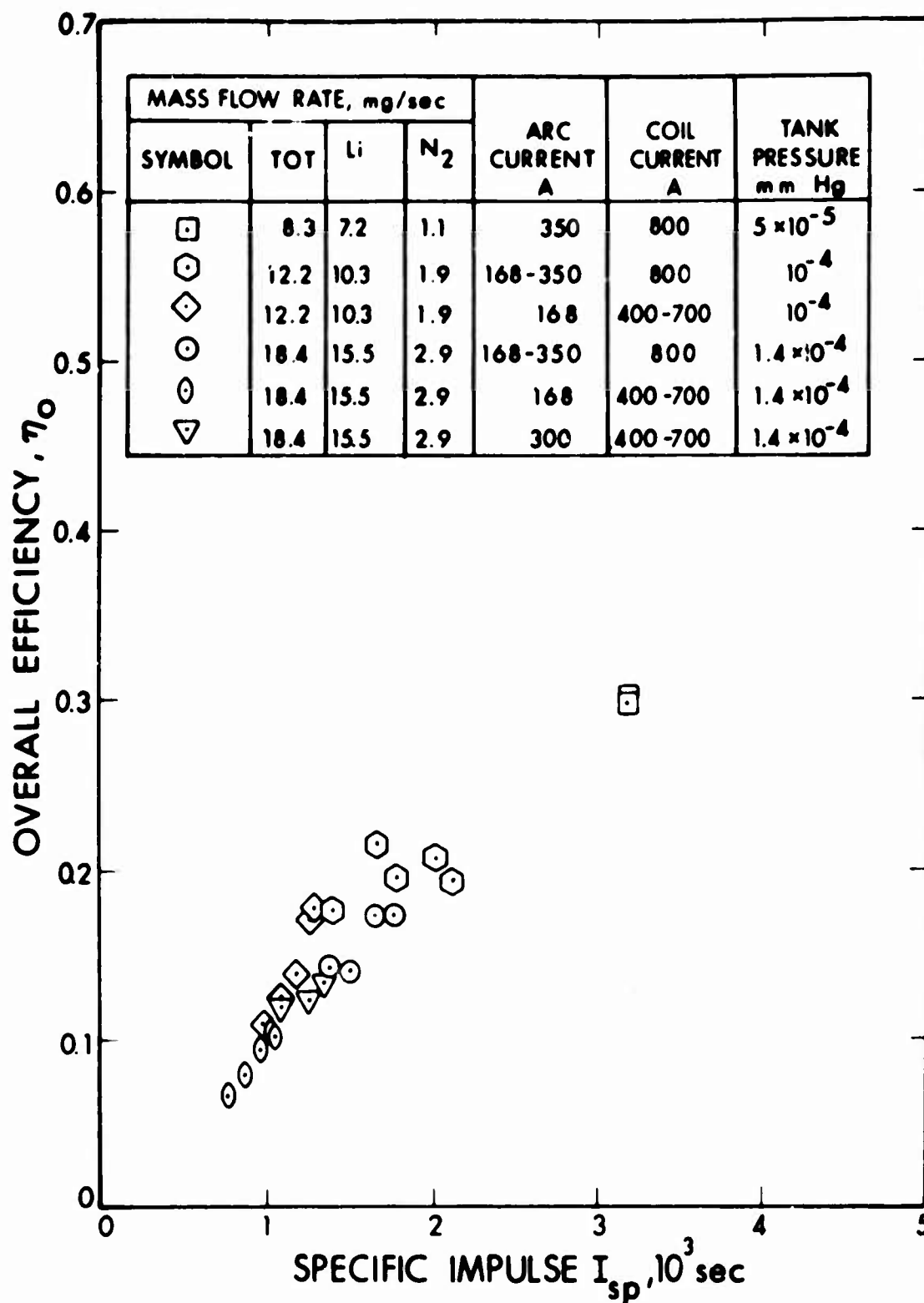


Figure 27 Overall Efficiency  $\frac{T^2}{2mVI}$  of Lithium Arc Jet Model LAJ-AF-BF-1A as a Function of Specific Impulse

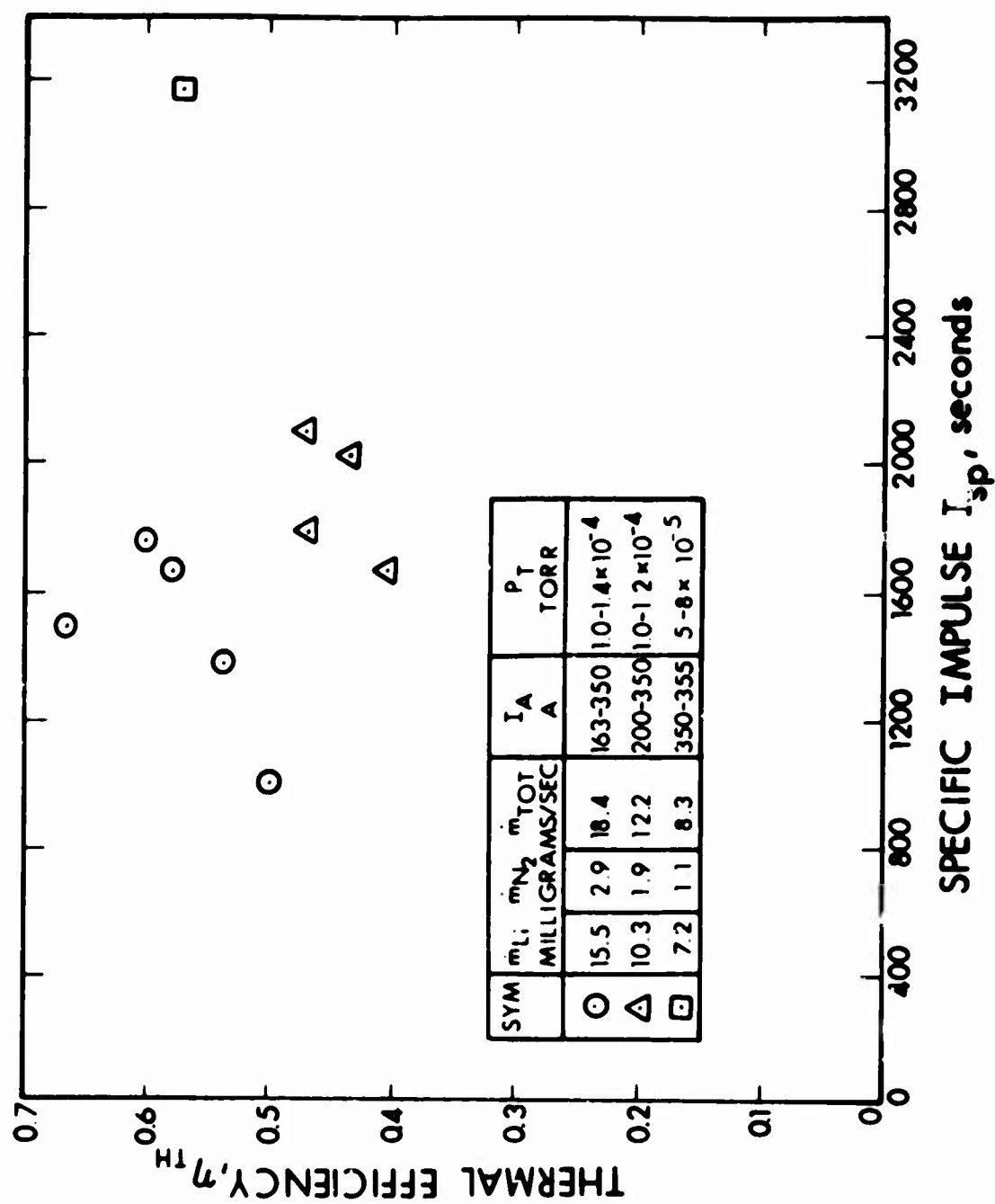


Figure 28 Thermal Efficiency of Lithium Arc Jet Model LAJ-AF-BG-1A as a Function of Specific Impulse

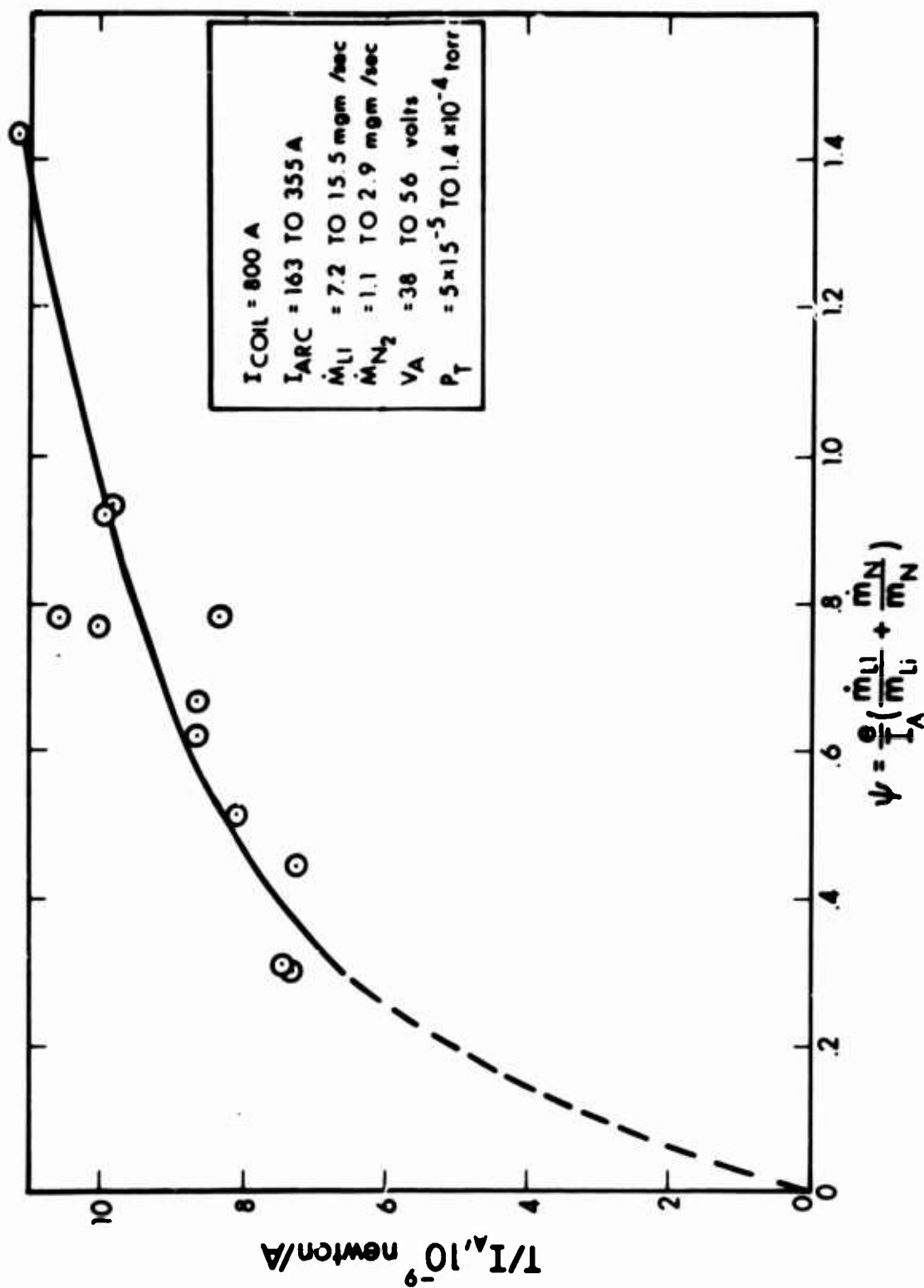


Figure 29 Ratio of Thrust to Arc Current for Lithium Arc Jet Model LAJ-AF-BG-1A as a Function of the Mass-Flow, Current Parameter  $\psi$

as Figure 30 shows,  $T/I_A$  increases with increasing magnetic field strength at constant arc current and mass-flow-rate (hence, also at constant  $\psi$ ). The proper parameter, on theoretical grounds, including  $\psi$ , magnetic field strength, and anode size is yet to be clearly established but is extremely important for optimizing thruster design and scaling to higher or lower power levels.

c. Thrusters With Gas-Stabilized Cathode

The gas-stabilized cathode configurations, shown in Figures 23 and 31 were developed to maintain the advantages of the previous buffered-cathode design and reduce the wall losses and neutral propellant losses. As in the buffer models, nitrogen and/or hydrogen were injected around the cathode to maintain spot attachment of the arc at the cathode tip. In the buffered design it appeared that the arc was attached to the anode upstream of the gap where lithium is injected. This situation probably permitted a significant fraction of the propellant to flow out of the thruster without encountering the arc discharge and thus without being ionized and electromagnetically accelerated. This loss was probably reduced considerably in the modified design (Figure 31) since the cathode was farther downstream, and the insulator was immediately adjacent to the injection gap. Both of these changes should cause the arc to attach to the anode downstream of the region of lithium injection.

Performance capabilities and parametric effects were experimentally determined for the first versions of the gas-stabilized-cathode thruster (Models CG-1A and 1B) with two different magnet-coil arrangements producing different magnetic field shapes and strength levels. Other parameters varied in the tests were arc current (up to 400 amperes), test chamber pressure ( $10^{-2}$  to  $5 \times 10^{-5}$  torr) and mass-flow-rate of both lithium (10 to 20 mg/sec) and nitrogen injected at the cathode tip (0 to 10 mg/sec).

The thrust and efficiency characteristics of this configuration are somewhat better than the fully buffered configuration

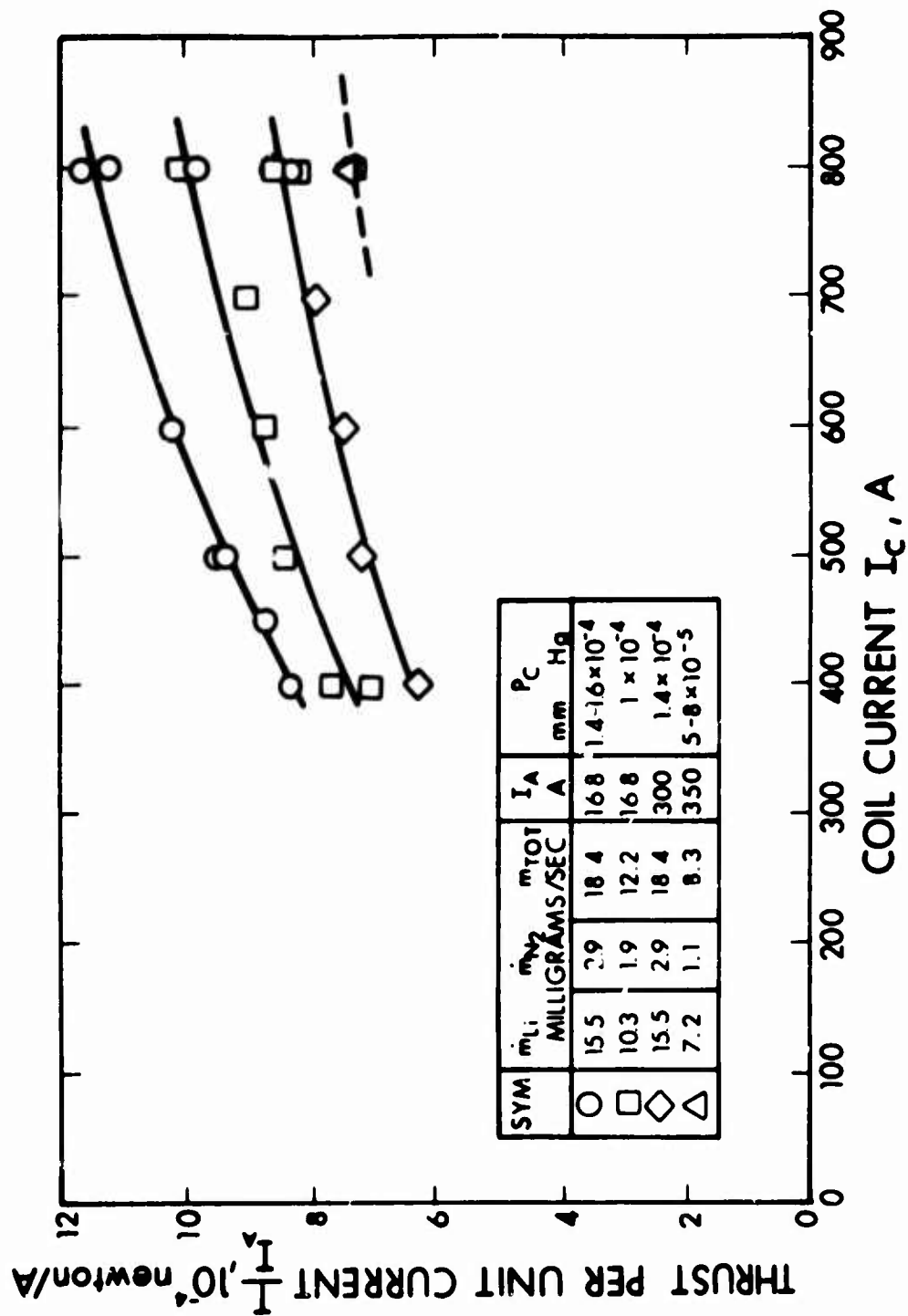
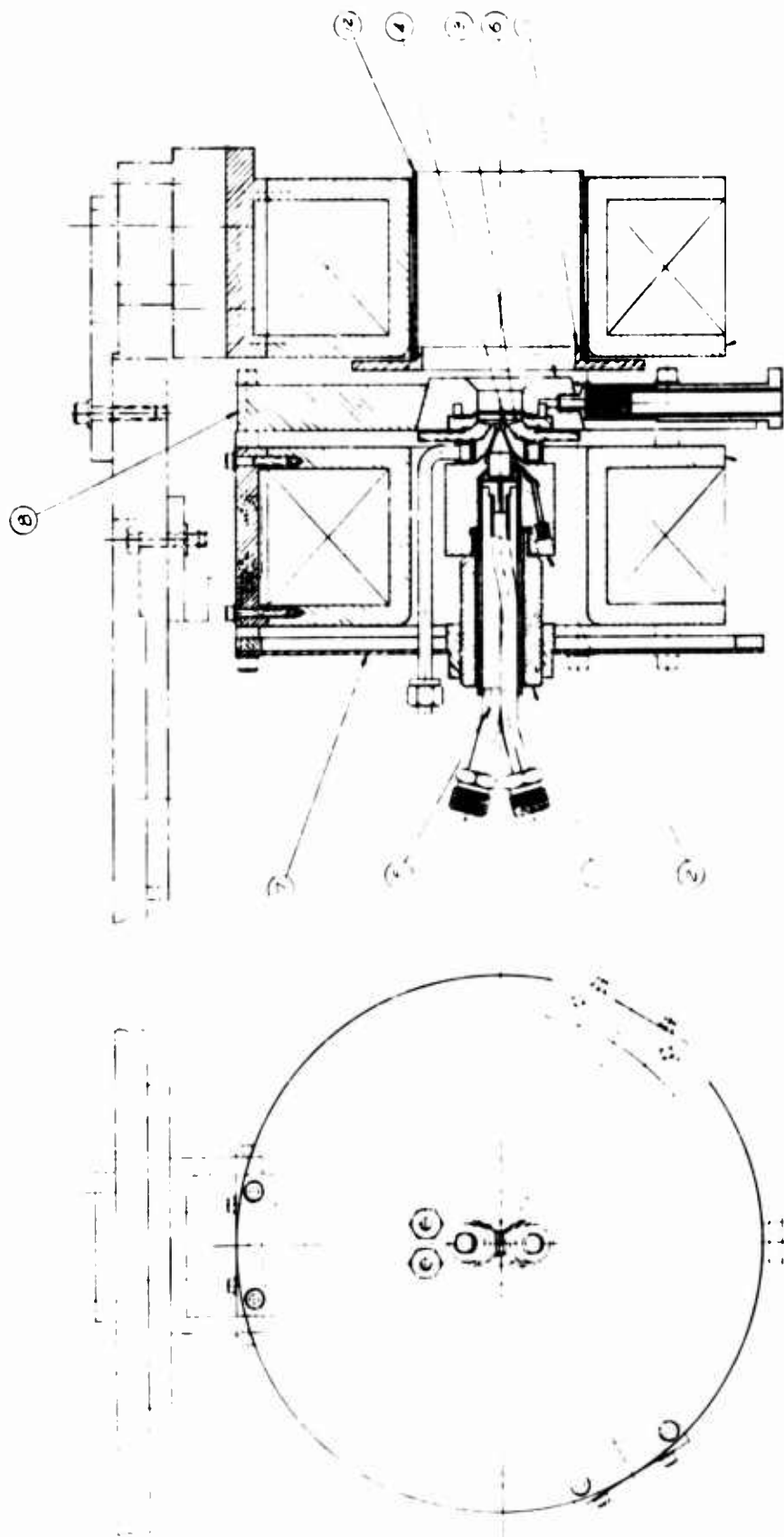


Figure 30 Ratio of Thrust Arc Current for Lithium Arc Jet Model LAJ-AF-BG-1A as a Function of the Magnet-Coil Current (Magnetic Field Strength at Center of Coil is  $\sim 4.4$  gauss per 1000 amperes)



(3)

(3)

Figure 31 Lithium Arc Jet Assembly

710-521	
1	2 710-521 NO. 1 - 1/2"
1	2 710-521 NO. 2 - 1/2"
1	2 710-521 NO. 3 - 1/2"
1	2 710-521 NO. 4 - 1/2"
1	2 710-521 NO. 5 - 1/2"
1	2 710-521 NO. 6 - 1/2"
1	2 710-521 NO. 7 - 1/2"
1	2 710-521 NO. 8 - 1/2"
1	2 710-521 NO. 9 - 1/2"
1	2 710-521 NO. 10 - 1/2"
1	2 710-521 NO. 11 - 1/2"
1	2 710-521 NO. 12 - 1/2"
1	2 710-521 NO. 13 - 1/2"
1	2 710-521 NO. 14 - 1/2"
1	2 710-521 NO. 15 - 1/2"
1	2 710-521 NO. 16 - 1/2"
1	2 710-521 NO. 17 - 1/2"
1	2 710-521 NO. 18 - 1/2"
1	2 710-521 NO. 19 - 1/2"
1	2 710-521 NO. 20 - 1/2"
1	2 710-521 NO. 21 - 1/2"
1	2 710-521 NO. 22 - 1/2"
1	2 710-521 NO. 23 - 1/2"
1	2 710-521 NO. 24 - 1/2"
1	2 710-521 NO. 25 - 1/2"
1	2 710-521 NO. 26 - 1/2"
1	2 710-521 NO. 27 - 1/2"
1	2 710-521 NO. 28 - 1/2"
1	2 710-521 NO. 29 - 1/2"
1	2 710-521 NO. 30 - 1/2"
1	2 710-521 NO. 31 - 1/2"
1	2 710-521 NO. 32 - 1/2"
1	2 710-521 NO. 33 - 1/2"
1	2 710-521 NO. 34 - 1/2"
1	2 710-521 NO. 35 - 1/2"
1	2 710-521 NO. 36 - 1/2"
1	2 710-521 NO. 37 - 1/2"
1	2 710-521 NO. 38 - 1/2"
1	2 710-521 NO. 39 - 1/2"
1	2 710-521 NO. 40 - 1/2"
1	2 710-521 NO. 41 - 1/2"
1	2 710-521 NO. 42 - 1/2"
1	2 710-521 NO. 43 - 1/2"
1	2 710-521 NO. 44 - 1/2"
1	2 710-521 NO. 45 - 1/2"
1	2 710-521 NO. 46 - 1/2"
1	2 710-521 NO. 47 - 1/2"
1	2 710-521 NO. 48 - 1/2"
1	2 710-521 NO. 49 - 1/2"
1	2 710-521 NO. 50 - 1/2"
1	2 710-521 NO. 51 - 1/2"
1	2 710-521 NO. 52 - 1/2"
1	2 710-521 NO. 53 - 1/2"
1	2 710-521 NO. 54 - 1/2"
1	2 710-521 NO. 55 - 1/2"
1	2 710-521 NO. 56 - 1/2"
1	2 710-521 NO. 57 - 1/2"
1	2 710-521 NO. 58 - 1/2"
1	2 710-521 NO. 59 - 1/2"
1	2 710-521 NO. 60 - 1/2"
1	2 710-521 NO. 61 - 1/2"
1	2 710-521 NO. 62 - 1/2"
1	2 710-521 NO. 63 - 1/2"
1	2 710-521 NO. 64 - 1/2"
1	2 710-521 NO. 65 - 1/2"
1	2 710-521 NO. 66 - 1/2"
1	2 710-521 NO. 67 - 1/2"
1	2 710-521 NO. 68 - 1/2"
1	2 710-521 NO. 69 - 1/2"
1	2 710-521 NO. 70 - 1/2"
1	2 710-521 NO. 71 - 1/2"
1	2 710-521 NO. 72 - 1/2"
1	2 710-521 NO. 73 - 1/2"
1	2 710-521 NO. 74 - 1/2"
1	2 710-521 NO. 75 - 1/2"
1	2 710-521 NO. 76 - 1/2"
1	2 710-521 NO. 77 - 1/2"
1	2 710-521 NO. 78 - 1/2"
1	2 710-521 NO. 79 - 1/2"
1	2 710-521 NO. 80 - 1/2"
1	2 710-521 NO. 81 - 1/2"
1	2 710-521 NO. 82 - 1/2"
1	2 710-521 NO. 83 - 1/2"
1	2 710-521 NO. 84 - 1/2"
1	2 710-521 NO. 85 - 1/2"
1	2 710-521 NO. 86 - 1/2"
1	2 710-521 NO. 87 - 1/2"
1	2 710-521 NO. 88 - 1/2"
1	2 710-521 NO. 89 - 1/2"
1	2 710-521 NO. 90 - 1/2"
1	2 710-521 NO. 91 - 1/2"
1	2 710-521 NO. 92 - 1/2"
1	2 710-521 NO. 93 - 1/2"
1	2 710-521 NO. 94 - 1/2"
1	2 710-521 NO. 95 - 1/2"
1	2 710-521 NO. 96 - 1/2"
1	2 710-521 NO. 97 - 1/2"
1	2 710-521 NO. 98 - 1/2"
1	2 710-521 NO. 99 - 1/2"
1	2 710-521 NO. 100 - 1/2"



described previously — especially when operating with the arc attached in a small region near the cathode tip. Another mode of attachment was occasionally observed as rotation of the attachment region around the conical surface of the cathode. In the results to be presented below, the first test (with Model LAJ-AF-CG-1A) was made with attachment in the "spot" or "tip" mode. In the second test (with Model LAJ-AF-CG-1B) the arc attached in the "surface" mode to the rim of the cathode during most of the run. This surface mode occurred after a front portion of the conical cathode tip separated from the cathode early in the run before lithium began to flow. The separation resulted from erosion caused apparently by the arc concentrating with high intensity on a region of the conical surface a few millimeters behind the tip.

This eroding condition developed due to a fault in the electrical instrumentation which indicated power input considerably lower than its actual level. This fault was not discovered until after the test was completed. The power input was actually too high for the mass-flow-rate and the cathode tip overheated.

The separation was fortuitous in that it provided direct observation of the differences in thruster operation and performance in the two modes of operation. When the tip separated the arc voltage decreased, thrust decreased, power loss to the cathode increased and the diameter of the cathode jet increased in correspondence with the larger diameter at the cathode where the arc attached.

#### (1) Overall Efficiency and Specific Impulse Characteristics

The thrust efficiency (not including magnet-coil and feed system power) is shown in Figure 32 as a function of specific impulse for Models LAJ-AF-CG-1A and 1B. Model 1A with one magnet coil located behind the anode was as shown in Figure 26. Model 1B had the same electrode configuration as 1A but another magnet coil, identical to that used with Model 1A, was installed in front of the anode. These two coils were connected in series, "aiding" so that the field strength

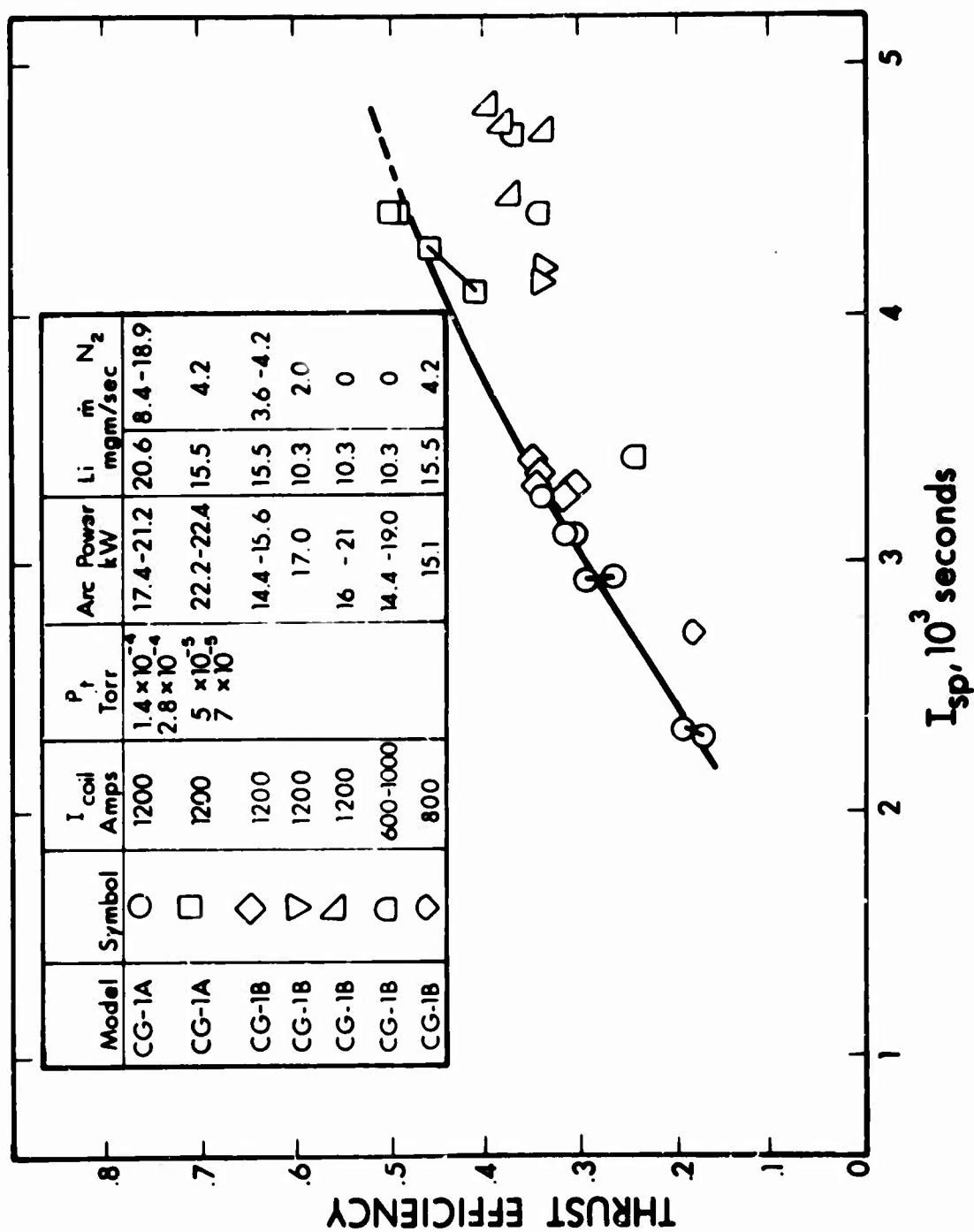


Figure 32 Thrust Efficiency versus Specific Impulse

(for the same coil current) in the electrode region and in the discharge region downstream of the electrodes was considerably increased (twice as strong at the anode face). The distribution of the axial field strength on the centerline is shown in Figure 33 for both configurations.

As Figure 32 shows, the efficiency ranges up to 50 percent at an  $I_{sp}$  of about 3500 sec for Model CG-1A and up to 40 percent at an  $I_{sp}$  of about 3800 sec for Model CG-1B. The difference in performance is believed to be caused by the different cathode attachment modes as described above. It is also felt that Model 1B performance in the tip attachment mode will be somewhat better than Model 1A based on the observations that: (1) the thrust per unit arc current is higher in this mode; (2) the thrust increases with increasing magnetic field strength; and (3) the cathode power loss is lower in the tip mode.

## (2) Thermal Efficiency Characteristics

The thermal efficiency is shown in Figure 34 as a function of specific impulse for both the 1A and 1B versions of the CG thruster configuration. These data are somewhat uncertain for two reasons.

In the Model 1A tests, radiation from only the rear portion of the anode is absorbed by the magnet coil housing. Power radiated from the front (downstream side) of the anode, along with the total jet power, is absorbed primarily by the tank walls. In order to estimate the thermal efficiency data shown in Figure 34 the total anode power loss was assumed to be twice that absorbed by the magnet housing. The efficiency was then calculated from

$$\eta_{\text{thermal}} = 1 - \frac{P_{\text{cathode}} + 2 P_{\text{magnet housing}}}{V_{\text{arc}} I_{\text{arc}}}$$

The power loss data for this run appeared to be very accurate, based on comparison of the electrical power with the sum of the powers transferred to the various water-cooling circuits.

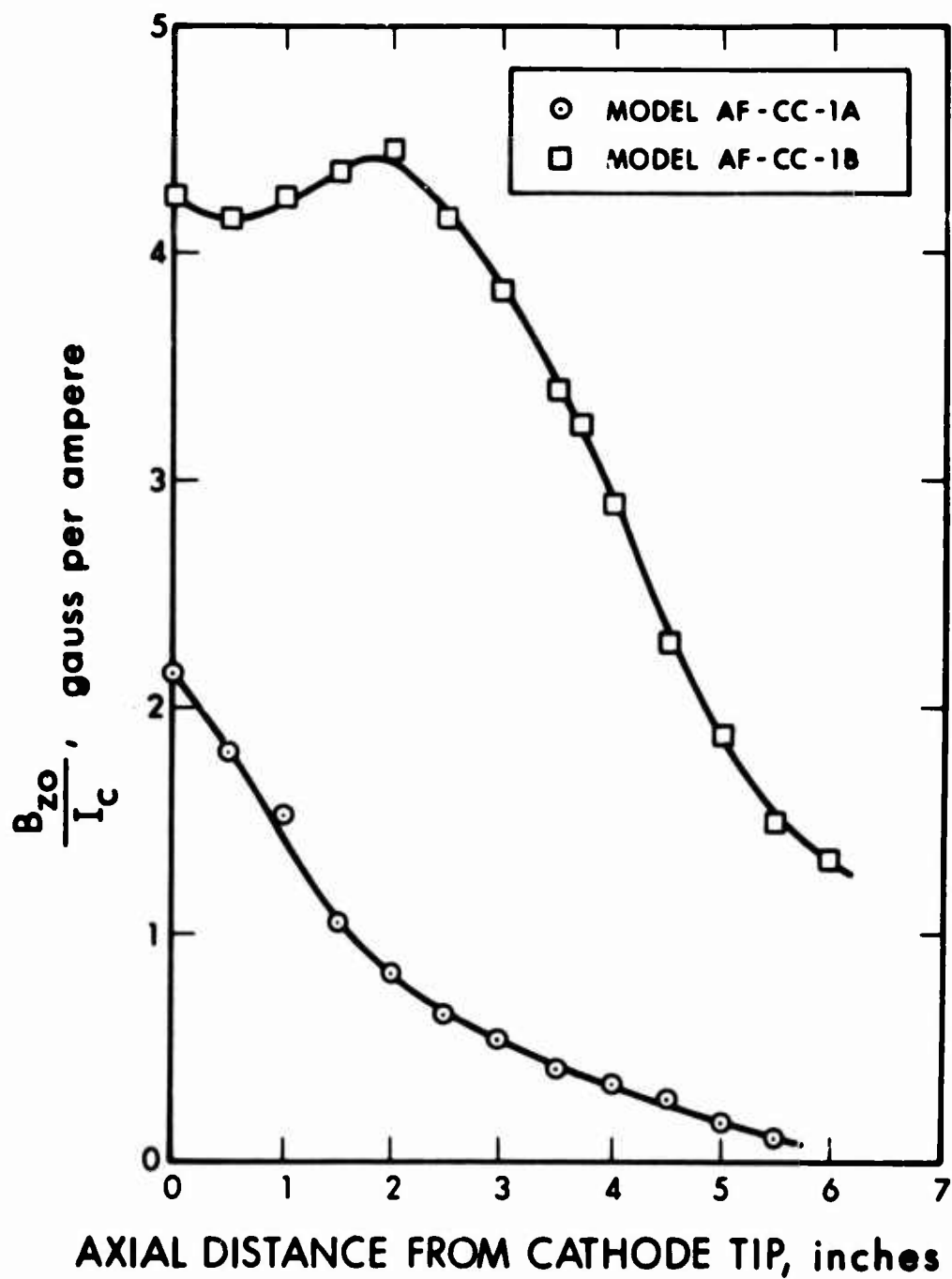


Figure 33 Axial Magnetic Field at Coil Centerline for Thrustor Models AF-CC-1A and 1B

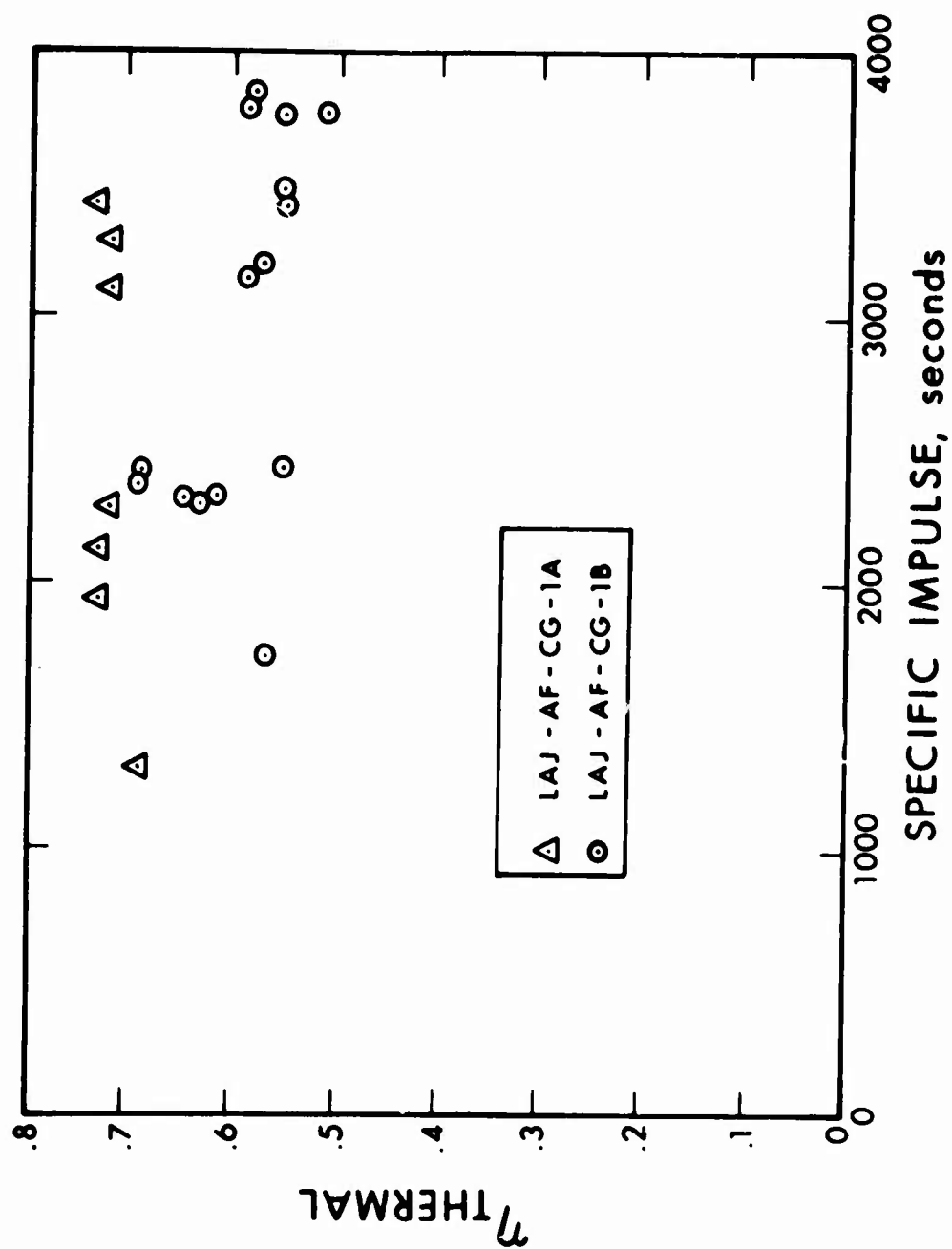


Figure 34 Thermal Efficiency versus Specific Impulse, Models AF-CG-1A and 1B

With Model 1B the anode radiation is mostly absorbed by the two magnet housings since the view factor between the anode and the tank walls is very low. The problem with this run was the previously described fault in instrumentation which resulted in an erroneous indication of arc voltage. Thus, there was no direct measurement of electrical power input. The power input was assumed to be equal to the total power in the cooling-water circuits. This seems to be valid in view of the good agreement between the two values in the previous run. The thermal efficiency for Model 1B was calculated from

$$\eta_{\text{thermal}} = \frac{P_{\text{tank}}}{\Sigma P_{\text{water circuits}}}$$

The principal difference in the thermal efficiency between the two versions was again in the cathode power loss as a result of the different cathode arc-attachment modes. This is shown in Figure 35 where it is seen that the effective cathode voltage drop was about 5 volts for Model 1A and about 7 to 11 volts for Model 1B.

### (3) Parametric Effects

The effects of the independent parameters — arc current, mass-flow-rate, coil current (magnetic field strength), and tank pressures — are shown in Figures 36, 37 and 38. Figure 36 is a plot of thrust per unit current as a function of the parameter  $\psi$ . This parameter, as shown by the theory, should properly correlate the effects of mass-flow-rate and arc current. Figure 36 indicates that the thrust per unit current was higher with Model 1A for the reasons previously discussed. The data in Figure 36 were taken with a wide variation in magnetic field strength. The maximum field strength was the 1200 amp condition with Model 1B and the minimum field strength was the 1200 amp condition with Model 1A (see Figure 33). All three of the curves on Figure 36 show the tendency for the thrust per unit current to increase with increasing  $\psi$  up to some asymptotic level. Although



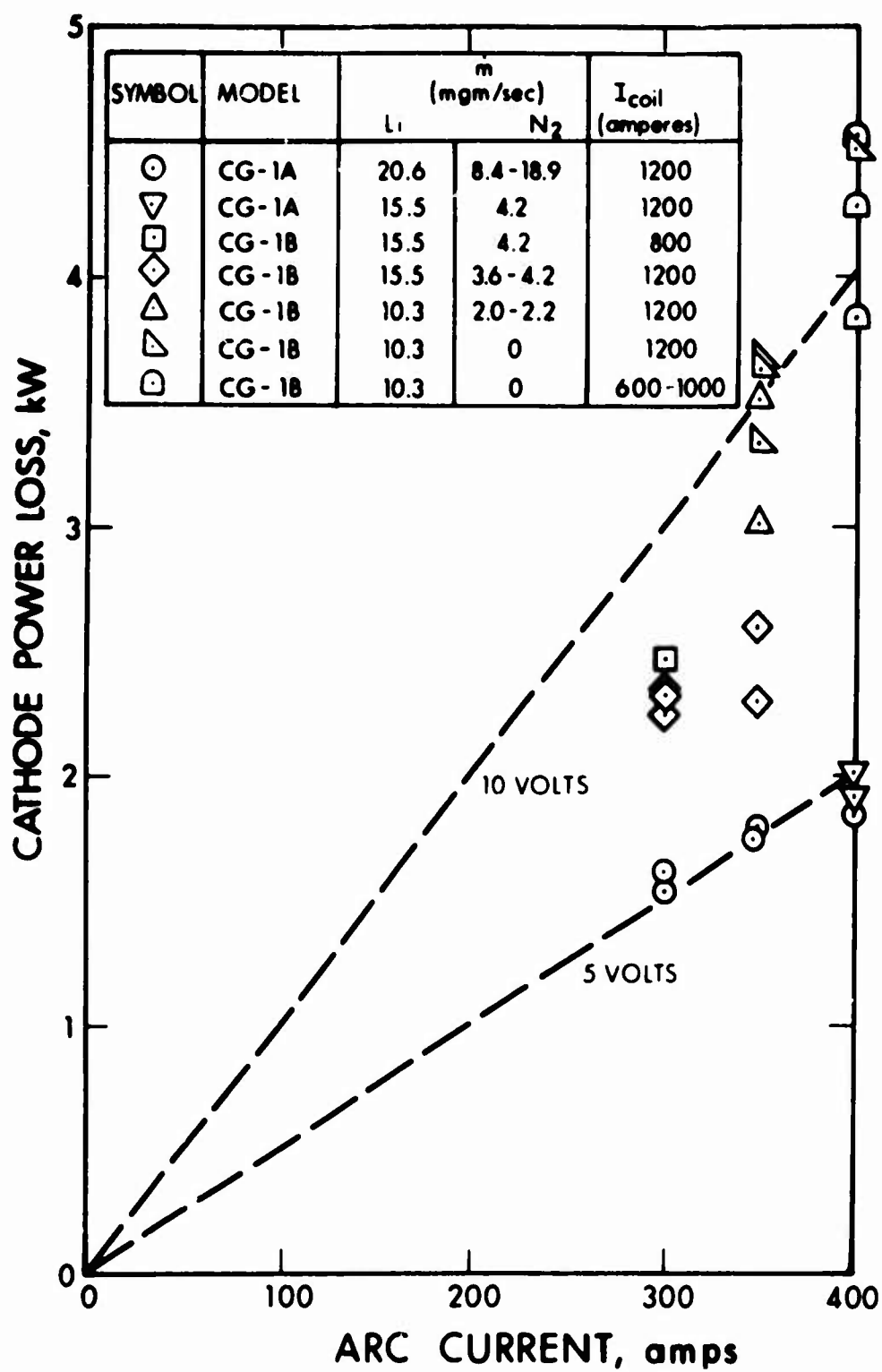


Figure 35 Cathode Power Loss versus Arc Current for Models AF-CG-1A and 1B

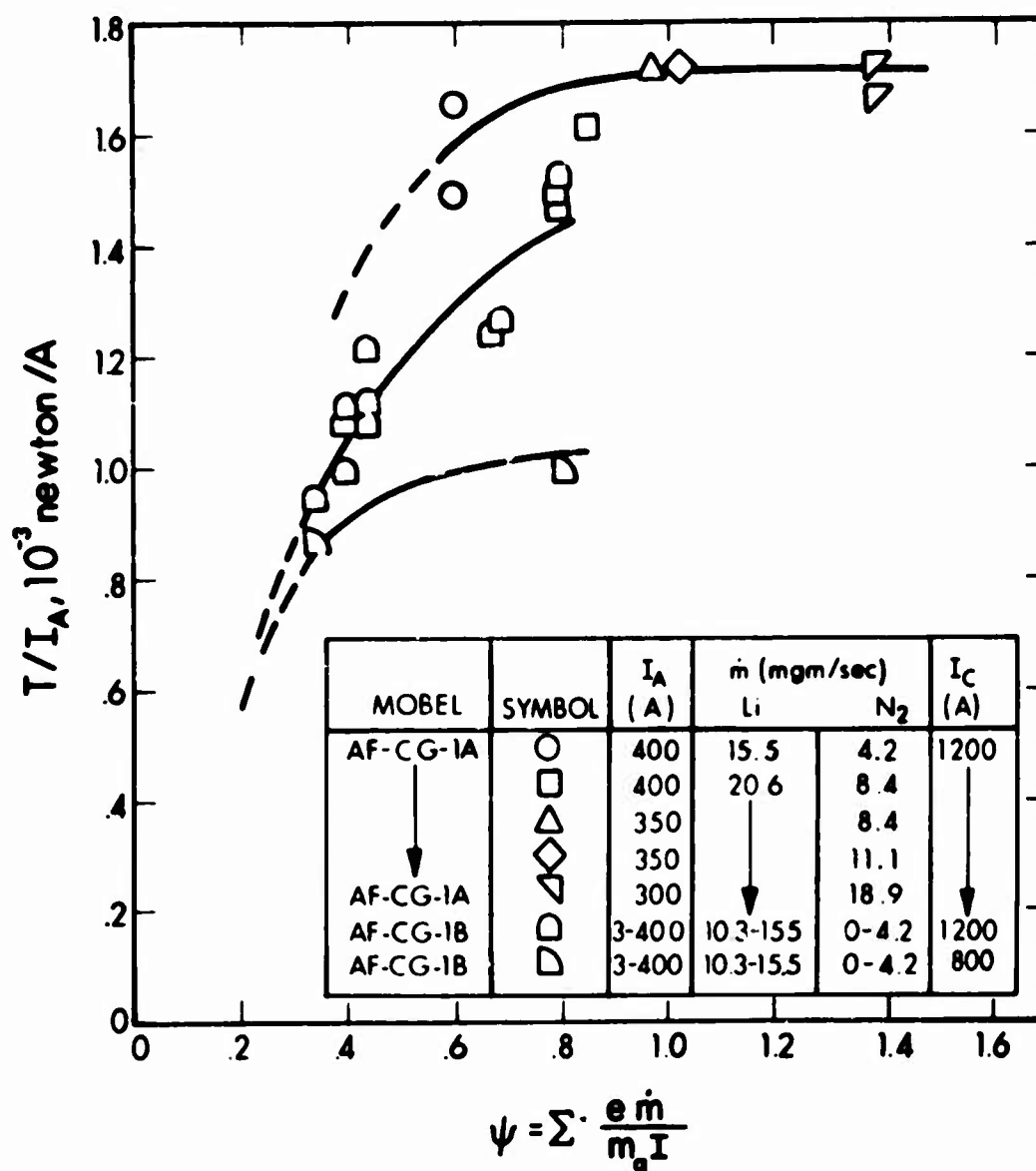


Figure 36 Thrust per Unit Arc Current versus the Parameter  $\psi$  for Models AF-CG-1A and 1B

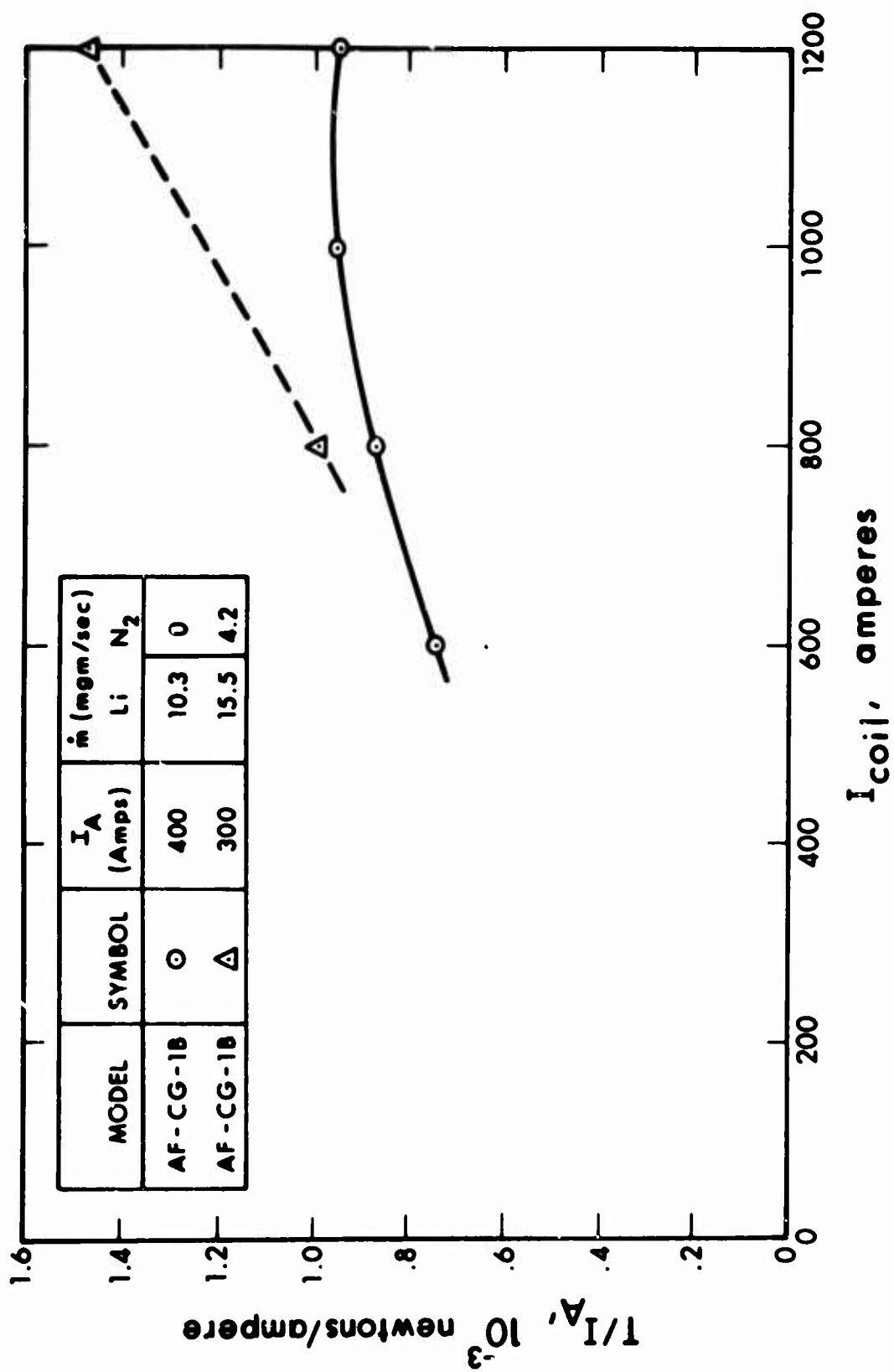


Figure 37 Effect of Magnetic-Coil Current on Thrust to Arc Current Ratio, Model AF-CG-1B

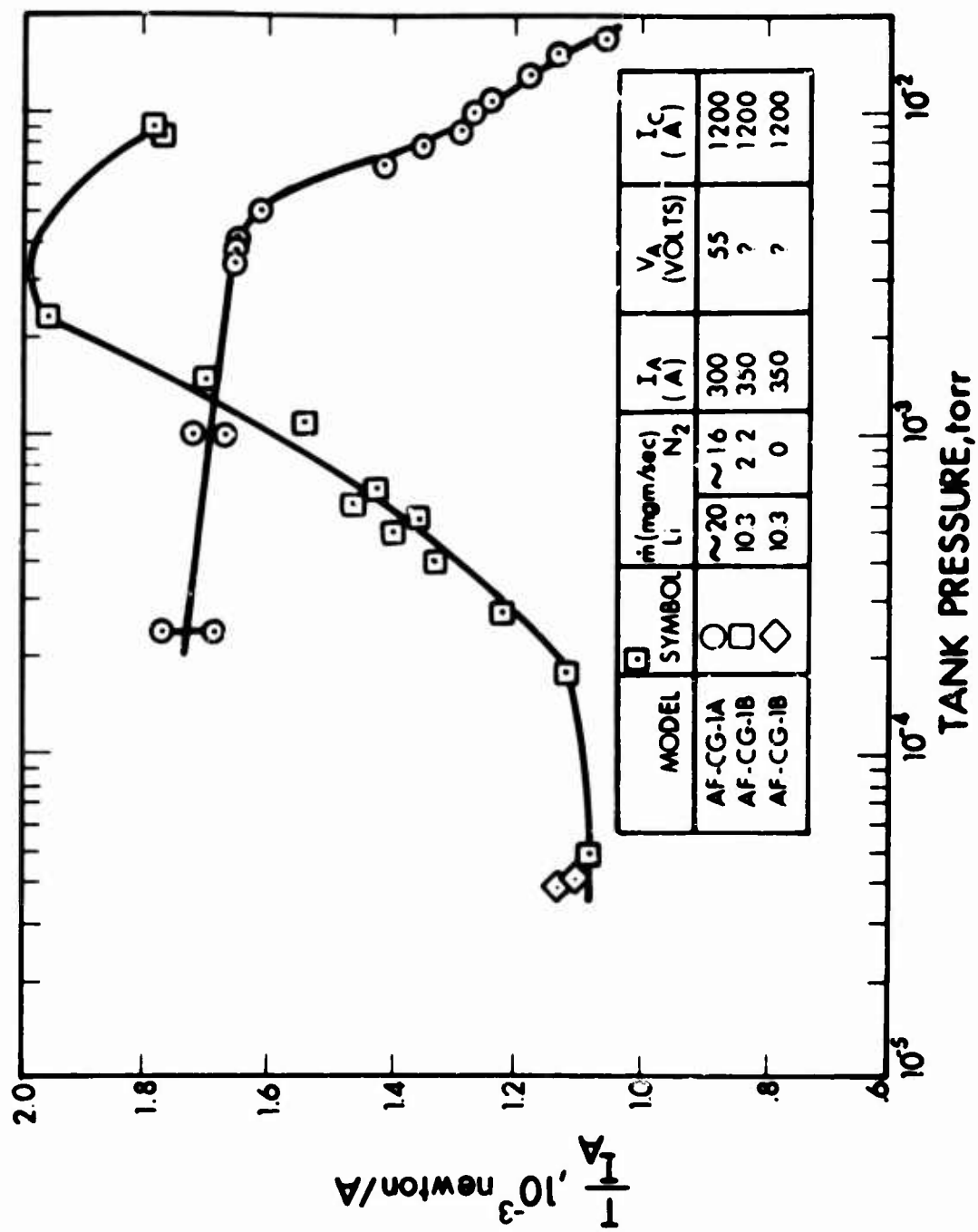


Figure 38 Thrust to Arc Current Ratio versus Tank Pressure for Models AF-CG-1A and 1B

there are some scatter in the data, the parameter  $\psi$  still appears to provide the proper correlation of thrust measurements at a constant magnetic field strength.

The effect of magnetic field strength is shown more directly for Model 1B in Figure 37 where thrust per unit current is plotted as a function of the coil current. Clearly there appears to be a strong effect of the mass-flow-rate on the influence of the magnetic field strength. At the lower mass-flow-rate an asymptotic level of thrust per unit current appears to exist above a coil current of 1000 amperes, where the field strength at the anode face is about 4000 gauss. At the higher mass-flow-rate there are not sufficient data to make a firm conclusion; however, it appears that thrust per unit current increases linearly with magnetic field strength and does not reach an asymptotic level even at a value of the field strength of 4800 gauss. Additional data are needed to further clarify the influence of both mass-flow-rate and magnetic field strength on the thrust characteristics.

Figure 38 shows the effect of test chamber pressure on the thrust per unit current for Models 1A and 1B. The two sets of results were taken under somewhat different conditions and it is not clear whether the great difference in the characteristics is dependent on how the tests were conducted. With Model 1A the thrust and pressure data were recorded during a transient condition. The measurements were taken after the test chamber was vented to the diffusion pump over a period of about three minutes, during which time the test chamber was pumped down from the equilibrium pressure of about 10 to 20 microns to the lower equilibrium pressure of about  $2 \times 10^{-4}$  torr. As Figure 38 shows, the thrust increased as the pressure decreased and achieved an asymptotic condition at about  $10^{-3}$  torr. For the Model 1B tests it was decided to bleed argon into the tank to control the pressure at steady state conditions for obtaining the effects of tank pressure on thrust. Figure 38 shows that under these conditions the thrust had a maximum

value at about 3 to 4 microns and decreased as the pressure decreased, again reaching an asymptotic level at about  $2 \times 10^{-4}$  torr. These results must be considered tentative at this time — they do not necessarily show that the previous results obtained during the transient are erroneous nor do they show conclusively that the two thruster versions have different characteristics. It is possible that the flow which was injected into the tank induced a circulating flow pattern which caused an erroneous thrust indication.

In the tests just described with the CG-1A and 1B gas-stabilized cathode configurations the boron-nitride shroud around the cathode was not totally satisfactory for long endurance. Therefore, this shroud was replaced by the tungsten buffer-shroud shown in Figure 31 which is a drawing of Models CG-1C and CG-1D.

The tests described below with these versions of the CG thruster indicated that this design is capable of long endurance and high efficiency with the magnet-coil power at a low level compared to the arc power input.

The effects of the field strength and the magnet power level on engine performance are indicated in a meaningful way through the power-to-thrust ratio. Power per unit thrust for the CG-1C and CG-1D engine configurations is shown in Figure 39 as a function of magnet current in two ways — one where magnet power is not included and the other with actual magnet power added to the arc power. The difference between the two curves of Figure 39 represents the power penalty of the magnet and it is seen that this penalty can be small without excessive loss of performance. This penalty can be further reduced by optimizing both the coil internal design and the magnetic field shape.

Power per unit thrust is an appropriate parameter because the efficiency within the  $I_{sp}$  range of interest is roughly proportional to  $I_{sp}$ . If it were exactly proportional, the power per unit thrust would be constant and the  $I_{sp}$  would not have any



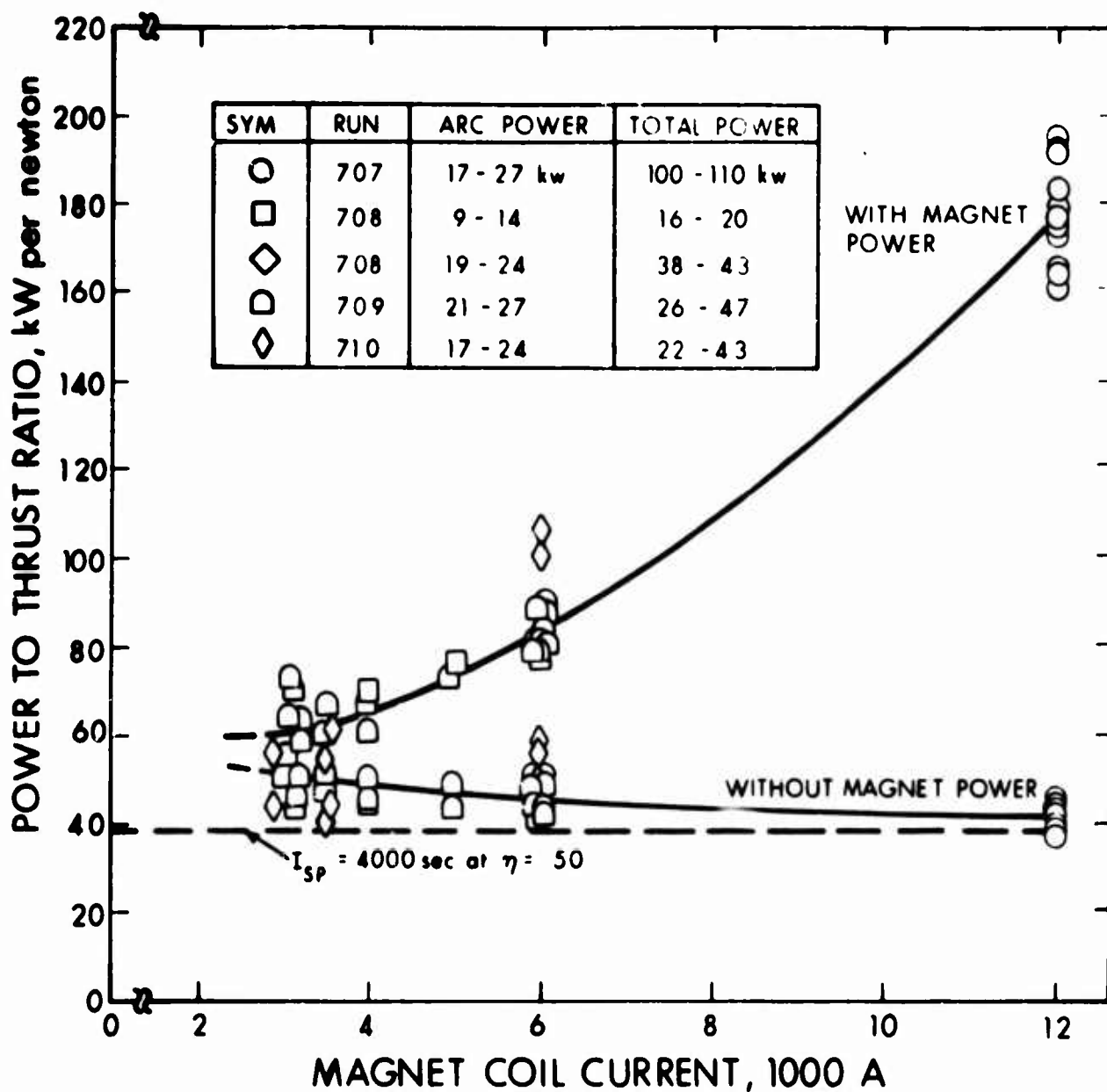


Figure 39 Power to Thrust Ratio for Model LAJ-AF-CG-1 versus Magnet Coil Current

significance. Actually, in this case, the optimum  $I_{sp}$  for any mission would be at the maximum  $I_{sp}$  available, disregarding any effects on life-time.

The effects of magnetic-field strength and magnet-power on thermal efficiency are shown in Figure 40 where thermal efficiency is plotted versus the magnet coil current. These data indicate that the electrode losses as a percentage of the power into the arc increase slightly as the magnetic field strength is decreased. This behavior is caused by a decrease of the discharge voltage while the effective voltage loss at the electrodes remains about constant. Though an efficiency based on inclusion of magnet power is not strictly a thermal efficiency, it is of interest because it may have a maximum value, as the lower curve in Figure 40 shows.

The efficiency -  $I_{sp}$  characteristics of the CG engines are shown by Figures 41, 42 and 43. Figure 41 shows the results for both nitrogen and hydrogen as the cathode gas. As expected it was possible to operate the engine at lower mass-flow-rates with hydrogen and hence higher specific impulse than with nitrogen. Also, the thrust efficiency was slightly higher (at the same  $I_{sp}$ ) when hydrogen was used. Though not shown graphically, the thermal efficiency was considerably higher with hydrogen (76 to 79 percent) than with nitrogen (66 to 68 percent). The correct explanation for this large difference is not clear at the present time but will be pursued since it may provide more insight into the acceleration processes.

Figure 42 shows additional performance data for the CG-1C engine at lower magnetic field strengths than in Figure 41. The efficiency is slightly lower (as also indicated by Figure 39) due to the weaker field. This run was extended over a period of about 4 hours to yield information about the endurance capability. The performance over the 4 hour period is represented by the cluster of data points in the  $I_{sp}$  range of 4200 to 4600 seconds. Throughout the period there was intermittent attachment of the discharge to the test chamber wall causing the scatter of results.

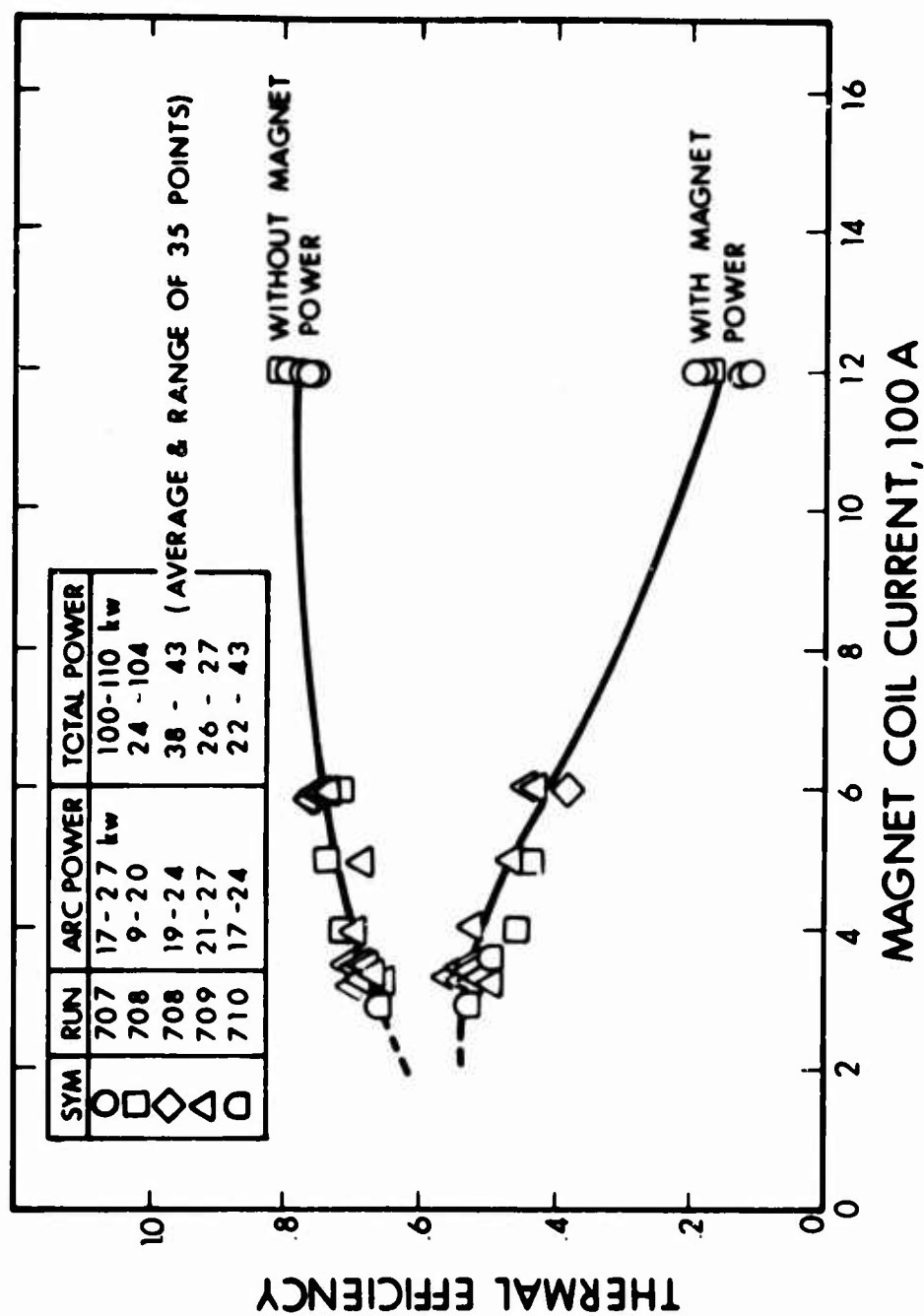


Figure 40 Thermal Efficiency of Model LAJ-AF-CG-1 versus Magnet Coil Current

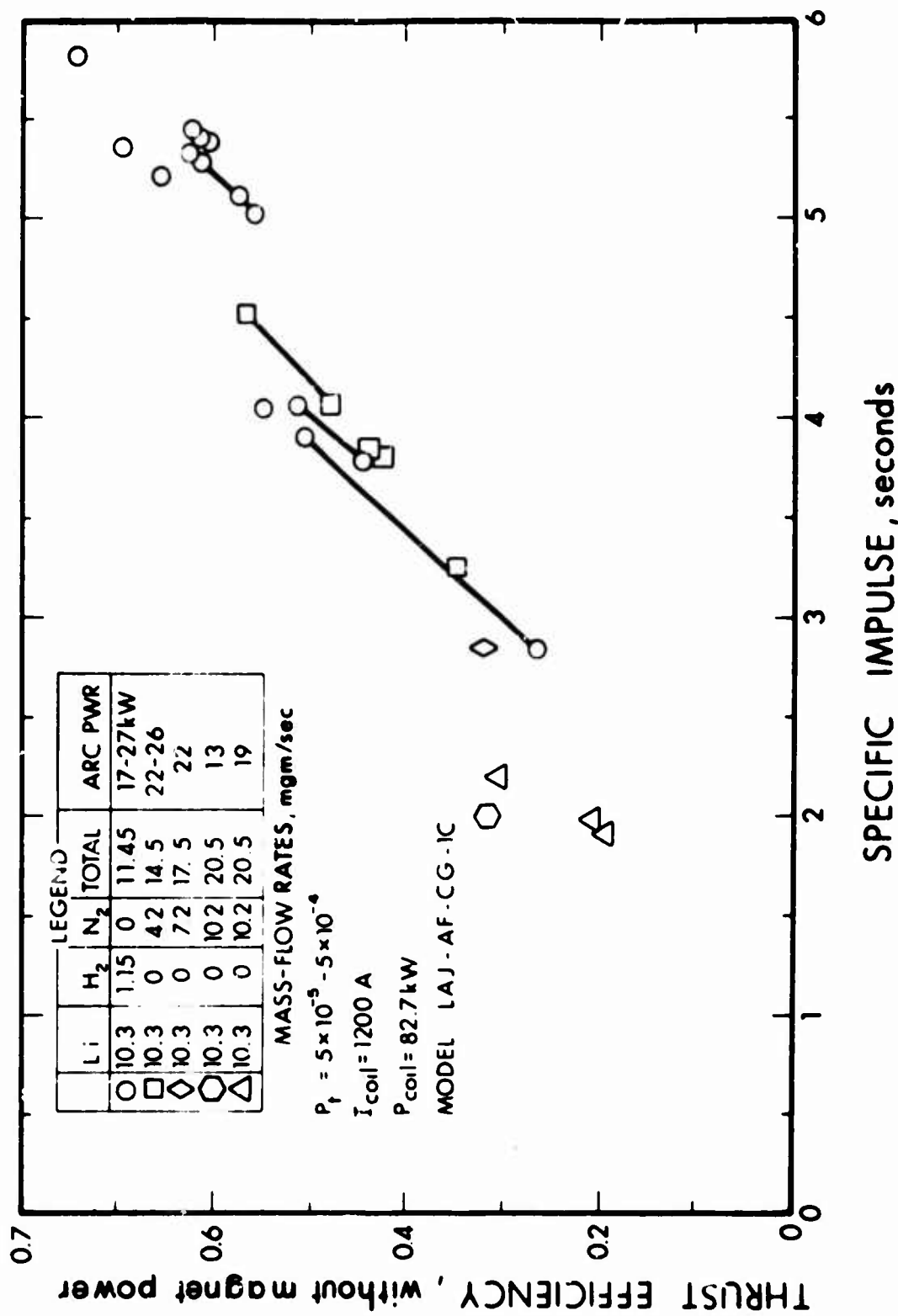


Figure 41 Thrust Efficiency versus Specific Impulse for Model LAJ-AF-CG-IC

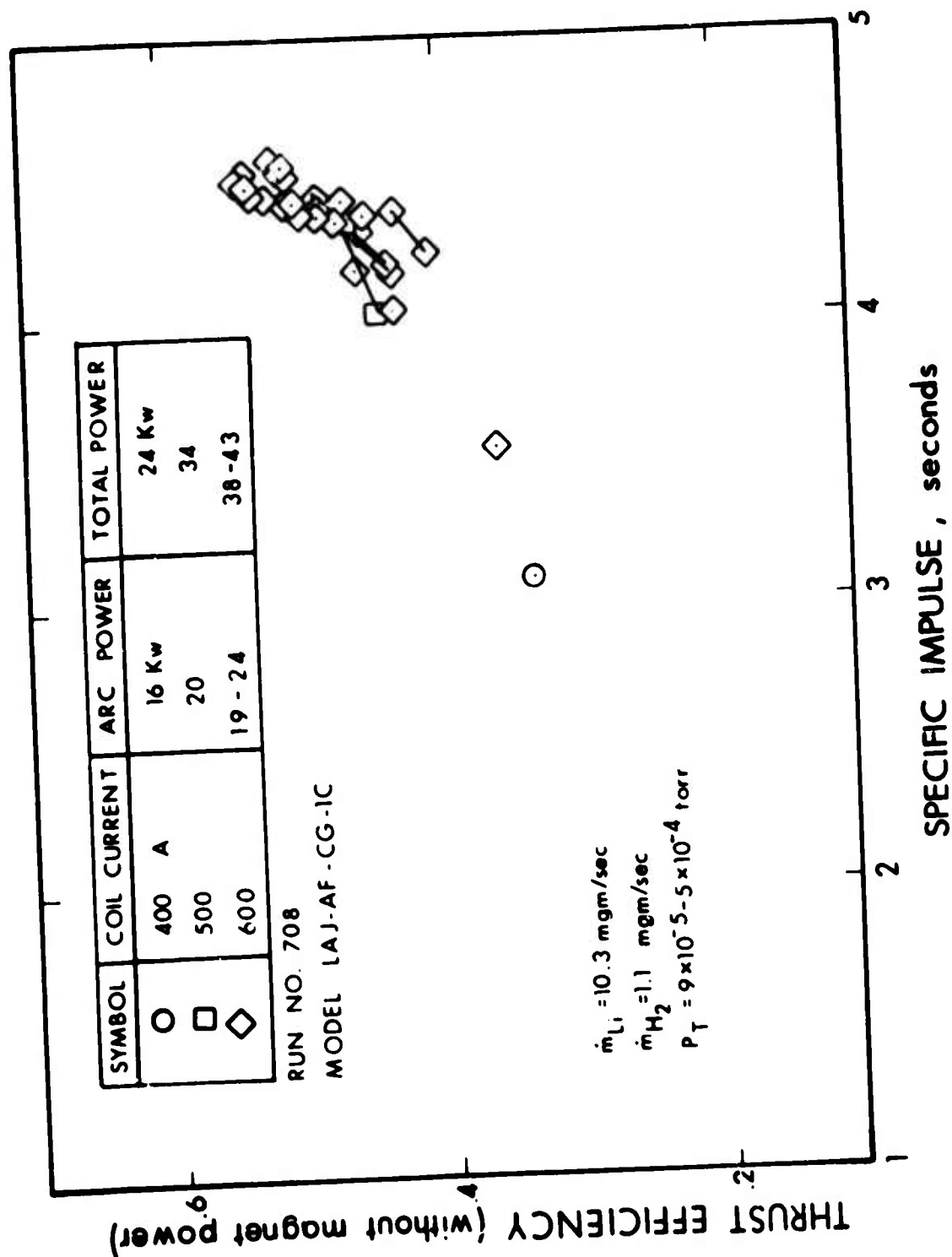


Figure 42 Thrust Efficiency versus Specific Impulse for Model LAJ-AF-CG-1C

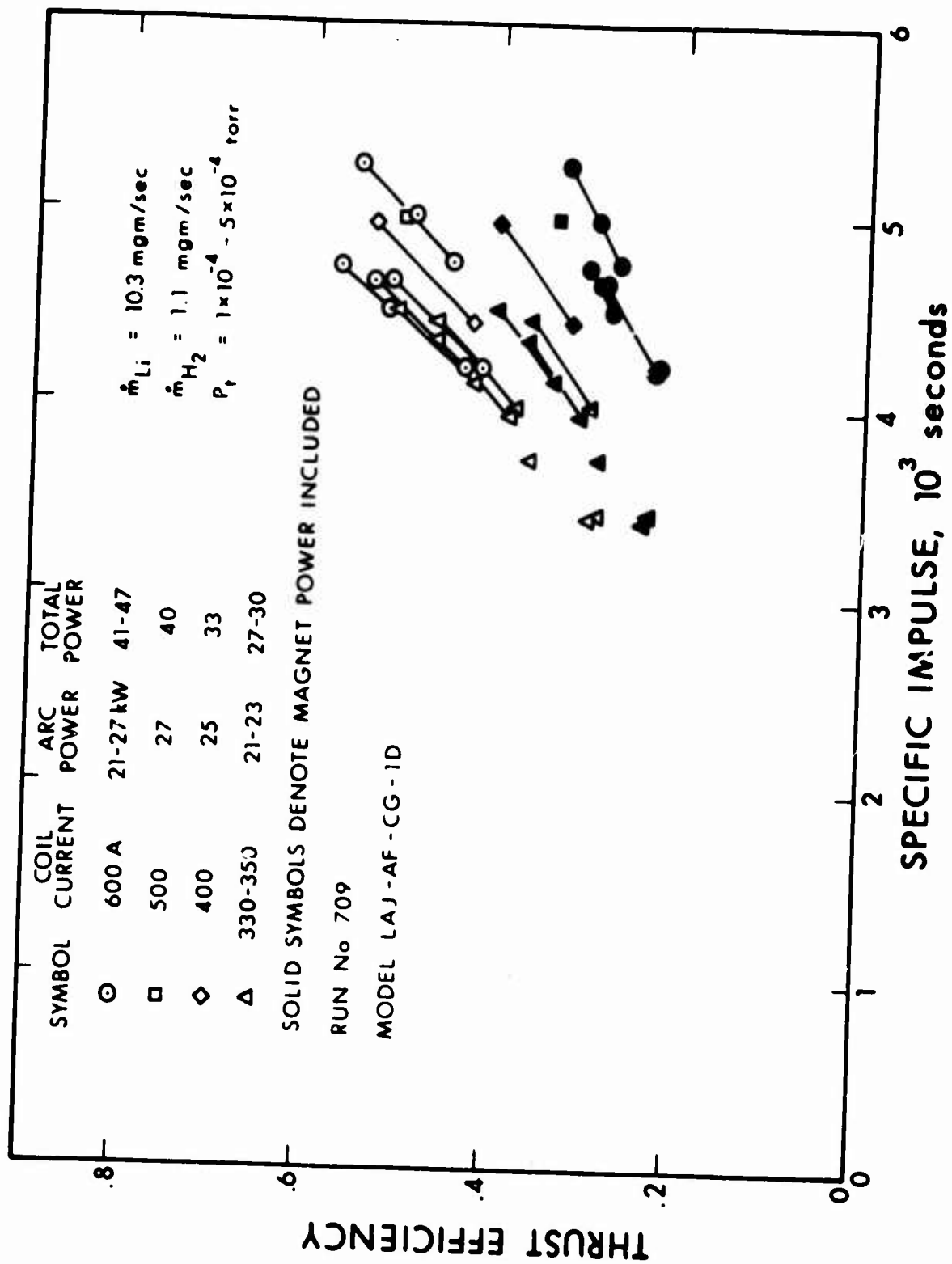


Figure 43 Thrust Efficiency versus Specific Impulse for Model LAJ-AF-CG-1D



Figure 43 shows results for still lower field strengths and were obtained with a slightly modified magnetic field shape (Model LAJ-AF-CG-1D). The downstream coil of the double-coil magnet was moved downstream 1/2 inch to give a stronger field gradient at the cathode tip. The intent of this shift was to provide for more stable attachment of the discharge at the cathode tip. Figure 43 includes efficiency calculated both with and without the magnet power included.

The lines between points in Figures 41, 42 and 43 connect the measurements of maximum and minimum thrust during oscillations. These oscillations were caused by attachment of the discharge to the chamber, fluctuation of the lithium feed rate, or unstable attachment at the cathode tip.

As a result of the extended magnetic-field configuration used in this engine, the discharge partly attached periodically to the wall of the tank opposite the engine. The chamber interference is not a matter of low leakage currents through the tank and cathode jet (as observed in the 10 kW test at NASA-LRC, Ref. 6). Rather it appears that a local current loop existed from the anode sheath through the tank wall (radially) and then through the cathode jet. It occurred intermittently, as observed by luminous discharge spots on the wall. It appears that the thrust is lower during such attachment as expected from the probable acceleration mechanisms of the engine (i.e., the current through the plasma across magnetic field lines is lower). Because of the tank interference problem, additional investigation of this engine, the endurance test, and other events representing completion of the second phase of the contract were delayed until a longer test chamber was provided. The chamber was extended by adding an existing EOS 6 x 8 chamber to the USAF 6 x 6 lithium chamber as shown in Figure 44. The resulting 6 x 14 chamber combination was too large for the old laboratory at 125 North Vinedo and was installed in the new lab at 250 North Hinstead.

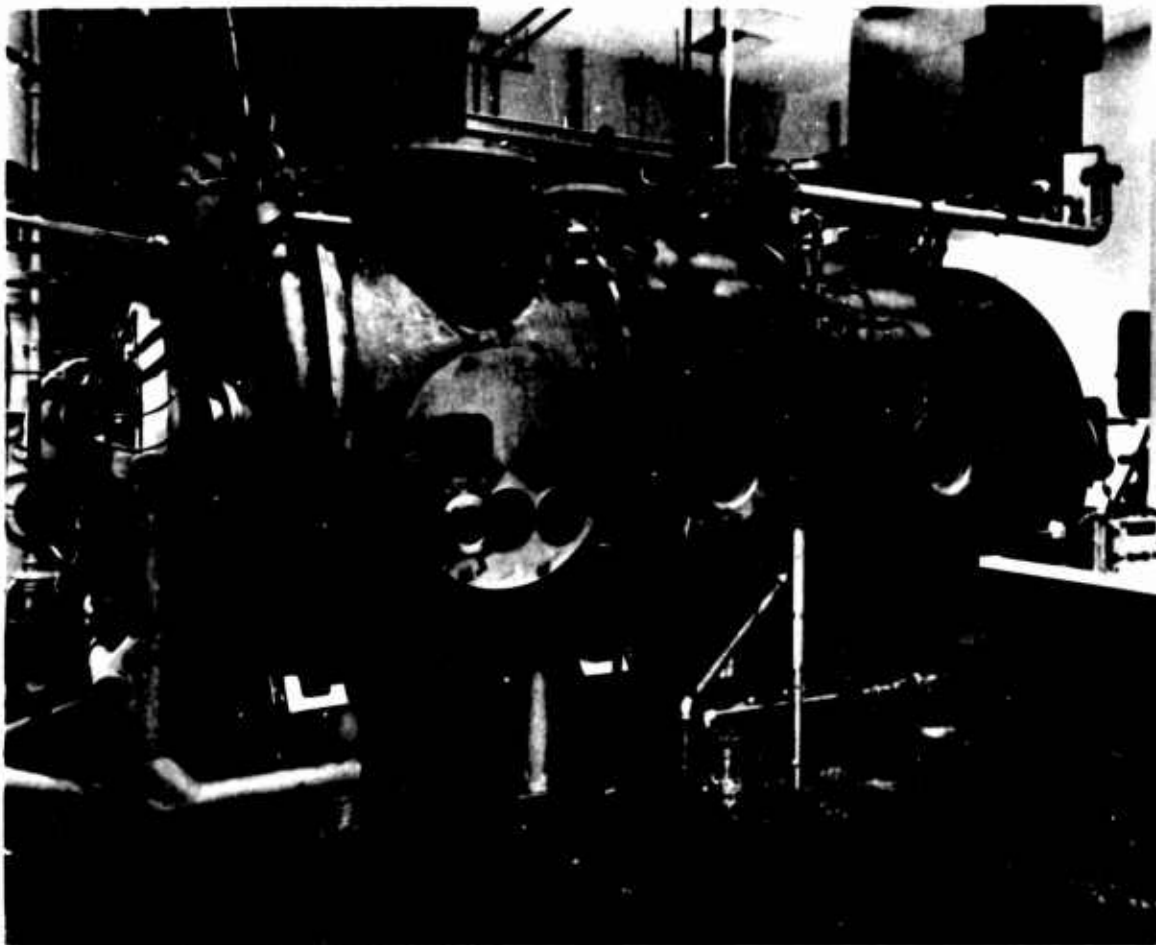


Figure 44 Photograph of Extended Propulsion Test Chamber (6 x 6 foot Chamber Converted to 6 x 14 foot chamber)

Subsequent tests in the extended chamber were directed primarily toward demonstrating endurance capability. However, the engine performance agreed closely with the data from the 6 x 6 chamber presented above.

## SECTION VIII

### ENDURANCE TESTS

Tests to determine the lifetime of the engine were started in the 6 ft x 6 ft tank. It was discovered that after several hours of operation the discharge would attach intermittently to the end of the vacuum chamber. It was postulated that this occurred because of the buildup of lithium on the tank walls. An attempt to stop this attachment was made by mounting an 18 inch diameter water cooled target in the tank. This target was electrically insulated from the tank and from the arc electrodes. This did not solve the problem, as the discharge was found to now attach intermittently to the target after several hours of running time. This problem appeared serious enough to discontinue the tests and modify the facility. An 8 ft x 6 ft tank was added to the 6 ft x 6 ft tank and two more diffusion pumps were attached to the new section.

A number of tests were conducted in the enlarged facility. During one 2-hour run it was found that the flow rate of propellant was not steady. The observations indicated that the flow tended to oscillate around the mean flow rate with a period of about 1 hour. When the flow rate fell below the mean value the following effects were observed:

1. The arc voltage would increase
2. The anode power loss would increase
3. The thrust would drop
4. The anode and insulator would heat up and particles of insulator material would erode off in an intermittent manner.

The engine tended to flood when the flow rate became greater than the mean. Liquid droplets of lithium would form on the anode and sputter out of the engine. When this occurred the arc voltage would decrease, the anode power loss would decrease and the thrust would increase.

The unevenness in feed rate was eventually traced directly to the bellows feeders and their interaction with the vaporizer. Two approaches to solving the problem were taken. First, the bellows feed systems were overhauled and attempts made to determine the exact reason for their periodic behavior.\* Second, a new high capacity feed system was designed and fabricated which operated on the vapor feed principle, i.e., it used a sonic orifice to control and measure the feed rate. Since this approach involved a considerable effort, it was decided in conjunction with APL, Wright-Patterson Air Force Base, to postpone the attempt to obtain 50 hours run time on one engine until later in the program. The data obtained from this series of tests (Runs 711 to 724) are reported in Tables I and II of Appendix I.

---

\* Because of these fluctuations, some of the overall efficiencies computed in Appendix I must correspondingly vary above and below the values associated with the appropriate average mass flow rate.

APPENDIX I

TEST DATA



TABLE 1 SUMMARY OF TESTS CONDUCTED

<u>Run Number</u>	<u>Date</u>	<u>Elapsed Time (hrs/min)</u>	<u>Configuration</u>	<u>Propellant</u>	<u>Chamber</u>	<u>Feed System</u>
<u>High Vacuum Tests</u>						
672	4-29-65	:28	AF-6D	Li	5x12	Bellows
673	5-2-65	:54	AF-6D	Li	5x12	Bellows
674	5-4-65	:10	AF-6D	Li	5x12	Bellows
<u>Potassium Tests</u>						
675	5-28-65	1:05	AF-6D	K	6x6	Bellows
676	6-3-65	:45	AF-6D	K	6x6	Bellows
677	6-17-65	2:10	AF-6D	K	6x6	Bellows
678	6-29-65	:51	AF-6D	K	6x6	Bellows
679	7-7-65	:33	AF-6D	K	6x6	Bellows
680	7-8-65	1:38	AF-6D	K	6x6	Bellows
681	7-20-65	1:45	AF-6D	K	6x6	Bellows
682	11-8-65	—	BF-1	K	6x6	Boiler
683	11-15-65	—	BF-1	K	6x6	Boiler
684	11-23-65	—	BF-1	K	6x6	Boiler
685	12-1-65	1:00	BF-1B	K	6x6	Boiler
686	12-15-65	:20	BF-1C	K	6x6	Boiler
687	12-16-65	:20	BF-1C	K	6x6	Boiler
688	12-16-65	:20	BF-1	K	6x6	Boiler
689	12-17-65	:10	BF-1	K	6x6	Boiler
690	12-17-65	:35	BF-1	K	6x6	Boiler
691	12-23-65	:10	BF-1C	K	6x6	Boiler
692	1-6-66	:45	BF-1D	K	6x6	Boiler
<u>Buffer Configuration Tests</u>						
693	1-24-66	:25	BF-1E	Li	6x6	Boiler
694	1-29-66	—	BF-1E	Li	6x6	Boiler
695	1-31-66	1:00	BF-1E	Li	6x6	Boiler
696	2-9-66	:10	BF-1E	Li	6x6	Boiler
697	2-16-66	—	BF-1E	Li	6x6	Boiler

TABLE I SUMMARY OF TESTS CONDUCTED (contd)

<u>Run Number</u>	<u>Date</u>	<u>Elapsed Time (hrs/min)</u>	<u>Configuration</u>	<u>Propellant</u>	<u>Chamber</u>	<u>Feed System</u>
698	2-21-66	1:40	BF-1E	L1	6x6	Boiler
699	2-22-66	1:30	BF-1E	L1	6x6	Boiler
700	3-2-66	:40	AF-BG-1	L1/N <sub>2</sub>	6x6	Bellows
701	3-11-66	2:03	AF-BG-1	L1/N <sub>2</sub>	6x6	Bellows
702	3-22-66	3:41	AF-BG-1A	L1/N <sub>2</sub>	6x6	Bellows
<u>Magnet Configuration Tests</u>						
703	3-28-66	—	AF-CG-1	L1/N <sub>2</sub>	6x6	Bellows
704	3-31-66	1:25	AF-CG-1	L1/N <sub>2</sub>	6x6	Bellows
705	4-11-66	3:00	AF-CG-1B	L1/N <sub>2</sub>	6x6	Bellows
706	4-19-66	—	AF-CG-1C	L1/H <sub>2</sub> , L1/N <sub>2</sub>	6x6	Bellows
707	4-26-66	2:08	AF-CG-1C	L1/H <sub>2</sub> , L1/N <sub>2</sub>	6x6	Bellows
708	5-6-66	4:17	AF-CG-1C	L1/H <sub>2</sub>	6x6	Bellows
709	5-9-66	3:05	AF-CG-1D	L1/H <sub>2</sub>	6x6	Bellows
710	5-12-66	:38	AF-CG-1D	L1/H <sub>2</sub>	6x6	Bellows
<u>Endurance Tests</u>						
711	6-30-66	:09	AF-CG-1D	L1	6x6 + 6x8	Bellows
712	7-1-66	—	AF-CG-1D	L1	6x6 + 6x8	Bellows
713	7-6-66	—	AF-CG-1D	L1	6x6 + 6x8	Bellows
714	7-7-66	1:24	AF-CG-1D	L1/H <sub>2</sub>	6x6 + 6x8	Bellows
715	7-8-66	:28	AF-CG-1D	L1/H <sub>2</sub>	6x6 + 6x8	Bellows
716	7-8-66	4:13	AF-CG-1D	L1/H <sub>2</sub>	6x6 + 6x8	Bellows
717	7-9-66	2:15	AF-CG-1D	L1/H <sub>2</sub>	6x6 + 6x8	Bellows
718	7-12-66	2:58	AF-CG-1D	L1/H <sub>2</sub>	6x6 + 6x8	Bellows
719	7-13-66	:54	AF-CG-1D	L1/H <sub>2</sub>	6x6 + 6x8	Bellows
720	7-14-66	9:16	AF-CG-1D	L1/H <sub>2</sub>	6x6 + 6x8	Bellows
721	7-15-66	4:50	AF-CG-1D	L1/H <sub>2</sub>	6x6 + 6x8	Bellows
722	7-20-66	1:15	AF-CG-1D	L1/H <sub>2</sub>	6x6 + 6x8	Bellows
723	7-28-66	9:04	AF-CG-1D	L1/H <sub>2</sub>	6x6 + 6x8	Bellows
724	8-8-66	6:47	AF-CG-1D	L1/H <sub>2</sub>	6x6 + 6x8	Bellows

TABLE II TEST RESULTS

Run No.	Point No.	I <sub>A</sub> amps	V <sub>A</sub> volts	P <sub>A</sub> kW	I <sub>C</sub> amps	$\dot{m}$ mg/sec	P <sub>t</sub> torr	P <sub>ca</sub> kW	P <sub>an</sub> kW	T grams	I <sub>sp</sub> sec	$\eta_b$ —
679	1	300	36.0	10.8	1800	40.0	$9.2 \times 10^{-4}$	1.31	1.60	50.6	1270	0.277
	2	300	39.5	11.9	1800	32.0	$4 \times 10^{-4}$	1.25	3.06	46.7	1460	0.276
	A	300	39.0	11.7	1800	41.0	—	—	—	48.2	1180	0.232
	B	300	37.5	11.3	1800	42.0	—	—	—	56.8	1350	0.328
680	1	200	28.0	5.60	1800	43.0	$3 \times 10^{-4}$	0.79	1.36	30.0	700	0.179
	2	300	36.5	11.0	1800	44.0	$2 \times 10^{-4}$	1.04	2.13	50.0	1140	0.249
	3	300	37.5	11.3	1800	46.0	$2 \times 10^{-4}$	1.15	2.87	50.2	1090	0.234
	A	200	38.5	7.70	1800	58.0	—	—	—	33.2	570	0.118
681	B	300	36.0	10.8	1200	—	—	—	—	—	—	—
	C	200	32.0	6.40	1200	31.0	—	—	—	—	—	—
	A	158	32.0	5.06	1800	32.5	$3.4 \times 10^{-4}$	0.82	1.48	26.6	820	0.207
	B	155	33.0	5.11	1800	32.5	$3.4 \times 10^{-4}$	0.82	1.48	26.2	808	0.199
681	C	250	39.5	9.88	1800	33.0	$3.0 \times 10^{-4}$	1.11	2.34	43.0	1300	0.274
	D	250	40.0	10.0	1800	33.3	$2.6 \times 10^{-4}$	1.21	2.68	41.8	1260	0.253
	E	250	40.5	10.1	1800	33.6	$2.6 \times 10^{-4}$	1.21	2.68	43.0	1280	0.262
	F	250	36.0	9.00	1600	33.6	$2.6 \times 10^{-4}$	1.23	2.96	43.0	1280	0.294
	G	250	36.0	9.00	1600	34.2	$2.6 \times 10^{-4}$	1.23	2.96	42.2	1240	0.280
	H	250	32.5	8.13	1400	34.2	$2.4 \times 10^{-4}$	1.19	2.76	38.0	1110	0.250
	I	250	32.5	8.13	1400	34.5	$2.4 \times 10^{-4}$	1.19	2.76	36.2	1050	0.225
	J	250	29.0	7.25	1200	34.6	$2.4 \times 10^{-4}$	1.10	2.37	35.0	1010	0.235
	K	250	29.5	7.38	1200	34.5	$2.3 \times 10^{-4}$	1.10	2.37	34.3	995	0.221

Thrustor Model: LAJ-AF-6D  
 Propellant: Potassium  
 Test Chamber: 6' x 6'

TABLE II TEST RESULTS (contd)

Run No.	Point No.	I <sub>A</sub> amps	V <sub>A</sub> volts	P <sub>A</sub> kW	I <sub>C</sub> amps	$\dot{m}$ mg/sec	P <sub>t</sub> torr	P <sub>ca</sub> kW	P <sub>an</sub> kW	T grams	I <sub>sp</sub> sec	$\eta_b$ —
681	L	250	26.5	6.63	1000	34.7	$2.6 \times 10^{-4}$	1.10	2.28	32.6	940	0.222
	M	250	26.3	6.56	1000	35.1	$2.4 \times 10^{-4}$	1.10	2.28	32.0	911	0.214
	N	250	24.0	6.00	800	35.0	$2.6 \times 10^{-4}$	1.13	2.03	29.7	850	0.203
	O	250	24.5	6.12	800	35.0	$2.6 \times 10^{-4}$	1.13	2.03	29.7	850	0.198
	P	250	38.5	9.62	1800	35.0	$1.8 \times 10^{-4}$	1.16	2.54	43.4	1240	0.268
	Q	250	38.5	9.62	1800	34.8	$1.8 \times 10^{-4}$	1.16	2.54	43.5	1250	0.272
	R	250	46.0	11.5	1800	20.9	$2.2 \times 10^{-4}$	1.49	4.23	35.3	1690	0.249
	S	250	46.0	11.5	1800	20.9	$2.4 \times 10^{-4}$	1.49	4.23	35.3	1690	0.249
	T	200	41.5	8.30	1800	21.0	$2.0 \times 10^{-4}$	1.33	3.48	31.2	1480	0.267
	U	195	42.0	8.20	1800	21.1	$2.0 \times 10^{-4}$	1.33	3.48	31.3	1480	0.271
	V	158	37.3	5.89	1800	21.3	$2.0 \times 10^{-4}$	1.01	2.25	26.4	1240	0.267
	W	154	38.0	5.85	1800	21.3	$2.0 \times 10^{-4}$	1.01	2.25	26.5	1240	0.265
	X	100	31.0	3.10	1800	21.3	$2.8 \times 10^{-4}$	0.81	1.44	14.7	690	0.157
	Y	100	30.5	3.05	1800	21.3	$2.8 \times 10^{-4}$	0.76	1.23	15.3	719	0.170
	Z	100	38.5	3.85	1800	21.3	$2.6 \times 10^{-4}$	—	—	15.4	1480	0.284
692	1	92	56	5.15	620	—	—	0.56	0.25	—	—	—
	2	160	26	4.16	620	24	—	0.87	0.69	16.0	670	0.125
	A	160	29	4.64	620	22	—	0.87	0.69	14.3	509	0.075
	3	200	30	6.00	620	20	—	0.95	0.87	12.1	605	0.059
	4	250	27	6.75	300	24	—	1.31	1.05	17.0	708	0.086
	5	250	35	8.75	600	27	$1.0 \times 10^{-4}$	1.40	1.25	26.0	963	0.137
	B	250	35	8.80	600	28	$1.0 \times 10^{-4}$	1.40	1.25	21.7	753	0.101

Thrustor Model: AF-BF-1D  
 Propellant: Potassium  
 Test Chamber: 6' x 6'

TABLE II TEST RESULTS (contd)

Run No.	Point No.	I <sub>A</sub> amps	V <sub>A</sub> volts	P <sub>A</sub> kW	I <sub>C</sub> amps	m mg/sec	P <sub>t</sub> torr	P <sub>ca</sub> kW	P <sub>an</sub> kW	T grams	I <sub>sp</sub> sec	η <sub>b</sub> —
692	6	300	43	12.9	600	24	1.0x10 <sup>-4</sup>	1.48	2.16	20.4	830	0.062
	C	300	43	12.9	600	26	1.0x10 <sup>-4</sup>	1.48	2.16	18.8	720	0.051
	7	305	44.5	13.57	750	21.5	1.0x10 <sup>-4</sup>	1.62	3.12	21.3	947	0.071
	D	305	44.5	13.57	750	21	1.0x10 <sup>-4</sup>	1.62	3.12	19.3	915	0.062
	8	350	46	16.10	750	20	1.0x10 <sup>-4</sup>	1.90	3.81	19.6	980	0.057
702	2A	168	47	7.90	400	18.4	1.6x10 <sup>-4</sup>	1.83	2.45	14.25	770	0.067
	2B	168	47	7.90	450	18.4	1.6x10 <sup>-4</sup>	1.83	2.45	15.0	815	0.067
	2C	168	47	7.90	500	18.4	1.6x10 <sup>-4</sup>	1.83	2.45	16.1	870	0.067
	3	168	50	8.40	500	18.4	1.4x10 <sup>-4</sup>	1.70	2.49	15.9	860	0.079
	4	168	50	8.40	600	18.4	1.4x10 <sup>-4</sup>	1.70	2.40	17.4	950	0.094
	5	163	54	8.80	800	18.4	1.4x10 <sup>-4</sup>	1.73	2.47	18.6	1010	0.103
	6	250	56	14.00	800	18.4	1.2x10 <sup>-4</sup>	1.83	2.71	27.4	1490	0.140
	7A	300	53	15.75	800	18.4	1.3x10 <sup>-4</sup>	1.95	3.54	32.3	1760	0.173
	7B	300	40	12.00	800	18.4	1.3x10 <sup>-4</sup>	1.95	3.54	25.5	1390	0.141
	8A	300	41	12.15	800	18.4	1.4x10 <sup>-4</sup>	2.10	3.53	25.5	1390	0.140
	8B	300	41	12.15	700	18.4	1.4x10 <sup>-4</sup>	2.10	3.53	23.6	1280	0.140
	8C	300	41	12.15	600	18.4	1.4x10 <sup>-4</sup>	2.10	3.53	21.4	1160	0.140
	8D	300	41	12.15	500	18.4	1.4x10 <sup>-4</sup>	2.10	3.53	19.5	1060	0.140
	9A	300	33	9.75	400	18.4	1.4x10 <sup>-4</sup>	2.12	3.53	19.2	1040	0.099
	9B	300	35	10.50	500	18.4	1.4x10 <sup>-4</sup>	2.12	3.53	21.8	1180	0.118
	9C	300	37	11.10	600	18.4	1.4x10 <sup>-4</sup>	2.12	3.53	22.8	1240	0.122
	9D	300	39	11.55	700	18.4	1.4x10 <sup>-4</sup>	2.12	3.53	24.2	1320	0.132
	9E	300	40	12.00	800	18.4	1.4x10 <sup>-4</sup>	2.12	3.53	25.5	1390	0.141

Thrustor Model: LAJ-AF-BG-1A  
 Propellant: Lithium/Nitrogen  
 Test Chamber: 6" x 6"

TABLE II TESTS RESULTS (contd)

Run No.	Point No.	I <sub>A</sub> amps	V <sub>A</sub> volts	P <sub>A</sub> kW	I <sub>C</sub> amps	m <sub>g</sub> /sec	P <sub>t</sub> torr	P <sub>ca</sub> kW	P <sub>an</sub> kW	T grams	I <sub>sp</sub> sec	η <sub>b</sub> —
702	10	350	41	14.35	800	18.4	1.0x10 <sup>-4</sup>	2.17	3.89	30.8	1670	0.172
	12	350	39	13.65	800	12.2	1.2x10 <sup>-4</sup>	2.22	5.01	25.8	2110	0.192
	13	300	39	11.70	800	12.2	1.1x10 <sup>-4</sup>	2.00	4.55	24.8	2030	0.207
	14	250	39	9.75	800	12.2	1.0x10 <sup>-4</sup>	1.58	3.61	22.0	1800	0.195
	15A	200	39	7.70	800	12.2	1.0x10 <sup>-4</sup>	1.43	3.22	20.4	1670	0.213
	15B	168	39	6.47	800	12.2	1.0x10 <sup>-4</sup>	1.43	3.22	17.0	1400	0.176
	15C	168	32	5.38	700	12.2	1.0x10 <sup>-4</sup>	1.43	3.22	15.5	1270	0.176
	15D	168	31	5.21	500	12.2	1.0x10 <sup>-4</sup>	1.43	3.22	15.0	1230	0.170
	15E	168	35	5.88	500	12.2	1.0x10 <sup>-4</sup>	1.43	3.22	14.4	1180	0.139
	15F	168	33	5.46	400	12.2	1.0x10 <sup>-4</sup>	1.43	3.22	13.0	1070	0.122
	15G	168	32	5.38	400	12.2	1.0x10 <sup>-4</sup>	1.43	3.22	12.0	980	0.105
	27A	355	38	13.50	800	8.3	0.8x10 <sup>-4</sup>	1.68	4.01	26.4	3180	0.299
	27B	350	38	13.30	800	8.3	0.5x10 <sup>-4</sup>	1.68	4.01	26.4	3180	0.303
	1	300	59	17.7	1200	39.5	2.4x10 <sup>-4</sup>	1.52	1.97	52.4	1315	0.185
	3	350	58	19.9	1200	31.7	2.8x10 <sup>-4</sup>	1.80	1.80	61.6	1940	0.285
704	4	348	58	20.0	1200	29.0	2.8x10 <sup>-4</sup>	1.75	1.80	61.4	2120	0.312
	5	400	53	21.2	1200	29.0	1.4x10 <sup>-4</sup>	1.85	2.01	66.0	2280	0.340
	6	400	56	22.2	1200	19.65	0.7x10 <sup>-4</sup>	2.02	2.09	62.6	3190	0.432
	7	400	56	22.3	1200	19.65	0.5x10 <sup>-4</sup>	1.92	1.99	67.2	3420	0.495
	4	300	37	11.10	800	19.65	0.9x10 <sup>-4</sup>	2.47	3.93	33.85	1722	0.185
	6	300	29	8.70	1200	19.65	2.0x10 <sup>-4</sup>	2.35	3.12	45.00	2290	0.325
	7	300	27	8.10	1200	19.35	1.8x10 <sup>-4</sup>	2.25	2.46	46.91	2420	0.350
705												

5090-Phase II Final

Thrustor Model:  
IAJ-AF-CG-1  
Propellant:  
Lithium/Nitrogen  
Test Chamber:  
6" x 6"

Thrustor Model:  
AF-CG-1B  
Propellant:  
Lithium/Nitrogen  
Test Chamber:  
6" x 6"



TABLE II TEST RESULTS (contd)

Run No.	Point No.	$I_A$ amps	$V_A$ volts	$P_A$ kW	$I_C$ amps	$\dot{m}$ mg/sec	$P_t$ torr	$P_{ca}$ kW	$P_{an}$ kW	$T$ grams	$I_{sp}$ sec	$\eta_b$ —
705	8	300	25	7.50	1200	19.35	$1.8 \times 10^{-4}$	2.33	2.34	45.61	2360	0.339
	9	350	26	9.10	1200	19.35	$1.5 \times 10^{-4}$	2.30	2.72	44.77	2310	0.345
	10	350	28	9.80	1200	19.05	$1.2 \times 10^{-4}$	2.60	3.36	44.30	2320	0.316
	11	350	33	11.55	1200	12.3	$0.6 \times 10^{-4}$	3.02	4.04	38.70	3145	0.343
	12A	350	36	12.60	1200	12.5	$1.8 \times 10^{-4}$	3.51	4.20	40.1	3200	0.342
	12B	350	36	12.60	1200	12.5	$1.8 \times 10^{-4}$	3.51	4.20	39.8	3180	—
	13	350	35	12.25	1200	12.5	$2.8 \times 10^{-4}$	—	—	43.6	3480	—
	14	350	36	12.60	1200	12.5	$4.0 \times 10^{-4}$	—	—	47.4	3792	—
	15	350	36	12.60	1200	12.5	$5.0 \times 10^{-4}$	—	—	49.8	3984	—
	16	350	34	11.90	1200	12.5	$5.6 \times 10^{-4}$	—	—	48.6	3888	—
	17	350	33	11.55	1200	12.5	$6.4 \times 10^{-4}$	—	—	51.1	4088	—
	18	350	32	11.20	1200	12.5	—	—	—	52.4	4192	—
	19	350	31	10.85	1200	12.5	—	—	—	54.9	4392	—
	20	350	28	9.80	1200	12.5	—	—	—	60.5	4840	—
	22	350	25	8.75	1200	12.5	—	—	—	69.9	5592	—
	23	350	17	5.95	1200	12.5	—	—	—	63.6	5088	—
	24	350	19	6.65	1200	12.5	—	—	—	63.0	5040	—
	25	350	30	10.50	1200	10.3	—	3.34	3.80	35.8	3480	0.374
	26	350	34	11.90	1200	10.3	$4.4 \times 10^{-5}$	3.64	4.08	39.0	3780	0.378
	27	350	40	14.00	1200	10.3	$4.2 \times 10^{-5}$	3.66	4.00	39.6	3840	0.396
	28	400	38	15.20	1200	10.3	$5.8 \times 10^{-5}$	4.50	4.80	38.6	3750	0.334

TABLE II TEST RESULTS (contd)

Run No.	Point No.	I <sub>A</sub> amps	V <sub>A</sub> volts	P <sub>A</sub> kW	I <sub>C</sub> amps	$\dot{m}$ mg/sec	P <sub>t</sub> torr	P <sub>ca</sub> kW	P <sub>an</sub> kW	T grams	I <sub>sp</sub> sec	$\eta_b$ —
705	29	400	34	13.60	1000	10.3	$3.0 \times 10^{-5}$	4.28	4.85	38.8	3760	0.370
	30	400	28	11.20	800	10.3	$2.0 \times 10^{-5}$	4.55	3.09	35.2	3420	0.340
	31	400	22	8.80	600	10.3	$2.0 \times 10^{-5}$	3.83	2.60	30.2	2420	0.244
707												
	2	136	93	12.6	1200	20.5	$5.4 \times 10^{-4}$	2.72	2.42	40.9	2000	0.318
	3	220	86	18.9	1200	20.5	$3.6 \times 10^{-4}$	3.08	3.25	40.8	1990	0.210
	4	220	97.5	21.5	1200	14.5	$0.8 \times 10^{-4}$	3.60	3.57	47.1	3250	0.349
	5	240	100	24.0	1200	14.5	$0.8 \times 10^{-4}$	3.95	3.85	55.6	3830	0.435
	6	250	102	25.5	1200	14.5	$0.5 \times 10^{-4}$	3.76	4.22	60.0	4140	0.477
	7	250	107	26.8	1200	11.45	$1.1 \times 10^{-4}$	2.96	2.63	62.0	5410	0.613
	8	250	102	25.5	1200	11.45	$1.5 \times 10^{-4}$	—	—	66.5	5810	0.742
	9	258	100	25.8	1200	11.45	$2.4 \times 10^{-4}$	—	—	67.1	5860	0.747
	10	256	102	26.1	1200	11.45	$2.9 \times 10^{-4}$	—	—	60.5	5280	0.600
	11	258	94	24.3	1200	11.45	$3.6 \times 10^{-4}$	—	—	56.6	4940	0.564
	12	254	92	23.4	1200	11.8	$5.0 \times 10^{-4}$	—	—	55.6	4710	0.548
	13	250	98	24.5	1200	11.45	$2.0 \times 10^{-4}$	—	—	57.0	4980	0.568
	14	252	92	23.2	1200	11.45	$1.0 \times 10^{-4}$	2.88	2.88	59.7	5210	0.657
	15	250	102	25.5	1200	11.45	$1.0 \times 10^{-4}$	3.49	3.49	60.4	5280	0.613
	16	195	93.0	18.1	1200	11.45	$1.2 \times 10^{-4}$	2.64	2.64	46.5	4060	0.511
	17	204	82.5	16.8	1200	11.45	$1.3 \times 10^{-4}$	2.36	2.36	46.4	4050	0.548

Thruster Model: CG-1C

Propellant: Li/N<sub>2</sub> pts. 2-6, Li/H<sub>2</sub> pts. 7-17

Test Chamber: 6' x 6'

TABLE II TESTS RESULTS (contd)

Run No.	Point No.	I <sub>A</sub> amps	V <sub>A</sub> volts	P <sub>A</sub> kW	I <sub>C</sub> amps	$\dot{m}$ mg/sec	P <sub>t</sub> torr	P <sub>ca</sub> kW	P <sub>an</sub> kW	T grams	I <sub>sp</sub> sec	$\eta_b$
708	1	104	86.5	9.0	1200	38.5	—	1.85	3.05	—	—	—
	2	241	90	21.4	1200	11.84	$3 \times 10^{-4}$	2.40	1.89	—	—	—
	3	252	62.5	15.8	400	11.36	$2 \times 10^{-4}$	2.43	2.08	35.3	3100	0.332
	4	280	72	20.2	500	11.36	$1.4 \times 10^{-4}$	2.62	2.72	45.9	4040	0.441
	5	280	80	22.4	600	11.36	$1.2 \times 10^{-4}$	2.80	2.49	50.7	4460	0.485
	6	280	72	20.4	600	11.36	$0.9 \times 10^{-4}$	2.53	2.71	50.8	4470	0.534
	7	280	74	20.7	600	11.36	$1.0 \times 10^{-4}$	2.72	2.77	50.7	4460	0.524
	8	280	72.5	20.5	600	11.36	$1.0 \times 10^{-4}$	2.57	2.64	51.2	4510	0.541
	9	280	75	21.0	600	11.36	$1.0 \times 10^{-4}$	2.61	2.64	50.3	4430	0.509
	10	279	75	20.9	600	11.36	$1.0 \times 10^{-4}$	2.66	2.64	47.6	4190	0.458
	11	279	75	20.9	600	11.36	$0.9 \times 10^{-4}$	2.50	2.54	46.1	4060	0.430
	12	282	78	22.0	600	11.36	$1.0 \times 10^{-4}$	2.77	2.92	51.6	4540	0.511
	13	282	74	20.9	600	11.36	$0.9 \times 10^{-4}$	2.62	2.72	51.6	4540	0.538
	14	282	75	20.6	600	11.36	$1.2 \times 10^{-4}$	2.57	2.61	51.1	4500	0.536
	15	278	78	21.7	600	11.36	$1.0 \times 10^{-4}$	2.65	2.73	49.8	4380	0.482
	16	280	76	21.3	600	11.36	$1.0 \times 10^{-4}$	2.63	2.63	50.7	4460	0.510
	17	282	75	21.2	600	11.36	$1.2 \times 10^{-4}$	2.61	2.61	49.9	4390	0.496
	18	282	76	21.4	600	11.36	$1.2 \times 10^{-4}$	2.72	2.83	50.4	4440	0.502
	19	282	78	22.0	600	11.30	$1.2 \times 10^{-4}$	2.83	2.99	51.7	4580	0.517
	20	280	82	23.0	600	11.30	$1.2 \times 10^{-4}$	3.02	3.09	50.2	4440	0.465
	21	276	88	24.3	600	11.30	$1.2 \times 10^{-4}$	2.58	2.80	48.1	4260	0.405
	22	280	79	22.1	600	11.30	$0.9 \times 10^{-4}$	2.62	2.82	47.4	4190	0.431

Thrustor Model: CG-1C  
 Propellant: Li/H<sub>2</sub>  
 Test Chamber: 6' x 6'

TABLE II TESTS RESULTS (contd)

Run No.	Point No.	I <sub>A</sub> amps	V <sub>A</sub> volts	P <sub>A</sub> kW	I <sub>C</sub> amps	m <sub>g</sub> /sec	P <sub>t</sub> torr	P <sub>ca</sub> kW	P <sub>an</sub> kW	T grams	I <sub>sp</sub> sec	η <sub>b</sub>
708	23	284	75	21.3	606	11.30	1.0x10 <sup>-4</sup>	2.74	2.92	50.1	4430	0.500
	24	282	77	21.7	600	11.30	1.1x10 <sup>-4</sup>	2.84	3.00	49.6	4390	0.482
	25	280	79	22.1	600	11.30	1.1x10 <sup>-4</sup>	2.98	3.05	49.6	4390	0.473
	26	276	84	23.2	500	11.30	1.4x10 <sup>-4</sup>	3.02	2.77	49.6	4390	0.451
	27	282	79	22.3	600	11.30	1.0x10 <sup>-4</sup>	2.65	2.86	48.9	4330	0.456
	28	282	78	22.0	600	11.30	1.2x10 <sup>-4</sup>	2.77	2.90	51.3	4540	0.508
	29	282	76.5	21.6	600	11.30	1.0x10 <sup>-4</sup>	2.77	2.89	51.3	4540	0.518
	30	281	76.5	21.5	600	11.30	1.2x10 <sup>-4</sup>	2.62	2.80	50.9	4500	0.511
	31	282	78.5	22.1	600	11.30	1.1x10 <sup>-4</sup>	3.03	3.09	51.7	4580	0.515
	32	286	73	20.9	600	11.30	2.3x10 <sup>-4</sup>	2.84	3.09	—	—	—
	33	280	70	19.6	600	11.30	2.4x10 <sup>-4</sup>	2.50	2.77	—	—	—
	34	280	68	19.0	600	11.30	4.6x10 <sup>-4</sup>	2.50	3.06	—	—	—
	35	280	69.5	19.5	600	11.30	4.4x10 <sup>-4</sup>	2.43	2.92	40.3	3570	0.354
	1A	300	80	24.0	600	11.45	3.7x10 <sup>-4</sup>	3.42	3.49	41.2	3600	0.165
	1B	300	80	24.0	600	11.45	3.7x10 <sup>-4</sup>	3.42	3.49	43.7	3820	0.186
710	2	300	60	18.0	350	11.45	0.7x10 <sup>-4</sup>	3.05	2.70	45.2	3950	0.350
	3A	300	58	17.4	300	11.45	4.2x10 <sup>-4</sup>	3.05	2.70	40.3	3520	0.310
	3B	300	58	17.4	300	11.45	4.2x10 <sup>-4</sup>	3.05	2.70	38.8	3400	0.287
	4	300	57	17.1	350	11.45	4.8x10 <sup>-4</sup>	2.96	2.53	39.7	3470	0.282

Thrustor Model: AF-CG-1D  
 Propellant: Li/H<sub>2</sub>  
 Test Chamber: 6' x 6'

TABLE II TEST RESULTS (contd)

Run No.	Point No.	I <sub>A</sub> amps	V <sub>A</sub> volts	P <sub>A</sub> kW	m <sup>3</sup> mg/sec	P <sub>t</sub> torr	P <sub>C+B</sub> kW	P <sub>an</sub> kW	P <sub>mag</sub> kW	T grams	I <sub>sp</sub> sec	η <sub>o</sub> —
716	1	200	160	32.00	—	—	1.29	8.85	5.60	—	—	—
	2	350	72	25.20	11.25	3.4x10 <sup>-4</sup>	3.81	3.21	5.56	30.12	2680	0.126
	3	345	59	23.81	10.92	5.0x10 <sup>-5</sup>	3.72	4.29	5.63	40.50	3700	0.244
	4	350	61.5	21.53	11.00	2.6x10 <sup>-5</sup>	3.90	3.69	4.86	41.37	3760	0.233
	5	350	58	20.30	11.00	3x10 <sup>-5</sup>	3.52	2.86	4.92	47.00	4270	0.382
	6	350	59	20.65	11.00	2.4x10 <sup>-5</sup>	3.75	3.03	4.86	46.50	4220	0.295
	7	375	58.5	21.94	11.12	3x10 <sup>-5</sup>	4.21	3.27	4.86	39.62	3560	0.253
	8	400	57.5	23.00	11.12	3x10 <sup>-5</sup>	4.27	3.52	4.58	42.50	3820	0.282
	9	400	57	22.80	11.12	2.4x10 <sup>-5</sup>	4.26	3.42	4.58	43.50	3910	0.298
	10	400	56	22.40	11.12	2.4x10 <sup>-5</sup>	3.82	2.98	4.58	50.75	4560	0.411
	11	400	58	23.20	11.12	2.4x10 <sup>-5</sup>	4.29	3.45	4.55	50.62	4550	0.271
	12	395	58	22.91	11.12	2.4x10 <sup>-5</sup>	4.34	3.50	4.55	46.00	4130	0.290
	13	395	56	22.12	11.12	2.2x10 <sup>-5</sup>	4.25	3.32	4.52	52.75	4740	0.450
	14	395	56	22.12	11.12	2.4x10 <sup>-5</sup>	3.98	2.86	4.50	51.75	4650	0.384
	15	395	56	22.12	11.12	2.6x10 <sup>-5</sup>	4.21	2.98	4.42	41.37	3720	0.278
	16	395	58.5	23.11	11.12	2.2x10 <sup>-5</sup>	4.37	3.53	4.52	42.00	3770	0.275
	17	420	56.5	23.73	11.12	2.8x10 <sup>-5</sup>	4.66	4.03	4.42	41.75	3750	0.267
	18	375	55	20.63	11.12	1.8x10 <sup>-5</sup>	3.63	3.07	4.55	49.25	4420	0.415
	19	350	57.5	20.13	11.12	2.3x10 <sup>-5</sup>	3.07	2.66	4.58	38.25	3440	0.256
	20	350	58	20.30	11.12	2.7x10 <sup>-5</sup>	3.20	2.76	4.72	43.87	3940	0.332
	21	350	58	20.30	11.12	2.3x10 <sup>-5</sup>	3.23	2.78	4.72	44.00	3950	0.334

TABLE II TEST RESULTS (contd)

Run No.	Point No.	I <sub>A</sub> amps	V <sub>A</sub> volts	P <sub>A</sub> kW	m <sub>g</sub> /sec	P <sub>t</sub> torr	P <sub>C+B</sub> kW	P <sub>an</sub> kW	P <sub>mag</sub> kW	T grams	I <sub>sp</sub> sec	η <sub>o</sub> —
716	22	350	58	20.30	11.12	2.5x10 <sup>-5</sup>	3.22	2.78	4.86	44.12	3960	0.333
	23	325	58	18.85	11.12	2.6x10 <sup>-5</sup>	3.13	2.69	4.92	39.62	3560	0.285
	24	300	61	18.30	11.12	3.4x10 <sup>-5</sup>	3.04	2.65	4.92	38.25	3440	0.272
718	1	350	63	22.05	7.91	1.0x10 <sup>-4</sup>	3.68	4.86	4.86	31.87	4029	0.229
	2	350	63.5	22.23	6.86	7.2x10 <sup>-5</sup>	3.89	5.00	4.86	32.75	4774	0.277
	3	350	63	22.05	6.86	6.2x10 <sup>-5</sup>	3.93	4.88	4.86	31.87	4645	0.264
	4	350	63	22.05	5.74	3.8x10 <sup>-5</sup>	4.01	4.85	4.86	32.50	5662	0.328
	5	350	63	22.05	5.74	3.5x10 <sup>-5</sup>	4.01	4.90	4.86	32.37	5639	0.325
	6	350	63	22.05	4.63	3.1x10 <sup>-5</sup>	4.05	4.96	4.86	32.25	6965	0.400
	7	350	64	22.40	4.63	3.4x10 <sup>-5</sup>	4.24	5.14	4.86	32.12	6937	0.392
	8	350	64	22.40	4.63	3.2x10 <sup>-5</sup>	4.37	5.14	4.86	32.37	6991	0.398
	9	350	64	22.40	4.63	3.0x10 <sup>-5</sup>	4.51	5.15	4.86	32.00	6911	0.390
	10	350	64	22.40	4.50	3.0x10 <sup>-5</sup>	4.60	5.15	4.86	31.87	7082	0.397
	11	350	64	22.40	4.50	2.8x10 <sup>-5</sup>	4.72	5.14	4.86	31.50	7000	0.388
	12	350	64	22.40	4.50	2.9x10 <sup>-5</sup>	4.89	5.13	4.86	30.50	6777	0.364
720	1A	202	77.5	15.66	—	—	0.97	5.31	10.75	—	—	—
	1B	202	77.5	15.66	—	—	0.97	5.31	10.75	—	—	—
	2A	299	60.0	17.94	11.10	2.0x10 <sup>-4</sup>	2.87	3.76	4.57	29.87	2690	0.173
	2B	299	60.0	17.94	9.14	2.0x10 <sup>-4</sup>	2.87	3.76	4.57	37.37	4080	0.325
	3	350	60.0	21.00	6.83	3.6x10 <sup>-4</sup>	3.43	3.47	4.62	41.87	6130	0.480
	4	350	60.0	21.00	6.77	4.0x10 <sup>-5</sup>	3.61	3.99	4.62	39.50	5830	0.431

Thrustor, Model: LAJ-AF-CG  
 Propellant: Li/H<sub>2</sub>  
 Test Chamber: 6' x 14'



TABLE II TEST RESULTS (contd)

Run No.	Point No.	I <sub>A</sub> amps	V <sub>A</sub> volts	P <sub>A</sub> kW	$\dot{m}$ mg/sec	P <sub>C</sub> corr	P <sub>C+B</sub> kW	P <sub>an</sub> kW	P <sub>mag</sub> kW	T grams	I <sub>sp</sub> sec	$\eta_b$ —
720	5A	350	60.0	21.00	6.77	$4.2 \times 10^{-5}$	3.61	4.07	4.71	37.00	5465	0.378
	5B	350	60.0	21.00	6.77	$4.2 \times 10^{-5}$	3.61	4.07	4.71	36.37	5372	0.365
	6	350	58.0	20.30	6.77	$2.2 \times 10^{-5}$	3.61	3.97	4.62	36.37	5372	0.376
	7	350	58.0	20.30	5.74	$3.5 \times 10^{-5}$	3.65	4.15	4.62	34.37	5076	0.336
	8	350	58.0	20.30	5.74	$3.5 \times 10^{-5}$	3.65	4.22	4.57	33.75	4985	0.325
	9	350	58.0	20.30	5.74	$3.4 \times 10^{-5}$	3.74	4.27	4.60	32.12	4744	0.294
	10	350	58.0	20.30	5.74	$3.3 \times 10^{-5}$	3.76	4.27	4.60	32.12	4892	0.312
	11	350	58.0	20.30	5.74	$3.2 \times 10^{-5}$	3.80	4.26	4.60	32.12	4892	0.312
	12	350	58.0	20.30	5.70	$3.1 \times 10^{-5}$	3.83	4.26	4.60	33.12	5810	0.371
	13	350	58.0	20.30	5.70	$3.1 \times 10^{-5}$	3.87	4.24	4.60	33.12	5810	0.371
	14	350	58.0	20.30	5.70	$2.9 \times 10^{-5}$	3.93	4.20	4.60	32.25	5657	0.352
	15	350	57.5	20.13	5.70	$2.8 \times 10^{-5}$	3.88	4.10	4.66	31.87	5591	0.345
	16A	350	57.0	19.95	5.70	$2.8 \times 10^{-5}$	3.90	4.05	4.50	26.87	4714	0.248
	16B	350	57.0	19.95	5.70	$2.8 \times 10^{-5}$	3.90	4.05	4.50	29.37	5152	0.297
	17	350	58.0	20.30	5.70	$3.0 \times 10^{-5}$	4.22	4.09	4.47	31.25	5482	0.332
	18A	350	59.0	20.65	5.78	$4.2 \times 10^{-5}$	4.31	4.04	4.44	32.50	5622	0.349
	18B	350	59.0	20.65	5.78	$4.2 \times 10^{-5}$	4.20	4.04	4.44	34.87	6032	0.402
	19	350	60.0	21.00	5.78	$4.0 \times 10^{-5}$	4.20	4.05	4.92	34.00	5882	0.370
	20	350	60.0	21.00	5.78	$4.1 \times 10^{-5}$	4.20	4.10	4.92	34.37	5944	0.378
	21	345	60.0	21.00	5.78	$4.8 \times 10^{-5}$	4.18	4.06	4.86	34.12	5903	0.374
	22	345	60.0	21.00	5.78	$3.9 \times 10^{-5}$	4.25	4.06	4.83	34.00	5882	0.372

TABLE II TEST RESULTS (contd)

Run No.	Point No.	I <sub>A</sub> amps	V <sub>A</sub> volts	P <sub>A</sub> kW	$\dot{m}$ mg/sec	P <sub>t</sub> torr	P <sub>C+B</sub> kW	P <sub>an</sub> kW	P <sub>mag</sub> kW	T grams	I <sub>sp</sub> sec	$\tau_o$ —
720	23A	345	58.5	20.18	5.78	$3.8 \times 10^{-5}$	4.09	3.84	4.80	35.00	6055	0.407
	23B	345	58.5	20.18	5.78	$3.8 \times 10^{-5}$	4.09	3.84	4.80	34.37	5944	0.392
	24	345	59.0	20.36	5.78	$4.1 \times 10^{-5}$	4.02	4.00	4.80	32.75	5666	0.354
	25A	345	60.0	20.70	5.78	$5.5 \times 10^{-5}$	4.14	4.50	4.80	30.62	5297	0.305
	25B	345	60.0	20.70	5.78	$5.5 \times 10^{-5}$	4.14	4.50	4.80	29.37	5081	0.280
	26A	345	61.0	21.05	5.78	$4.5 \times 10^{-5}$	4.01	4.40	4.77	22.50	5622	0.339
	26B	345	61.0	21.05	5.78	$4.5 \times 10^{-5}$	4.01	4.40	4.77	35.62	6162	0.408
	27	345	54.0	18.73	5.78	$3.4 \times 10^{-5}$	4.20	3.84	4.74	35.00	6055	0.433
	28A	345	56.0	19.32	5.78	$3.6 \times 10^{-5}$	4.25	3.68	4.05	35.62	6162	0.438
	28B	345	56.0	19.32	5.78	$3.6 \times 10^{-5}$	4.25	3.68	3.90	33.75	5839	0.393
	29A	345	57.0	19.66	5.78	$3.8 \times 10^{-5}$	4.12	3.84	3.87	33.37	5773	0.378
	29B	345	57.0	19.66	5.78	$3.8 \times 10^{-5}$	4.12	3.84	4.05	35.62	6162	0.430
	30	345	55.5	19.15	5.78	$3.4 \times 10^{-5}$	4.28	3.86	4.05	35.62	6162	0.440
	31	345	56.5	19.49	5.78	$4.6 \times 10^{-5}$	4.17	3.74	3.85	35.62	6162	0.435
	32A	345	57.5	19.83	5.78	$4.5 \times 10^{-5}$	4.17	4.00	3.90	36.25	6271	0.444
	32B	345	57.5	19.83	5.78	$4.5 \times 10^{-5}$	4.00	4.17	4.00	35.00	6055	0.414
	33	345	56.5	19.49	5.78	$3.4 \times 10^{-5}$	3.62	4.17	3.92	34.00	5882	0.396
	34	345	57.5	19.83	5.78	$3.8 \times 10^{-5}$	3.91	4.17	3.81	32.62	5643	0.359
	35	345	57.0	19.66	5.78	$3.6 \times 10^{-5}$	3.83	4.23	3.92	34.00	5882	0.395
	36	345	58.0	20.01	5.78	$3.7 \times 10^{-5}$	3.92	4.21	3.88	33.50	5795	0.376
	37	345	56.0	19.32	5.78	$3.4 \times 10^{-5}$	3.74	4.1	3.92	33.50	5795	0.387
	38	345	58.5	20.18	5.78	$4.1 \times 10^{-5}$	3.85	4.21	3.85	32.62	5626	0.355

TABLE II TEST RESULTS (contd)

Run No.	Point No.	I <sub>A</sub> amps	V <sub>A</sub> volts	P <sub>A</sub> kW	ḡ mg/sec	P <sub>t</sub> torr	P <sub>C+B</sub> kW	P <sub>an</sub> kW	P <sub>mag</sub> kW	T grams	I <sub>sp</sub> sec	η <sub>b</sub>
720	39	345	57.0	19.66	5.78	4.0x10 <sup>-5</sup>	3.94	4.15	3.90	33.25	5752	0.377
	40	345	58.0	20.01	5.78	4.0x10 <sup>-5</sup>	3.92	4.19	3.87	32.87	5687	0.363
	41A	348	53.0	18.44	5.80	3.4x10 <sup>-5</sup>	4.21	4.32	3.75	31.37	5408	0.350
	41B	348	53.0	18.44	5.80	3.4x10 <sup>-5</sup>	4.21	4.32	3.66	28.75	4956	0.294
	42	345	58.0	20.01	5.80	3.6x10 <sup>-5</sup>	3.96	4.54	3.51	28.37	4891	0.268
	43	342	56.0	19.15	5.80	4.1x10 <sup>-5</sup>	4.36	4.32	3.61	29.62	5106	0.308
	44	351	56.0	19.66	5.80	3.5x10 <sup>-5</sup>	4.21	4.41	3.65	30.12	5193	0.305
	45	350	57.0	19.95	5.83	3.5x10 <sup>-5</sup>	4.37	4.08	4.80	31.12	5337	0.322
	46	350	57.0	19.95	5.83	3.4x10 <sup>-5</sup>	4.39	3.99	4.80	31.87	5466	0.338
	47	350	55.5	19.43	5.83	3.4x10 <sup>-5</sup>	4.39	3.91	4.90	32.00	5488	0.346
721	48	351	56.0	19.66	5.83	3.3x10 <sup>-5</sup>	4.37	3.83	4.96	30.75	5274	0.316
	49	301	61.0	18.36	—	—	2.09	7.26	5.05	—	—	—
	50	200	80.5	16.10	—	—	1.46	7.15	10.56	—	—	—
	1	350	51.0	17.85	5.73	5.4x10 <sup>-5</sup>	4.55	3.42	4.83	30.00	5235	0.332
	2	355	49.0	17.40	5.73	2.8x10 <sup>-4</sup>	8.58	5.02	4.80	10.87	1897	—
	3	355	53.0	18.82	5.68	4.9x10 <sup>-5</sup>	4.87	3.85	4.77	28.37	4995	0.346
	4	350	55.0	19.25	5.73	5.4x10 <sup>-5</sup>	4.83	4.01	4.65	28.12	4908	0.276
	5	348	56.0	19.49	5.73	4.8x10 <sup>-5</sup>	4.90	4.40	4.65	28.37	4951	0.279
	6	355	57.0	20.24	5.73	4.7x10 <sup>-5</sup>	5.24	4.60	4.89	30.50	5323	0.309
	7	355	57.0	20.24	5.73	5.2x10 <sup>-5</sup>	5.56	4.82	4.92	30.37	5300	0.307
	8	355	57.0	20.24	6.76	4.4x10 <sup>-5</sup>	5.65	4.89	4.89	30.75	5489	0.322
	9	351	59.0	20.71	5.73	4.7x10 <sup>-5</sup>	6.03	5.03	4.89	30.12	5257	0.296

TABLE II TEST RESULTS (contd.)

Run No.	Point No.	I <sub>A</sub> amps	V <sub>A</sub> volts	P <sub>A</sub> kW	$\dot{m}$ mg/sec	P <sub>t</sub> torr	P <sub>C+B</sub> kW	P <sub>an</sub> kW	P <sub>mag</sub> kW	T grams	I <sub>sp</sub> sec	$\eta_b$
721	10	351	55.0	19.31	5.73	$4.0 \times 10^{-5}$	4.96	4.64	4.82	29.50	5148	0.301
	11	355	53.0	18.82	5.73	$3.6 \times 10^{-5}$	4.87	4.23	4.83	30.25	5279	0.324
	12A	351	54.0	18.95	5.73	$3.4 \times 10^{-5}$	4.92	4.01	4.83	29.37	5126	0.304
	12B	351	54.0	18.95	5.73	$3.4 \times 10^{-5}$	4.92	4.01	4.83	28.75	5017	0.291
	13	351	58.0	20.35	5.73	$3.8 \times 10^{-5}$	5.41	4.61	4.79	27.25	4756	0.247
	14	350	59.0	20.63	5.73	$4.0 \times 10^{-5}$	5.70	4.63	4.70	25.25	4407	0.210
	15A	355	50.0	17.75	5.73	$7.0 \times 10^{-5}$	6.23	3.86	4.70	22.12	3860	0.182
	15B	355	50.0	17.75	5.73	$7.0 \times 10^{-5}$	6.23	3.86	4.70	20.25	3534	0.153
	16A	355	50.0	17.75	5.73	$5.7 \times 10^{-5}$	6.16	3.53	4.70	23.87	4166	0.212
	16B	355	50.0	17.75	5.73	$5.7 \times 10^{-5}$	6.16	3.53	4.70	22.87	3991	0.195
	17	355	51.5	18.30	5.73	$5.8 \times 10^{-5}$	6.21	3.83	4.70	21.50	3752	0.168
	18	355	51.5	18.30	5.73	$7.0 \times 10^{-5}$	6.18	3.74	4.74	22.25	3883	0.180
	19A	355	51.5	18.30	5.73	$5.5 \times 10^{-5}$	6.16	3.72	4.66	23.87	4166	0.207
	19B	355	51.5	18.30	5.73	$5.5 \times 10^{-5}$	6.16	3.72	4.66	22.25	3883	0.181
	20	355	50.5	17.90	5.73	$4.4 \times 10^{-5}$	5.98	3.64	4.66	23.75	4145	0.209
	21A	360	33.0	11.90	5.73	$1.2 \times 10^{-5}$	5.41	2.23	4.55	33.87	5911	0.489
	21B	360	33.0	11.90	5.73	$1.2 \times 10^{-5}$	5.41	2.23	4.55	28.87	5038	0.356
	22	360	48.0	17.27	—	—	—	—	4.66	—	—	—
	23	350	59.0	20.63	—	—	—	—	4.87	—	—	—

TABLE II TEST RESULTS (contd)

Run No.	Point No.	I <sub>A</sub> amps	V <sub>A</sub> volts	P <sub>A</sub> kW	$\dot{m}$ mg/sec	P <sub>t</sub> torr	P <sub>C+B</sub> kW	P <sub>an</sub> kW	P <sub>mag</sub> kW	T grams	I <sub>sp</sub> sec	$\eta_b$ —
722	1	134	121	16.21	36.7	—	1.04	5.64	19.26	32.62	888	0.039
	2	136	112	15.23	38.6	—	1.16	6.60	14.66	29.50	764	0.036
	3	138	102	14.08	38.4	—	1.19	6.36	8.91	29.50	768	0.047
	4	202	96.5	19.49	37.3	—	1.50	8.27	8.76	28.75	771	0.037
	5	172	99.0	17.03	37.1	—	1.39	7.62	8.91	31.50	849	0.049
	6	172	99.0	17.03	37.1	—	1.40	7.62	8.91	30.12	812	0.045
723	1	119	109.0	12.20	34.10	—	1.15	4.77	8.91	22.00	645	0.032
	2	200	100.0	20.00	33.80	—	1.51	7.90	8.91	27.87	824	0.038
	3	200	97.0	19.40	33.50	—	1.51	8.23	8.91	26.75	798	0.036
	4	200	97.0	19.40	33.30	—	1.48	8.24	8.91	26.50	795	0.035
	5	200	97.0	19.40	32.20	—	1.50	8.40	8.91	26.12	811	0.035
	6	200	97.0	19.40	32.00	—	1.52	8.40	8.91	26.00	812	0.035
	7A	250	77.0	19.25	6.82	$1.2 \times 10^{-4}$	3.87	3.55	8.80	30.12	4416	0.227
	7B	250	77.0	19.25	6.82	$1.2 \times 10^{-4}$	3.87	3.55	8.80	31.37	4600	0.246
	8A	250	77.0	19.25	6.82	$1.2 \times 10^{-4}$	3.74	3.54	8.80	28.87	4231	0.208
	8B	250	77.0	19.25	6.82	$1.2 \times 10^{-4}$	3.74	3.54	8.80	30.75	4508	0.237
	9	300	71.0	21.30	6.82	$5.0 \times 10^{-5}$	3.87	3.49	8.72	45.37	6652	0.482
	10	300	70.0	21.00	6.82	$4.5 \times 10^{-5}$	4.19	3.53	8.64	45.37	6652	0.488
	11	300	69.0	20.70	6.82	$4.3 \times 10^{-5}$	4.29	3.53	8.49	45.37	6652	0.496
	12	300	69.0	20.70	6.82	$4.0 \times 10^{-5}$	4.32	3.39	8.42	43.87	6433	0.465
	13	300	69.5	20.85	6.82	$4.0 \times 10^{-5}$	4.39	3.41	8.45	44.00	6452	0.465

TABLE II TEST RESULTS (contd)

Run No.	Point No.	I <sub>A</sub> amps	V <sub>A</sub> volts	P <sub>A</sub> kW	$\dot{m}$ mg/sec	P <sub>t</sub> torr	P <sub>C+B</sub> kW	P <sub>an</sub> kW	P <sub>mag</sub> kW	T grams	I <sub>sp</sub> sec	$\eta_b$ —
723	14A	300	68.0	20.40	6.82	$3.8 \times 10^{-5}$	4.44	3.26	8.35	45.12	6617	0.498
	14B	300	68.0	20.40	6.82	$3.8 \times 10^{-5}$	4.44	3.26	8.35	45.75	6708	0.512
	15A	300	68.0	20.40	6.82	$3.2 \times 10^{-5}$	4.50	3.10	8.35	45.87	6726	0.515
	15B	300	68.0	20.40	6.82	$3.2 \times 10^{-5}$	4.50	3.10	8.35	43.87	6433	0.471
	16	300	68.0	20.40	6.82	$4.2 \times 10^{-5}$	4.55	3.29	8.35	42.62	6249	0.444
	17	298	70.0	20.86	6.82	$2.7 \times 10^{-5}$	4.58	3.14	8.35	42.50	6232	0.435
	18A	300	69.0	20.70	6.82	$4.1 \times 10^{-5}$	4.62	3.45	8.35	42.00	6158	0.427
	18B	300	69.0	20.70	6.82	$4.1 \times 10^{-5}$	4.62	3.45	8.35	44.50	6525	0.479
	19A	300	68.0	20.40	6.82	$3.9 \times 10^{-5}$	4.59	3.24	8.35	42.00	6158	0.431
	19B	300	68.0	20.40	6.82	$3.9 \times 10^{-5}$	4.59	3.24	8.35	41.37	6066	0.418
	20	300	68.0	20.40	6.82	$4.2 \times 10^{-5}$	4.64	3.36	8.35	41.37	6066	0.418
	21	300	62.0	18.60	6.82	$8.4 \times 10^{-6}$	3.50	2.79	8.35	54.30	7991	0.775
	22	300	69.0	20.70	6.82	$2.8 \times 10^{-5}$	4.64	3.42	8.35	40.75	5975	0.402
	23A	300	67.0	20.10	6.82	$3.8 \times 10^{-5}$	4.61	3.42	8.35	41.37	6066	0.423
	23B	300	67.0	20.10	6.82	$3.8 \times 10^{-5}$	4.61	3.42	8.35	51.37	7532	0.652
	24A	300	63.0	18.90	6.82	$2.0 \times 10^{-5}$	4.36	2.58	8.35	46.37	6799	0.555
	24B	300	63.0	18.90	6.82	$2.0 \times 10^{-5}$	4.36	2.58	8.35	37.62	5516	0.365
	25	300	68.0	20.40	6.82	$3.6 \times 10^{-5}$	4.61	3.43	8.35	39.50	5792	0.381
	26A	303	62.0	18.78	6.82	$1.4 \times 10^{-5}$	3.99	2.92	8.35	49.50	7258	0.635
	26B	303	62.0	18.78	6.82	$1.4 \times 10^{-5}$	3.99	2.92	8.35	46.37	6799	0.557
	27	300	69.0	20.70	6.82	$3.4 \times 10^{-5}$	4.58	3.29	8.35	37.62	5516	0.342
	28	300	54.0	19.20	6.82	$2.8 \times 10^{-5}$	4.40	3.22	8.35	40.75	5975	0.424



TABLE II TEST RESULTS (cont'd)

Run No.	Point No.	I <sub>A</sub> amps	V <sub>A</sub> volts	P <sub>A</sub> kW	h mg/sec	P <sub>t</sub> torr	P <sub>C+B</sub> kW	P <sub>an</sub> kW	P <sub>mag</sub> kW	T grams	I <sub>sp</sub> sec	η <sub>b</sub> —
723	29	302	62.0	18.72	6.82	1.4x10 <sup>-5</sup>	3.92	2.87	8.35	48.87	7166	0.620
	30	300	69.0	20.70	6.82	3.5x10 <sup>-5</sup>	4.48	3.22	8.35	50.12	7349	0.608
	31	300	66.0	19.80	6.82	3.4x10 <sup>-5</sup>	4.61	3.31	8.35	38.87	5699	0.377
	38	300	69.0	20.70	6.82	2.8x10 <sup>-5</sup>	4.41	3.30	8.76	41.12	6029	0.403
	39	302	69.0	20.84	6.82	2.3x10 <sup>-5</sup>	4.62	3.43	8.80	41.25	6048	0.404
	40	302	67.0	20.23	6.82	3.4x10 <sup>-5</sup>	4.61	3.38	8.80	42.12	6176	0.430
	41A	304	63.0	19.15	6.82	1.6x10 <sup>-5</sup>	4.00	2.79	8.80	49.25	7221	0.610
	41B	304	63.0	19.15	6.82	1.6x10 <sup>-5</sup>	4.00	2.79	8.80	40.50	5938	0.412
	42	303	66.0	19.99	6.82	3.2x10 <sup>-5</sup>	4.66	3.32	8.80	42.37	6213	0.438
	43	304	63.0	19.15	6.82	1.8x10 <sup>-5</sup>	4.35	2.79	8.80	44.25	6488	0.492
	44A	304	64.0	19.46	6.82	2.0x10 <sup>-5</sup>	4.41	2.66	8.80	44.25	6488	0.487
	44B	304	64.0	19.46	6.82	2.0x10 <sup>-5</sup>	4.41	2.66	8.80	41.12	6029	0.421
	45	304	67.0	20.37	6.82	3.4x10 <sup>-5</sup>	4.65	3.44	8.80	41.75	6128	0.421
	46A	305	62.0	18.91	6.82	3.2x10 <sup>-5</sup>	4.10	2.55	8.80	47.37	6946	0.569
	46B	305	62.0	18.91	6.82	3.2x10 <sup>-5</sup>	4.10	2.55	8.80	40.50	5938	0.416
	47	300	70.0	21.00	6.82	3.2x10 <sup>-5</sup>	4.57	3.62	8.80	40.75	5975	0.392
	48	304	65.0	19.76	6.82	3.0x10 <sup>-5</sup>	4.69	3.21	8.80	44.25	6488	0.482
	49	300	73.0	21.90	6.82	2.4x10 <sup>-5</sup>	4.76	3.60	8.80	40.12	5883	0.368
	50	300	72.0	21.60	6.82	3.3x10 <sup>-5</sup>	4.71	3.81	8.80	40.75	5975	0.384
	51A	304	69.0	20.98	6.82	3.4x10 <sup>-5</sup>	4.66	3.68	8.59	37.00	5425	0.251
	51B	304	69.0	20.98	6.82	3.4x10 <sup>-5</sup>	4.66	3.68	8.59	38.87	5699	0.350
	52	306	64.0	19.58	6.82	1.6x10 <sup>-5</sup>	3.50	2.85	8.59	42.00	6158	0.440

TABLE II TEST RESULTS (contd)

Run No.	Point No.	I <sub>A</sub> amps	V <sub>A</sub> volts	P <sub>A</sub> kW	$\dot{m}$ mg/sec	P <sub>t</sub> torr	P <sub>C+B</sub> kW	P <sub>an</sub> kW	P <sub>mag</sub> kW	T grams	I <sub>sp</sub> sec	$\eta_o$ —
723	53	310	59.0	18.29	6.82	$6.5 \times 10^{-6}$	4.12	2.86	8.59	50.75	7441	0.674
	54	300	79.0	23.70	6.82	$6.2 \times 10^{-5}$	5.25	4.35	8.99	33.50	4912	0.241
	55	300	79.0	23.70	6.82	$5.5 \times 10^{-5}$	5.30	4.59	9.14	33.50	4912	0.240
	56A	304	68.0	20.67	6.82	$4.2 \times 10^{-5}$	4.81	4.44	9.14	37.75	4949	0.300
	56B	304	68.0	20.67	6.82	$4.2 \times 10^{-5}$	4.81	4.44	9.14	29.50	4326	0.205
724	1	200	81.0	16.20	26.0	—	1.37	7.17	8.72	112.3	4310	0.931
	2A	296	76.5	22.64	6.83	$0.5 \times 10^{-4}$	4.90	4.46	8.42	14.00	2052	0.044
	2B	296	76.5	22.64	6.83	$0.5 \times 10^{-4}$	4.90	4.46	8.42	17.12	2506	0.066
	3	300	76.0	22.80	6.82	$1.2 \times 10^{-4}$	4.91	4.51	8.42	17.62	2583	0.069
	4A	300	74.0	22.20	6.82	$7 \times 10^{-4}$	5.14	4.29	8.34	24.50	3592	0.138
	4B	300	74.0	22.20	6.82	$7 \times 10^{-4}$	5.14	4.29	8.34	27.62	4049	0.175
	5	300	71.0	21.30	6.82	$5.8 \times 10^{-4}$	4.94	4.16	8.40	27.62	4049	0.180
	6A	303	60.0	18.18	6.82	$0.9 \times 10^{-4}$	2.86	2.60	8.40	36.37	5332	0.350
	6B	303	60.0	18.18	6.82	$0.9 \times 10^{-4}$	2.86	2.60	8.40	33.87	4966	0.303
	7	300	59.0	17.70	6.82	$1 \times 10^{-5}$	2.88	1.79	8.34	33.25	4875	0.298
	8	292	77.0	22.48	6.82	$2 \times 10^{-5}$	3.89	2.95	8.34	37.62	5516	0.323
	9A	303	68.0	20.60	6.62	$2.6 \times 10^{-5}$	4.89	3.77	8.34	31.37	4599	0.239
	9B	303	68.0	20.60	6.82	$2.6 \times 10^{-5}$	4.89	3.77	8.34	30.12	4416	0.220
	10	300	69.0	20.70	6.82	$3.0 \times 10^{-5}$	4.79	4.02	8.34	30.12	4416	0.219
	11	300	69.0	20.70	6.82	$2.2 \times 10^{-5}$	4.90	4.06	8.80	32.00	4692	0.244
	12	298	70.0	20.86	6.82	$2.2 \times 10^{-5}$	5.11	4.19	8.84	32.62	4782	0.252

Thrustor Model: LAJ-AF-CG2  
 Propellant: Li/H<sub>2</sub>  
 Test Chamber: 6' x 14'

TABLE II TEST RESULTS (contd)

Run No.	Point No.	I <sub>A</sub> amps	V <sub>A</sub> volts	P <sub>A</sub> kW	$\dot{m}$ mg/sec	P <sub>t</sub> torr	P <sub>C+B</sub> kW	P <sub>an</sub> kW	P <sub>mag</sub> kW	T grams	I <sub>sp</sub> sec	$\eta_b$
724	13A	298	66.0	19.66	6.82	$2.5 \times 10^{-5}$	5.10	4.40	8.80	32.62	4782	0.263
	13B	298	66.0	19.66	6.82	$2.5 \times 10^{-5}$	5.10	4.40	8.80	35.75	5241	0.315
	14A	300	68.0	20.40	6.82	$2.5 \times 10^{-5}$	4.82	3.72	8.80	35.75	5241	0.307
	14B	300	68.0	20.40	6.82	$2.5 \times 10^{-5}$	4.82	3.72	8.80	33.87	4966	0.276
	15	298	68.0	20.26	6.82	$2.8 \times 10^{-5}$	4.83	3.93	8.80	32.12	4709	0.249
	16	298	69.0	20.56	6.82	$3.0 \times 10^{-5}$	5.11	4.14	8.80	30.62	4489	0.224
	17	298	71.0	21.15	6.82	$3.8 \times 10^{-5}$	5.45	4.33	8.80	29.62	4343	0.206
	18	298	68.0	20.26	6.82	$4.2 \times 10^{-5}$	5.16	3.87	8.80	30.62	4489	0.227
	19	298	69.5	20.71	6.82	$4.4 \times 10^{-5}$	6.70	3.95	8.80	30.62	4489	0.223
	20	298	69.5	20.71	6.82	$4.4 \times 10^{-5}$	5.23	3.87	8.84	30.62	4489	0.223
	21	298	69.5	20.71	6.82	$4.4 \times 10^{-5}$	5.13	3.89	8.84	30.50	4472	0.221
	22	298	69.5	20.71	6.82	$4.2 \times 10^{-5}$	5.14	3.91	8.88	30.12	4416	0.215
	23	298	69.5	20.71	6.82	$4.4 \times 10^{-5}$	5.18	3.89	8.84	30.62	4489	0.223
	24	298	69.0	20.56	6.82	$4.2 \times 10^{-5}$	5.14	3.83	8.88	30.62	4489	0.224
	25	298	69.0	20.56	6.82	$4.1 \times 10^{-5}$	5.15	3.87	8.88	30.62	4489	0.224
	26	300	69.5	20.85	6.82	$4.1 \times 10^{-5}$	5.14	3.87	8.88	30.62	4489	0.221
	27	300	69.5	20.85	6.82	$4.5 \times 10^{-5}$	5.35	3.96	8.84	30.75	4508	0.223
	28	300	70.0	21.00	6.82	$4.2 \times 10^{-5}$	6.72	3.95	8.96	31.00	4545	0.225
	29A	300	70.0	21.00	6.82	$4.0 \times 10^{-5}$	5.06	3.98	8.92	32.00	4692	0.240
	29B	300	70.0	21.00	6.82	$4.0 \times 10^{-5}$	5.06	3.99	8.92	34.50	5058	0.280

TABLE II TEST RESULTS (contd)

Run No.	Point No.	I <sub>A</sub> amps	V <sub>A</sub> volts	P <sub>A</sub> kW	m mg/sec	P <sub>t</sub> torr	P <sub>C+B</sub> kW	P <sub>an</sub> kW	P <sub>mag</sub> kW	T grams	I <sub>sp</sub> sec	η <sub>b</sub> —
724	30	300	70.0	21.00	6.82	3.8x10 <sup>-5</sup>	5.24	3.93	8.84	35.12	5149	0.305
	31	300	69.5	20.85	6.82	3.6x10 <sup>-5</sup>	5.14	3.83	8.99	34.50	5058	0.289
	32	300	68.0	20.40	6.82	3.2x10 <sup>-5</sup>	5.07	3.66	9.03	34.50	5058	0.293
	33	300	66.5	19.95	6.82	3.0x10 <sup>-5</sup>	5.00	3.60	9.03	32.62	4782	0.258
	34	305	60.0	18.30	6.82	6.4x10 <sup>-6</sup>	4.04	3.95	9.03	43.25	6341	0.481
	35	307	55.5	17.03	6.82	5.5x10 <sup>-6</sup>	3.59	2.22	9.07	43.25	6341	0.504
	36A	308	54.0	16.63	6.82	7.8x10 <sup>-6</sup>	3.46	2.10	9.07	43.25	6341	0.512
	36B	308	54.0	16.63	6.82	7.8x10 <sup>-6</sup>	3.46	2.10	9.07	43.25	6341	0.512

## APPENDIX II

### X-ATRON ANALYSIS

The heating mechanisms of the Hall Current Accelerator, when operated at very low pressures, are very similar to those of the X-ATRON device. In the Hall accelerator, the internal and rotational energies produced are converted to axial kinetic energy by expansion through a magnetic nozzle. Since many of the heating mechanisms may be similar, a recent analysis of the X-ATRON has been included in this Appendix.

The analysis of the heating and confining in X-ATRON-like devices has been a continual effort over the past three years. The conclusion of an earlier analysis was that heating and confining were good but end losses of energy were too large. For this reason attention was placed upon a model which incorporates flow away from the electrodes so that convective cooling prevents back conduction. Early analysis also showed that it is difficult to support potential near the electrodes where the azimuthal rotation is small. Thus it was decided to move the anode away so that there could be a vacuum separation to support potentials near the end. The analysis which follows studies the dense cathode jet and low density anode jet and their interaction, in order to optimize the configuration and find scaling laws for X-ATRON.

#### 1. Approximations and Equations

The analysis of any device as complex as X-ATRON must involve many simplifying approximations in order to get solutions. Some of these approximations can be checked once the analysis is completed to see if the assumptions are consistent with the answers. Others must be checked by experiment. In this section a partial list of the assumptions has been made, together with justification where possible.

- a. The existence of a steady, axially symmetric operation, with anode and cathode jets is assumed. This is based upon past experiments. The stability of this mode of operation at higher currents is as yet unknown.
- b. The cathode jet is a collision-dominated plasma which can be described in terms of averaged properties and transport coefficients. It consists of a fully ionized plasma in which there are only two species, electrons and ions. The Debye distance is small compared to the dimensions of the device, so that



the number density of the two species are equal almost everywhere. The magnetic Reynolds number is small, so that the magnetic fields are almost unaltered by the plasma. It is convenient to use mass velocity and current rather than ion velocity and electron velocity as the variables. We also write mass averaged conservation laws and generalized Ohm's laws rather than ion and electron conservation laws. The equations which were used are shown in Table I. There is no dissociation or recombination. The term  $P_r$  in the energy equation includes conduction and radiation of power.

- c. The anode jet is a nearly collisionless cloud of electrons and ions in an annular volume surrounding the cathode jet. Near the cathode the anode jet is separated from the cathode jet by a vacuum. It is assumed that the volume is neutral and that individual particle motion is described by

$$m \ddot{\mathbf{r}} = e (\bar{\mathbf{E}} + \dot{\mathbf{r}} \times \bar{\mathbf{B}}) \quad (1)$$

where  $\bar{\mathbf{E}}$  and  $\bar{\mathbf{B}}$  are applied electric and magnetic fields.

- d. The applied electric and magnetic fields will be approximated for the purpose of the analysis. The electric field is greatly affected by the presence of the plasma, the magnetic field is not. Space charges will build up within the plasma to cause magnetic field lines to be nearly equipotential. The space charges require negligible percentage difference in the numbers of ions and electrons.

The only thing which can support potential drops along the field is electron collisions with ions, such as will occur in the cathode jet. In the anode jet, it is assumed that the magnetic field lines are equipotentials. Thus the cathode and anode jet are like virtual electrodes for the source and sink of the radial currents.

The applied magnetic field will be nearly axial with a small radial component. Thus to a reasonable degree of accuracy

TABLE I EQUATIONS FOR DENSE PLASMA

Continuity

$$\frac{1}{r} \frac{\partial}{\partial r} (r \rho u) + \frac{\partial}{\partial z} (\rho w) = 0$$

Momentum

$$\frac{\partial p}{\partial r} - \frac{\rho v^2}{r} = J_{\theta} B_z$$

$$\frac{1}{r^2} \frac{\partial}{\partial r} (r^2 \rho u v) + \frac{\partial}{\partial z} (\rho w v) = J_z B_r - J_r B_z$$

$$\frac{1}{r} \frac{\partial}{\partial r} (r \rho u w) + \frac{\partial}{\partial z} (\rho w^2 + p) = - J_{\theta} B_r$$

Enthalpy

$$\frac{1}{r} \frac{\partial}{\partial r} \left[ r \rho u \left( \frac{2\gamma}{\gamma-1} \frac{kT}{m_a} + \frac{v^2 + w^2}{2} \right) \right] + \frac{\partial}{\partial z} \left[ \rho w \left( \frac{2\gamma}{\gamma-1} \frac{kT}{m_a} + \frac{v^2 + w^2}{2} \right) \right] +$$

$$P_r = - J_r \frac{\partial \phi}{\partial r} - J_z \frac{\partial \phi}{\partial z}$$

Continuity

$$\frac{1}{r} \frac{\partial}{\partial r} (r J_r) + \frac{\partial J_z}{\partial z} = 0$$

Ohm's Laws

$$\frac{1}{\sigma} J_r + \frac{J_{\theta} B_z}{en_e} = - \frac{\partial \phi}{\partial r} + \frac{1}{2en_e} \frac{\partial p}{\partial r} + v B_z$$

$$\frac{1}{\sigma} J_{\theta} + \frac{J_z B_r - J_r B_z}{en_e} = + w B_r - u B_z$$

TABLE I EQUATIONS FOR DENSE PLASMA (contd)

Ohm's Laws (contd)

$$\frac{1}{c} J_z - \frac{J_\theta B_r}{en_e} = - \frac{\partial \phi}{\partial z} + \frac{1}{2en_e} \frac{\partial p}{\partial z} - v B_r$$

State

$$n_e = \frac{p}{2kT}, \quad \rho = \frac{m_a p}{2kT}$$

$$\begin{aligned} B_r &= -\frac{r}{2} \frac{dB(z)}{dz} \\ B_z &= B(z) \end{aligned} \quad (2)$$

## 2. Overall Conservation Laws

The local conservation laws of Table I can be integrated to give overall conservation laws. In addition to the obvious energy, linear momentum, and conservation laws, there are two more which can be integrated.

The angular momentum equation can be integrated over the cathode jet of radius  $R$  to give:

$$\frac{d}{dz} \left\{ \int_0^R \rho v(rV) 2\pi r dr + \int_0^R J_z \left( B \frac{r^2}{2} \right) 2\pi r dr \right\} = 0 \quad (3)$$

Stated in words, the change in the flux of angular momentum is proportional to the change of the magnetic field encompassed by the current. Notice that  $B r^2/2$  is  $1/2\pi$  times the amount of magnetic field inside  $r$ . Equation 3 can be simplified for the special case where  $\rho v$  and  $J_z$  have the same radial distribution, and  $V = \omega(z) \cdot r$ ,

$$\frac{d}{dz} \left( \dot{m} \omega R^2 - B I \frac{R^2}{2} \right) = 0 \quad (4)$$

The radial momentum equation can be integrated by using the azimuthal Ohm's law and the continuity equations to give

$$\int_0^R p(p + \rho v^2) 2\pi r dr = \frac{2B\sigma kT}{m_a} \frac{d}{dz} \int_0^R \left( \rho v - \frac{m_a}{e} J_z \right) \left( \frac{B r^2}{2} \right) 2\pi r dr \quad (5)$$

where

$$p(R) = 0, \quad \frac{\partial B}{\partial r} = 0, \quad \frac{\partial T}{\partial r} = 0.$$

Thus pressure is due to mass and current crossing the magnetic field. Integral 5 is a form of diffusion equation; where  $\left(\frac{\rho v}{m_a} - \frac{j_z}{e}\right)$  is the electron flux, the integral is the amount of magnetic field encompassed by the electron flux, and hence the leakage (change of encompassed field) is proportional to  $p^2/B \propto kT$ .

### 3. The Anode Jet

The purpose of this analysis is to study the motions of the ions. The components of the equation of motion (Eq. 1) in cylindrical coordinates with axial symmetry and steady fields are:

$$\begin{aligned} m(\ddot{r} - r\dot{\theta}^2) &= e\left(-\frac{\partial \phi}{\partial r} + r\dot{\theta}B_z - \dot{z}B_\theta\right) \\ m(r\ddot{\theta} + 2\dot{r}\dot{\theta}) &= e\left(\dot{z}B_r - \dot{r}B_z\right) \\ m\ddot{z} &= e\left(-\frac{\partial \phi}{\partial z} + \dot{r}B_\theta - r\dot{\theta}B_r\right) \end{aligned} \quad (6)$$

The energy and angular momentum integrals are

$$\begin{aligned} \frac{m}{2}(\dot{r}^2 + r^2\dot{\theta}^2) + e\phi &= \text{const}, \\ mr^2\dot{\theta} + e \int_0^R B_z(s, z) s ds &= \text{const}. \end{aligned} \quad (7)$$

In the second part of Eq. 7, the integral is  $r$  times the vector potential, and to our approximation for magnetic fields is  $B r^2/2$ . If particles are introduced at rest from an anode at potential  $\phi_A$ , and radius  $R_A$ , then

$$\begin{aligned} r\dot{\theta} &= eB(R_A^2 - r^2)/2mr \\ \phi &= \phi_A - \frac{m}{2e} \left\{ \dot{r}^2 + \left[ eB(R_A^2 - r^2)/2mr \right]^2 + \dot{z}^2 \right\} \end{aligned} \quad (8)$$

The minimum potential to get an ion from  $R_A$  to  $R_{cr}$  defined as the minimum radial coordinate of an ion trajectory, occurs when  $\dot{r} = \dot{z} = 0$  at  $r = R_{cr}$  and

$$\phi_A - \phi = \frac{eB^2 (R_A^2 - R_{cr}^2)^2}{8m R_{cr}^2} \quad (9)$$

Equation 9 is the voltage drop of the very low density anode jet.

If some  $B_\theta$  is supplied (by currents in an interior cathode jet) and if  $E_r$  is inward, then an axial drift (away from the cathode of the inner conductor) occurs. If the  $B_\theta$  were not present, the ion motion would consist of azimuthal drift with a circular motion superimposed. The path a particle follows is called a hypocycloid. The addition of a  $B_\theta$  field skews the applied field so that the drift perpendicular to the total  $B_\theta/B_z$  field produces an axial component. The velocity at the larger radius of the path is primarily radial, and the velocity at the inner radius is both azimuthal and axial. Thus the azimuthal and axial current carried by the anode jet is carried near its inner edge.

#### 4. The Cathode Jet

A plasma flow away from the cathode, which carries current toward the cathode and moves along a magnetic field, will be analyzed. The existence of such a flow in X-ATRON is probable, since it has been observed in early models which have a similar configuration. The cathode jet can confine pressure by inducing azimuthal currents which interact with the applied magnetic field. The pressure is the result of the diamagnetic effect of the plasma. The cathode jet can heat the plasma by dissipation of electrical power. The purpose of the analysis which follows is to study the heating and confining in a cathode jet.

The analysis in this proposal is divided into two parts. First a simplified set of equations will be derived and solved. Next a more complete set of equations will be discussed. A solution of the more complete equations, when it is found, will give a more



accurate description of the distribution of the temperature, velocity, pressure, and currents. The simplified solution is valuable because it predicts trends (scaling laws) and incorporates most of the mechanisms, without undue complexity. The simplified analysis is a quasi-one dimensional theory which considers only average properties at each cross section.

In the quasi-one dimensional approach it is possible to separate the gas dynamics from the plasma physics. The gas dynamics of a quasi-one dimensional flow gives the pressure, velocity and temperature as a function of the change of area, addition of momentum, and addition of energy. In the cathode jet the plasma physics gives the area change (diffusion across the applied magnetic field) the momentum change ( $\mathbf{J} \times \mathbf{B}$  Lorentz forces) and energy input (due to electrical conduction).

One important feature of the cathode jet is the existence of rotation about the axis, which causes radial pressure gradients due to centrifugal effects, radial potential gradients due to  $\mathbf{v} \times \mathbf{B}$ , and allows much of the energy to be put into azimuthal kinetic energy. Radial pressure gradients will be neglected. Radial potential gradients and azimuthal kinetic energy are dominant and cannot be neglected. An azimuthal momentum equation will be used in addition to the gas dynamics and plasma physics to determine the rotational motion of the quasi-one dimensional cathode jet.

The gas dynamic equations include continuity, momentum energy and an equation of state.

#### Continuity

$$\frac{d}{dt} (\rho A w) = 0 \quad (10)$$

#### Axial Momentum

$$\frac{d}{dz} (A p + \dot{m} w) = (\text{axial force per unit length}) \quad (11)$$

### Energy

$$\dot{m} \frac{d}{dz} \left( \frac{2\gamma}{\gamma - 1} \frac{kT}{m_a} + \frac{w^2}{2} \right) = (\text{energy input}) - (\text{change of azimuthal kinetic energy}) \quad (12)$$

### State

$$\rho = \frac{m_a p}{2kT} \quad (13)$$

In a purely axial magnetic field, the axial Lorentz force per unit length is zero, so the momentum equation can be integrated. We shall consider that the magnetic field is purely axial (i.e.,  $B_r = 0$ ). The energy input per unit length is given by

$$- \frac{d}{dz} \int (J_z \cdot \Phi) dA, \quad (14)$$

and the change of azimuthal kinetic energy by

$$\frac{d}{dz} \int \rho w \frac{v^2}{2} dA. \quad (15)$$

If  $B_r = 0$ , the gas dynamic equations can be integrated.

The plasma physics equations include the generalized Ohm's laws and the radial momentum equation. These give an equation for the rate of growth of the jet due to diffusion across the field.

$$\frac{dR}{dz} = \frac{\tau_{m_a} R p^2}{B^2 \sigma kT \left( \dot{m} + \frac{m_a}{e} I \right)} \quad (16)$$

This is the rate of growth due to classical diffusion. It is necessary to find the potentials to calculate the energy input. The radial potential gradient

$$\frac{\partial \Phi}{\partial r} = BV + \frac{m_a v^2}{er} - \frac{kT}{e} \frac{1}{p} \frac{\partial p}{\partial r} \quad (17)$$

is given by the radial ion momentum equation. Finally the axial Ohm's law gives

$$J_z = \sigma \frac{\partial \phi}{\partial z} \quad (18)$$

The azimuthal momentum equation is given in Eq. 3.

If we let  $\rho\omega = \dot{m}/rR^2$ ,  $J_z = -I/rR^2$ , and  $v(r,z) = \omega(z) \cdot r$ , to get one dimensional motion, then

$$\frac{d}{dz} \left[ \dot{m} \frac{R^2}{2} \omega - IB \frac{R^2}{4} \right] = 0 \quad (19)$$

Thus

$$\omega = \frac{BI(R^2 - R_c^2)}{2\dot{m}R^2} \quad (20)$$

where  $\omega = 0$  when  $R = R_c$ , the radius of the cathode attachment zone.

If the angular velocity is given by Eq. 20, and the third term ( $\sim kT/e$ ) of Eq. 17 is small, then Eq. 17 can be solved for the radial potential drop. Since  $\sigma$  is large, there is negligible potential drop along the axis. Equations 14 and 15 can be evaluated and the energy equation integrated

$$\frac{2\gamma}{\gamma-1} \frac{kT}{m_a} = \left( \frac{2\gamma}{\gamma-1} \frac{kT}{m_a} \right)_{\text{inlet}} + \left( \frac{BI}{4\dot{m}} \right)^2 (R^2 - R_c^2) \left[ \frac{R^2 + R_c^2}{R^2} + \frac{m_a I}{em} \frac{R^2 - R_c^2}{R^2} \right] \quad (21)$$

$$\phi = \frac{B^2 I (R^2 - R_c^2)}{4\dot{m}} \left[ 1 + \frac{m_a I}{em} \frac{R^2 - R_c^2}{R^2} \right] \quad (22)$$

Finally, Eq. 16, the radial diffusion equation can be integrated to find the length  $L$  required to reach any desired radius, since plasma conductivity  $\sigma$  is proportional to  $T^{3/2}$ , and both temperature and pressure variation with  $R$  are known. If  $R^2 \gg R_c^2$ , then

$$L = \frac{\pi B^7 I^5 R^9 \left(1 + \frac{m_a I}{em}\right)^{7/2}}{9252 \left(\frac{2\gamma}{\gamma-1}\right)^{5/2} \left(\frac{k}{m_a}\right)^{3/2} \left(\frac{T}{\sigma}\right)^{3/2} (\pi R^2 p)^2 \dot{m}^4} \quad (23)$$

Continuity can be used to find the axial velocity

$$w = \frac{2\dot{m} kT}{m_a (\pi R^2)} \quad (24)$$

Since the velocity increases linearly with temperature, the Mach number  $M = w (m_a/2\gamma kT)^{1/2}$  will increase with the square root of temperature. The maximum Mach number occurs at the hottest point, and a sonic condition there will determine  $(\pi R^2)$ .

$$(\pi R^2) = \dot{m} \sqrt{\frac{2kT_{\max}}{\gamma m_a}} \quad (25)$$

$$= \sqrt{\frac{(\gamma-1) \left(1 + \frac{m_a I}{em}\right)}{4\gamma}} B I R_{\max}$$

where the last form is for  $R^2 \gg R_c^2$ . Thus we have found solutions for all quantities by the quasi-one dimensional flow method.

There is another method to compute the amount of pressure which can be confined in the cathode jet. The radial diffusion will be greatest where the jet is coldest, which is near the cathode. Hence the inlet region will limit the amount of pressure. The same radial diffusion of electrons which confines pressure produces rotation. This axial rotational gradient forces the axial current to move to the outside of the jet. If the maximum radial diffusion of electrons occurs such that no backward flow of electrons along the centerline occurs, then the largest pressure which can be confined is given by

$$pR^2 = \dot{m} \sqrt{12 \frac{I}{\dot{m}} \frac{kT_{\text{inlet}}}{e}} \quad (26)$$

The pressure will be the smaller of Eqs. 25 or 26.

The expression for pressure shown in Eq. 26 indicates that the wall confinement limits for the plasma are the factors which will determine the confined pressure. It is not yet clear whether one should maximize  $p$ , or  $pR_{\text{inlet}}^2$  at the position where the plasma leaves the containing cylinder (e.g., buffer or segments). In either case the procedures outlined in Ref. 13 can be used to help design the cathode-buffer and/or cathode-segment structure.

If a rather long arc segment column is used, then maintaining the stability of the wall confined arc in the presence of an axial magnetic field will be important. The arc has been found to go unstable, presumably forming a helical path, at low arc currents (Ref. 14). Recent experiments at EOS, however, indicate that this instability becomes suppressed at higher arc currents. Since the X-ATRON will operate at quite high currents, there is thus reason to expect that the discharge will remain steady and axisymmetric in the confined arc column.

The radius at which the anode and cathode jets meet will be such as to minimize the total potential.

$$\phi_{\text{total}} = \frac{B^2 I (R^2 - R_c^2)}{4\dot{m}} \left[ 1 + \frac{m_{ac} I}{e\dot{m}} \frac{R^2 - R_c^2}{R^2} + \frac{eB^2 (R_A^2 - R^2)^2}{8 m_{aa} R^2} \right] \quad (27)$$

The value of  $R$  which minimizes Eq. 27 is called  $R_{\text{crit}}$  and is

$$R_{\text{crit}}^4 = \frac{R_A^4 + \frac{m_{aa}}{m_{ac}} \frac{2}{\gamma_c^2}}{1 + \frac{m_{aa}}{m_{ac}} \frac{2(1 + \gamma_c)}{\gamma_c^2}}, \quad (28)$$

where

$$\gamma_c = \frac{em_c}{Im_{ac}}.$$

Notice that different atomic masses are allowed for the two jets.

$$\phi_{\min} = \frac{eB^2}{4m_{aa}} \left[ \sqrt{\left( R_A^4 + \frac{m_{aa}}{m_{ac}} \frac{2}{\gamma_c^2} R_c^4 \right) \left( 1 + \frac{m_{aa}}{m_{ac}} \frac{2(1 + \gamma_c)}{\gamma_c^2} \right)} - R_A^2 + \frac{m_{aa}}{m_{ac}} \frac{2 + \gamma_c}{\gamma_c^2} R_c^2 \right]$$

Thus in the X-ATRON, the joining radius is given by Eq. 28, which then allows the calculation of all other quantities.

#### a. Detailed Solution for Cathode Jet

Additional analysis is needed to find the radial distribution of mass flow, current, pressure, potential, and azimuthal velocities. The quasi-one dimensional analysis is incapable of finding these distributions. The pressure, for example, may have a radial profile which has a maximum off-axis if the centrifugal forces are large. The axial current density will not be uniform, since rates of change of angular velocity in  $z$  will induce changes in the radial potential drops with respect to  $z$ , and hence changes in the axial potential drops with respect to  $r$  (since  $\nabla \times E = 0$  and thus  $\partial E_r / \partial z = \partial E_z / \partial r$ ). Finally, if  $p$  approaches zero near the edge, it must fall off exponentially since  $\partial p / \partial r$  ( $\sim J_\theta \sim eM V_e \sim p/kT$ ) is proportional to  $p$ . Thus there is much radial structure to the cathode jet which cannot be found from the one dimensional analysis.

It is possible to weaken other hypotheses of the quasi-one dimensional analysis and still obtain a solution. A more realistic magnetic field such as suggested in Eq. 2 will be used. Finite Mach number effects (axial momentum) will be used; however it is unlikely



that this will change the pressure by more than a factor of two from inlet to exit. By assuming power series in  $r$  (radius) for  $\ln p$  (pressure) and  $V$  (azimuthal velocity), we have shown that  $\phi$  (the potential),  $J_r$ ,  $J_z$ , (the currents), etc., have related power series. A system of ordinary differential equations in the variable  $z$  (axial position) has been set up. We now have a method of analysis which can predict the radial distribution of the unknowns.

#### 5. Conclusions

- a. X-ATRON devices can heat and confine plasma under a wide range of operating conditions. The two limiting cases studied were the electron conduction model which applies at high density and the ion conduction model which applies at low density.
- b. The cathode jet grows in diameter as it travels away from the cathode due to diffusion across the applied magnetic field. The growth rate is proportional to the square of the pressure, and inversely to the five-halves power of the temperature and the square of the magnetic field. (These scaling laws apply for classical diffusion in a highly ionized plasma.)
- c. Due to spreading the cathode jet will rotate about its axis. The change of rotation induces EMF's which cause the currents to concentrate near the outer surface of the cathode jet.
- d. In the ion conduction limit, the anode sheath does not spread as it travels away from the anode. It will rotate in the same direction as the cathode jet, and currents concentrate along the inner edge of the annulus.
- e. The cathode jet and anode sheath have small axial potential drops, and act as virtual electrodes.
- f. When the cathode jet grows to the inner diameter of the anode sheath, the zones mix, thus completing the current path. The radius where this occurs can be found by mathematically minimizing the potential.

APPENDIX III  
CATHODE HEAT TRANSFER CALCULATIONS

Case I

Comparison of Power Losses for Cylindrical "Ring" vs Conical "Tip" Arc Attachment Modes.

From Figure 1, it can be seen that, provided the half-width of the attachment "ring" is small with respect to the radius of the cylinder, the problem may be approximately "unwrapped" into a "trough" on a flat plate of thickness R, width  $2\pi R$  and infinite length.

The steady-state heat conduction equation in the absence of sources or sinks is given by

$$\nabla^2 \phi = 0$$

where

$$\phi = \int k \, dT$$

k = thermal conductivity of the cathode material

T = temperature

In the cylindrical geometry of Figure 2 this becomes

$$\frac{1}{r} \frac{d}{dr} \left[ r \frac{d\phi}{dr} \right] = 0$$

or

$$r \frac{d\phi}{dr} = -\lambda \quad \lambda = \text{constant}$$

and

$$\phi = -\lambda \ln r + C_1$$

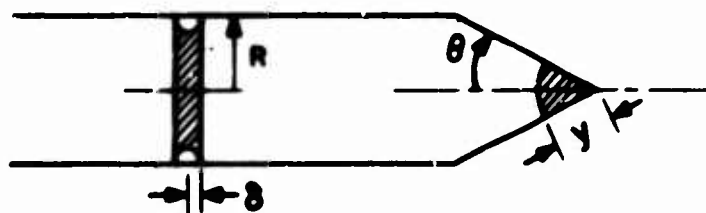


Figure 1 Geometry of "Ring" and "Tip" Cathode Attachments



Figure 2 Geometry of "Unwrapped" Ring Attachment

The boundary conditions  $\phi = \phi_0$  at  $r = \delta$  and  $\phi = \phi_\infty$  at  $r = R$  give

$$\phi_0 - \phi_\infty = \lambda \ln (R/\delta)$$

The heat flux  $q$  is given by

$$q = - \frac{d\phi}{dr} = \frac{\lambda}{r}$$

or

$$q = \frac{\phi_0 - \phi_\infty}{r \ln (R/\delta)}$$

and

$$q|_{r=\delta} = (\phi_0 - \phi_\infty)/\delta \ln (R/\delta)$$

The power is given by  $P_{\text{ring}} = q_{\text{ring}} A_{\text{ring}}$  where  $q_{\text{ring}} = q|_{r=\delta}$  and  $A_{\text{ring}} = 2\pi^2 R\delta$ . Thus

$$P_{\text{ring}} = 2\pi^2 R (\phi_0 - \phi_\infty)/\ln (R/\delta)$$

Now, for the conical tip problem we write  $\nabla^2 \phi$  in spherical polar coordinates and obtain

$$\frac{1}{r^2} \frac{d}{dr} \left[ r^2 \frac{d\phi}{dr} \right] = 0$$

or

$$r^2 \frac{d\phi}{dr} = -\beta$$

or

$$\phi = \frac{\beta}{r} + C$$

Applying the boundary conditions  $\phi = \phi_0$  at  $r = y$  and  $\phi = \phi_\infty$  at  $r = \infty$  we find

$$\phi_0 - \phi_\infty = \beta/y$$

The heat flux is given by  $q = -\frac{d\phi}{dr} = \frac{\beta}{r^2}$  and  $q|_{r=y} = \frac{\beta}{y^2} = \frac{\phi_0 - \phi_\infty}{y}$ . The power is given by  $P_{tip} = q_{tip} A_{tip}$ , where  $q_{tip} = q|_{r=y}$  and  $A_{tip}$  is the spherical cap area which can be determined from the integral

$$A_{tip} = \int_0^\theta \int_0^{2\pi} (y d\theta)(y \sin\theta d\phi) = 2\pi y^2 [1 - \cos\theta]$$

Hence

$$P_{tip} = 2\pi y (\phi_0 - \phi_\infty) [1 - \cos\theta]$$

Further,

$$I_{tip} = I_{ring} = I$$

and

$$\phi_{0\ tip} = \phi_{0\ ring} \text{ (corresponding to the melting point).}$$

Provided the current density is primarily due to thermionic emission the conditions above result in equal current densities and therefore equal emitting areas for the ring and the conical tip

cases. Assuming that the tip melts back to the point where the spherical cap is at the melting point, then

$$2\pi^2 R\delta = 2\pi y^2 (1 - \cos\theta)$$

or

$$y/R = \sqrt{\frac{\delta/R}{1 - \cos\theta}}$$

Thus

$$\frac{P_{\text{tip}}}{P_{\text{ring}}} = \frac{\delta/R}{y/R} \ln(R/\delta)$$

Noting that

$$\sqrt{\frac{1 - \cos\theta}{2}} = \sin\left(\frac{\theta}{2}\right)$$

We find

$$\frac{P_{\text{tip}}}{P_{\text{ring}}} = \sqrt{\frac{\delta}{\pi}} \sin\left(\frac{\theta}{2}\right) X \ln\left(\frac{1}{X}\right)$$

where

$$X^2 = \delta/R < 1$$

The ratio  $P_{\text{tip}}/P_{\text{ring}}$  is shown in Figure 2 of the main body of this report for various values of  $X$  and  $\theta$ . In all cases the ratio is less than unity and decreases with decreasing  $\theta$ . This indicates that within the framework of our assumptions the power loss from a conical attachment is always less than that from a ring attachment.



### Case II

Comparison of Delta Function and Uniform Surface Energy Distributions. For a cylinder of radius  $R$  and length  $L$  with an energy input  $Q(z)$  per unit area, and essentially one-dimensional heat conduction, we obtain the differential equation

$$\frac{d^2 T}{dz^2} = \frac{2Q(z)}{Rk}$$

where

$$Q(z) = V j_i(z) - \chi j_e(z)$$

Physically this implies that the ion current density  $j_i$  arrives at the surface of the cathode with the arc voltage  $V$  while an electron current density  $j_e$  leaves the surface with the work function,  $\chi$ , of the cathode material.

The Richardson equation for thermionic emission may be written in the form

$$j_e = j_0 \left( \frac{T}{T_{\max}} \right)^2 e^{-\chi/kT}$$

The total current, which is to be regarded as constant, is given by

$$I_0 = 2\pi R \int_0^L [j_i(z) + j_e(z)] dz$$

the net power into the cathode, from the ions, is given by

$$P = 2\pi R V \int_0^L j_i(z) dz$$

For the case of a Delta function heat source we take

$$Q(z) = \delta(z)$$

which yields

$$T = C_1 z + C_2$$

The boundary conditions are  $T(0) = T_{\max}$  and  $T(L) = 0$ . We define  $\theta = T/T_{\max}$  and  $\xi = z/L$ .

The temperature distribution is just  $\theta = 1 - \xi$  and

$$j_e = j_0 (1 - \xi)^2 e^{-B/(1 - \xi)} \quad B = e\chi/kT_{\max}$$

Now, for  $z \neq 0$ ,  $Q(z) = 0$  and  $j_1(z) = \frac{\chi}{V} j_e(z)$

$$\text{Thus} \quad I_0 = 2\pi RL j_0 (1 + \chi/V) R(B)$$

$$\text{where} \quad R(B) = \int_0^1 (1 - \xi)^2 e^{-B/(1 - \xi)} d\xi$$

$$\begin{aligned} \text{also,} \quad P_{\text{delta}} &= 2\pi R \int_0^L V j_1(z) dz \\ &= 2\pi RL\chi j_0 R(B) \end{aligned}$$

Substituting for  $R(B)$  from the above current relation we obtain

$$P_{\text{delta}} = I_0 V \left[ \frac{\chi}{V + \chi} \right]$$

For the case of a uniform heat source we take

$$Q(z) = Q_0 = \text{constant}$$

then

$$\frac{d^2 T}{dz^2} = A_0 \quad A_0 = \frac{2Q_0}{RK_0}$$

Applying the same boundary conditions and dimensionless variables we find for the temperature distribution

$$\theta = (1 - \xi)(1 - \alpha\xi) \quad \alpha \equiv A_0 L^2 / 2T_{max}$$

and

$$j_e = j_0 \theta^2 e^{-B/\theta}$$

$$j_i = \frac{\lambda}{V} j_e + \frac{Q_0}{V}$$

$$\begin{aligned} I_0 &= 2\pi R \int_0^L (j_i(z) + j_e(z)) dz \\ &= 2\pi RL \left[ \frac{Q_0}{V} + \left( \frac{V + \lambda}{V} \right) j_0 \mathcal{L}(\alpha, B) \right] \end{aligned}$$

where

$$\mathcal{L}(\alpha, B) \equiv \int_0^1 (1 - \xi)^2 (1 - \alpha\xi)^2 e^{-B/(1 - \xi)(1 - \alpha\xi)} d\xi$$

and

$$\begin{aligned} P_{uniform} &= 2\pi R \int_0^L V j_i(z) dz \\ &= 2\pi RV \int_0^L \left[ \frac{\lambda}{V} j_e(z) + \frac{Q_0}{V} \right] dz \\ &= 2\pi R \lambda \int_0^L j_e(z) dz + 2\pi RLQ_0 \end{aligned}$$

and

$$\int_0^L j_e(z) dz \equiv j_0 L \mathcal{L}(\alpha, B)$$

thus

$$\begin{aligned} P_{\text{uniform}} &= 2\pi RL [x j_0 \mathcal{L} + Q_0] \\ &= I_0 V \left[ \frac{x}{x + \frac{V}{1 + \beta}} \right] \end{aligned}$$

where

$$\beta \equiv \frac{Q_0}{x j_0 \mathcal{L}(\alpha, B)} > 0$$

Therefore

$$\frac{P_{\text{uniform}}}{P_{\text{delta}}} = \frac{x + \frac{V}{1 + \beta}}{x + \frac{V}{1 + \beta}} \geq 1 \text{ for } \beta \geq 0$$

Hence the delta function will, other things being equal, result in a smaller power loss than a uniform energy distribution. This is a general result which can be expected to apply within the framework of the assumptions. In order to obtain numerical values for the power ratio,  $P_{\text{uniform}}/P_{\text{delta}}$ , we must estimate  $\beta$ .

We can obtain a very rough value for  $\beta$  by replacing  $e^{-B/(1-\alpha\xi)(1-\xi)}$  by  $e^{-B[1-\xi]^{2n}}$  which is equivalent to setting  $\alpha = 1$  and replacing the exponential function by a polynomial adjusted to a "best-fit" through the proper choice of  $n$ . It now follows that

$$\begin{aligned} \mathcal{L}(1, B) &= \int_0^1 (1 - \xi)^4 e^{-B} (1 - \xi)^{2n} d\xi \\ &= e^{-B} \frac{(1 - \xi)^{2n+5}}{2n+5} \Big|_0^1 = \frac{e^{-B}}{2n+5} \end{aligned}$$

By comparison with a plot of  $e^{-1/(1-\xi)^2}$  it is found that  $n \approx 20$ .  
Hence

$$\mathcal{L}(1, B) = \frac{1}{45e^B}$$

and

$$\beta = \frac{45e^B Q_0}{\chi J_0}$$

Further, within the spirit of the previous approximation we may take

$$\frac{Q_0}{\chi J_e} = \frac{V}{\chi} \frac{J_i}{J_e} - 1 = O(1)$$

and

$$B = e\chi/kT_{\max} \approx 5$$

hence

$$\beta \approx O(10^4)$$

While the approximations are admitted quite rough, it is clear that  $\beta \gg 1$  and in this limit, provided  $\beta \chi/V \gg 1$  (i.e., provided  $\chi \neq 0$  and  $V$  finite) then

$$\lim_{\beta \rightarrow \infty} \left[ \frac{P_{\text{uniform}}}{P_{\text{delta}}} \right] = 1 + \frac{V}{\chi}$$

## REFERENCES

1. R. A. Moore, G. L. Cann, L. R. Gallagher, High Specific Impulse Thermal Arc Jet Thrustor Technology, TR No. AFAPL-TR-65-48, Air Force Aero Propulsion Laboratory, Jun 1965 (EOS 5090-Phase I Final)
2. G. L. Cann, R. L. Harder, Follow-on Investigation of a Steady State Hall Current Accelerator, NAS CR-54062, NASA-Lewis Research Center, 30 Oct 1964 (EOS 4010-Final)
3. S. Bennett, R. R. John, G. Enos and A. Tushman, Experimental Investigation of the MPD Arc Jet, AIAA Paper No. 66-239
4. R. R. John, S. Bennett, and R. Jahn, Current Status of Plasma Propulsion, AIAA Paper No. 66-565
5. R. M. Patrick and A. M. Schneiderman, Axial Current Distribution in the Exhaust of the Magnetic Annular Arc, Research Report 231, AVCO-EVERETT, prepared for NASA-LRC under Contract No. NAS3-5748, Jul 1966
6. G. L. Cann, R. L. Harder, R. A. Moore, and P. D. Lenn, Hall Current Accelerator, NASA CR-54705, prepared for NASA/LRC under Contract NAS3-5909, 4 Feb 1966 (EOS 5470-Final)
7. G. Schmidt, "Nonadiabatic Particle Motion in Axiallysymmetric Fields," Phys Fluids, 5, 994, 1962
8. G. L. Cann, R. L. Harder, Study of Electrode Attachment Regions in High-Current Gaseous Discharges, Arnold Engineering Development Center, Report AEDC-TDR-64-107, Aug 1964
9. G. L. Cann, R. A. Moore, P. F. Jacobs, L. R. Gallagher, High Specific Impulse Thermal Arc Jet Thrustor Technology, Interim Technical Report on Contract AF 33(615)-1579, Air Force Aero Propulsion Laboratory, Sep 1965 (EOS 5090-IR-2)
10. G. L. Cann, "Energy Transfer Processes in a Partially Ionized Gas," Ph.D. Thesis; published as GALCIT Hypersonic Research Project Memorandum No. 61, Jun 15, 1961
11. G. L. Cann, R. A. Moore, R. D. Buhler, G. L. Marlotte, Thermal Arc Jet Research, TDR No. ASD-TDR-63-632, Air Force Aero Propulsion Laboratory Contract AF 33(657)-8839, 15 Aug 1963 (EOS 3170-Final)
12. R. A. Moore, G. L. Cann, et al, Thermal Arc Jet Research, TDR No. APL-TDR-64-55, Air Force Aero Propulsion Laboratory, May 1964



REFERENCES (contd)

13. G. L. Cann and R. D. Buhler, "A Survey and Prediction of the Performance Capability of Coaxial Arc Heaters," Paper presented at AGARD Specialists' Meeting on Arc Heaters and MHD Accelerators for Aerodynamic Purposes, Belgium, 21 Sep 1964
14. M. C. Yuen, "Stability of the Poiseuille Plasma Arc in an Axial Magnetic Field," The Physics of Fluids, Vol. 9, No. '6, pp 1140-1150, Jun 1966

Unclassified

Security Classification

DOCUMENT CONTROL DATA - R&D		
(Security classification of title, body of abstract and indexing annotation must be entered when the overall report is classified)		
1. ORIGINATING ACTIVITY (Corporate author)		2a. REPORT SECURITY CLASSIFICATION
Electro-Optical Systems, Inc. A Subsidiary of Xerox Corporation 300 No. Halstead, Pasadena, California		Unclassified
		2b. GROUP
3. REPORT TITLE		
HIGH SPECIFIC IMPULSE THERMAL ARCJET THRUSTOR TECHNOLOGY		
4. DESCRIPTIVE NOTES (Type of report and inclusive dates)		
Summary Technical Report, Phase II - 1 April 1965 to 31 March 1966		
5. AUTHOR(S) (Last name, first name, initial)		
Cann, Gordon L; Moore, Robert A; Harder, Robert L; and Jacobs, Paul F.		
6. REPORT DATE	7a. TOTAL NO. OF PAGES	7b. NO. OF REFS
January 1967	154	14
8a. CONTRACT OR GRANT NO.	8b. ORIGINATOR'S REPORT NUMBER(S)	
AF 33(615)-1579	EOS Report 5090-Phase II Final	
9. PROJECT NO.	9b. OTHER REPORT NO(S) (Any other numbers that may be assigned this report)	
314101		
10. AVAILABILITY/LIMITATION NOTICES		
11. SUPPLEMENTARY NOTES	12. SPONSORING MILITARY ACTIVITY	
	Air Force Aero Propulsion Laboratory Research and Technology Division Air Force Systems Command Wright Patterson Air Force Base, Ohio 45433	
13. ABSTRACT The objective of this program is to develop efficient electric arcjet thrusters for high specific impulse and long life. Power levels between 10 and 50 kW, specific impulse between 1500 and 6500 seconds are sought with power input-to-thrust ratios less than 190 kW/lb for durations up to 100 hours. The approach combines analytical and experimental research to investigate and develop thrusters using lithium and other alkali metals as propellants. The present approach has relied predominantly on Hall current interactions with an applied magnetic field. Thrusters of this type have been designated ALPHA (Alkali Plasma Hall Accelerator). During the second phase of the program the following advances have been made. The effects of the testing environment upon the measured performance have been investigated. The performance of potassium propellant has been investigated and found to be comparable with that of lithium at low $I_{sp}$ and worse at a higher $I_{sp}$ . Two major modifications to the design of the engine have been made: (a) the cylindrical cathode has been replaced by a buffered cathode with separate propellant injection, thereby increasing the thrust per unit current, decreasing the cathode power loss per unit current, increasing the insulator lifetime, and helping to separate the ionization and acceleration processes; and (b) the region of strong magnetic field has been extended downstream by placing a second coil on the engine, reducing magnet power requirement by a factor of almost five. Thrust balance has been improved. A new feed system has been designed to provide continuous operation for periods over 100 hours at levels around 10 mg/sec. A theory has been developed for the operation of ALPHA. Calculations based on this theory indicate that significant improvements can be made over present performance.		

DD FORM 1 JAN 64 1473

Unclassified  
Security Classification

Unclassified

Security Classification

14. KEY WORDS	LINK A		LINK B		LINK C	
	ROLE	WT	ROLE	WT	ROLE	WT
ALPHA (Alkali Plasma Hall Accelerator) arcjet thruster lithium						

#### INSTRUCTIONS

1. **ORIGINATING ACTIVITY:** Enter the name and address of the contractor, subcontractor, grantee, Department of Defense activity or other organization (corporate author) issuing the report.
- 2a. **REPORT SECURITY CLASSIFICATION:** Enter the overall security classification of the report. Indicate whether "Restricted Data" is included. Marking is to be in accordance with appropriate security regulations.
- 2b. **GROUP:** Automatic downgrading is specified in DoD Directive 5200.10 and Armed Forces Industrial Manual. Enter the group number. Also, when applicable, show that optional markings have been used for Group 3 and Group 4 as authorized.
3. **REPORT TITLE:** Enter the complete report title in all capital letters. Titles in all cases should be unclassified. If a meaningful title cannot be selected without classification, show title classification in all capitals in parentheses immediately following the title.
4. **DESCRIPTIVE NOTES:** If appropriate, enter the type of report, e.g., interim, progress, summary, annual, or final. Give the inclusive dates when a specific reporting period is covered.
5. **AUTHOR(S):** Enter the name(s) of author(s) as shown on or in the report. Enter last name, first name, middle initial. If military, show rank and branch of service. The name of the principal author is an absolute minimum requirement.
6. **REPORT DATE:** Enter the date of the report as day, month, year, or month, year. If more than one date appears on the report, use date of publication.
- 7a. **TOTAL NUMBER OF PAGES:** The total page count should follow normal pagination procedures, i.e., enter the number of pages containing information.
- 7b. **NUMBER OF REFERENCES:** Enter the total number of references cited in the report.
- 8a. **CONTRACT OR GRANT NUMBER:** If appropriate, enter the applicable number of the contract or grant under which the report was written.
- 8b, 8c, & 8d. **PROJECT NUMBER:** Enter the appropriate military, department identification, such as project number, subproject number, system numbers, task number, etc.
- 9a. **ORIGINATOR'S REPORT NUMBER(S):** Enter the official report number by which the document will be identified and controlled by the originating activity. This number must be unique to this report.
- 9b. **OTHER REPORT NUMBER(S):** If the report has been assigned any other report numbers (either by the originator or by the publisher), also enter this number(s).
10. **AVAILABILITY/LIMITATION NOTICES:** Enter any limitations on further dissemination of the report, other than those

imposed by security classification, using standard statements such as:

- (1) "Qualified requesters may obtain copies of this report from DDC."
- (2) "Foreign announcement and dissemination of this report by DDC is not authorized."
- (3) "U. S. Government agencies may obtain copies of this report directly from DDC. Other qualified DDC users shall request through \_\_\_\_\_."
- (4) "U. S. military agencies may obtain copies of this report directly from DDC. Other qualified users shall request through \_\_\_\_\_."
- (5) "All distribution of this report is controlled. Qualified DDC users shall request through \_\_\_\_\_."

If the report has been furnished to the Office of Technical Services, Department of Commerce, for sale to the public, indicate this fact and enter the price, if known.

11. **SUPPLEMENTARY NOTES:** Use for additional explanatory notes.

12. **SPONSORING MILITARY ACTIVITY:** Enter the name of the departmental project office or laboratory sponsoring (paying for) the research and development. Include address.

13. **ABSTRACT:** Enter an abstract giving a brief and factual summary of the document indicative of the report, even though it may also appear elsewhere in the body of the technical report. If additional space is required, a continuation sheet shall be attached.

It is highly desirable that the abstract of classified reports be unclassified. Each paragraph of the abstract shall end with an indication of the military security classification of the information in the paragraph, represented as (TS), (S), (C), or (U).

There is no limitation on the length of the abstract. However, the suggested length is from 150 to 225 words.

14. **KEY WORDS:** Key words are technically meaningful terms or short phrases that characterize a report and may be used as index entries for cataloging the report. Key words must be selected so that no security classification is required. Identifiers, such as equipment model designation, trade name, military project code name, geographic location, may be used as key words but will be followed by an indication of technical context. The assignment of links, rules, and weights is optional.